Physics – Uspekhi **51** (2) 167 – 198 (2008)

CONFERENCES AND SYMPOSIA PACS numbers: 01.10.Fv, **74.20. – z**, **74.72. – h**

Scientific session of the Physical Sciences Division of the Russian Academy of Sciences "Room temperature superconductivity" (4 October 2007)

DOI: DOI: 10.3367/UFNr.0178.200802e.0175

On 4 October, 2007, the scientific session of the Division of Physical Sciences of the Russian Academy of Sciences on room-temperature superconductivity was held at the conference hall of the Lebedev Physics Institute, Russian Academy of Sciences. The following reports were made at this session:

1. **Maksimov E G** (Lebedev Physics Institute, Russian Academy of Sciences, Moscow). "Room-temperature superconductivity: myth or reality?";
2. **Božović I** (Brookhaven National Laboratory, USA). "Experiments with atomically smooth thin films of cuprate superconductors: strong electron – phonon coupling and other surprises";
3. **Antipov E V, Abakumov A M** (Moscow State University, Chemical Department, Moscow). "Structural design of superconductors based on complex copper oxides";
4. **Kopaev Yu V, Belyavskii V I, Kapaev V V** (Lebedev Physics Institute, Russian Academy of Sciences, Moscow). "With cuprate luggage to room-temperature superconductivity."

An abridged version of these reports is given below.

PACS numbers: **74.20. – z**, **74.72. – h**
DOI: 10.1070/PU2008v051n02ABEH006465
DOI: 10.3367/UFNr.0178.200802f.0175

Room-temperature superconductivity: myth or reality?

E G Maksimov

The problem of high-temperature superconductivity (HTSC) is considered to have appeared following the pioneering works by Ginzburg [1] and Little [2], who showed the possibility of nonphonon superconductivity mechanisms due to the interaction of electrons with electron excitations (excitons). The energy of these excitations is much higher than the phonon energy, which can result in substantially higher superconducting transition temperatures. Although this work attracted the particular interest of experts in the superconductivity physics, it did not cause a serious boom in HTSC investigations. Moreover, a number of prominent scientists demonstrated scepticism about Ginzburg's and Little's ideas, and some of them published works (see, e.g., [3]) stating that high values of T_c cannot be reached in principle for any superconductivity mechanism at all. This statement followed from the inequality for static permittivity $\varepsilon(\mathbf{q}, 0) > 0$, which was regarded in [3] as a system stability criterion. However, Kirzhnits [4] long ago rigorously proved that the condition $\varepsilon(\mathbf{q}, 0) > 0$ is not a stability criterion if charge density waves occur in the system. The corresponding condition is written as the inequality $1/\varepsilon(\mathbf{q}, 0) < 1$, which demonstrates that the situation where $\varepsilon(\mathbf{q}, 0) > 1$ or $\varepsilon(\mathbf{q}, 0) < 0$ can occur in a stable system. Nevertheless, Anderson [5] again repeats the erroneous arguments regarding the possible nature of high-temperature superconductivity related to the inequality $\varepsilon(\mathbf{q}, 0) > 0$. In the report presented in the session, this issue was discussed in detail; however, we do not dwell on this point, since we have recently published the relevant paper in *Physics – Uspekhi* ([6]).

Generally speaking, the appearance of the problem of high-temperature superconductivity should be dated 1946 rather than 1964. In that year, Ogg from Stanford University [7] detected superconductivity at a temperature $T_c \approx -90\,^\circ$C. His work was titled "Bose – Einstein Condensation of Trapped Electron Pairs. Phase Separation and Superconductivity of Metal – Ammonia Solutions." If the last words in this title were substituted, for instance, by superconducting cuprates or high-temperature superconductors, that work would be similar to numerous recent HTSC studies. According to a legend existing in the physics community, Ogg's works were neither recognized nor supported by most of his colleagues. The degree of this nonrecognition was such that, according to this legend, Ogg committed suicide. It is now clear with some degree of certainty that Ogg was likely to have observed the transformation of a metal – ammonia solution into a metallic state (in which the resistance decreased by several orders of magnitude) rather than into a superconducting state. Another point is more important: in 1946, long before the appearance of works by Bardeen, Cooper, and Schrieffer [8] and Schafroth's group [9] regarding the formation of real electron pairs followed by Bose condensation, Ogg proposed a plausible explanation of superconductivity in metallic systems.

The boom in the problem of high-temperature superconductivity began with the work by Bednortz and Müller [10], in which they detected superconductivity in $La_{1-x}Ba_xCuO_4$ compounds at a temperature $T_c \approx 30$ K. The discussion of the consequences of this boom for the problem of HTSC is beyond the scope of this work; such a discussion is given in our review [11], for example. Here, we only dwell on some conclusions that are important for the

Uspekhi Fizicheskikh Nauk **178** (2) 175 – 210 (2008)
Translated by K V Shakhlevich; edited by A M Semikhatov

problem of room-temperature superconductivity. First, this concerns the nature of the superconducting state in cuprates. In most metals, the transition to a superconducting state is known to be well described in terms of the Bardeen – Cooper – Schrieffer (BCS) model [8]. This means that electrons near the Fermi surface are coupled into Cooper pairs, which form something that resembles Bose condensation, due to the electron – electron attraction. After discovering superconducting cuprates with the transition temperature $T_c \approx 30$ K, researchers proposed a number of scenarios in which a superconducting state appears due to various mechanisms other than the formation of Cooper pairs. We do not discuss these mechanisms here because it is now obvious that superconductivity in cuprates is based on the same phenomenon as the appearance of Cooper pairs. This was most clearly demonstrated by angle-resolved photoemission spectroscopy [12]. The authors of [12] proved that the electron excitations in the superconducting state of these systems represent so-called Bogoliubov quasiparticles, i.e., a coherent mixture of electrons and holes, which follows from the BCS model. Of course, the superconductivity in HTSC cuprates is not described by the simple BCS model, which uses well-determined electron quasiparticle excitations weakly interacting with each other. Superconducting cuprates have a system of strongly interacting electrons subjected to damping. The wave function of electron pairs is anisotropic, in contrast to the wave function of the simple BCS model, which involves the isotropic s pairing. These differences should be taken into account in calculating or estimating T_c, but they are not critical for the purposes of this report.

The only question that is challenging for both the problem of superconductivity in cuprates and the discussion of the possibility of room-temperature superconductivity is the nature of the interaction that results in electron pairing into Cooper pairs. Broadly speaking, only two possibilities exist. First, these can be the well-known electron – phonon and electron – exciton interactions. The other possibility is provided by magnetic interactions between electrons. Such interactions, for example, can result in various magnetically ordered states. The critical magnetic transition temperatures can be rather high: in many cases, they are well above both the superconducting transition temperature T_c in cuprates and room temperature. In discussing the possibilities of achieving high T_c for a superconducting transition due to magnetic interactions, the following points must be taken into account. The magnetic transition temperature T_M depends on the electron – electron exchange interaction constant J,

$$T_M \approx J\,. \tag{1}$$

But the superconducting transition temperature depends directly not on J but on the dimensionless constant $g = N(0)\,J$, where $N(0)$ is the density of electron states at the Fermi surface. The corresponding dependence has the form

$$T_c = \varepsilon_F \exp\left(-\frac{1}{N(0)\,J}\right), \tag{2}$$

where ε_F is the Fermi energy.

In the Hubbard model, which is often used to describe systems with strong exchange – correlation effects, the exchange constant can be written as

$$J = t\,\frac{t}{U}\,, \tag{3}$$

where t is the overlap integral and U is the on-site Coulomb repulsion. According to estimates obtained for the compound La_2CuO_4, which is an insulator and antiferromagnet in the undoped state, the exchange constant is $J \approx 0.1$ eV ≈ 1000 K. It is then not surprising that the antiferromagnetic transition temperature in this compound is relatively high ($T_M \approx 230$ K). The dimensionless coupling constant g in this model can be written as

$$g = N(0)\,t\,\frac{t}{U} \approx \frac{t}{ZU}\,, \tag{4}$$

where Z is the number of the nearest neighbors. In this case, g is of the order of 0.1, and the resulting value of T_c is well below 100 K and, all the more, below room temperature at any reasonable value of the prefactor in Eqn (2) ($\varepsilon_F \sim t$). Therefore, hereafter, we restrict ourselves to the discussion of the possibilities of room-temperature superconductivity in terms of the standard electron – phonon interaction (EPI) and the BCS model. As Kikoin once wrote, [1]

Until a single vibration
Exists in earthly world
And powerful workstation
Gives us its wireless cord,
Until our Troika lashes,
Until our brains progress,
The pairs will couple in Russia
By means of BCS!

The maximum value of T_c characteristic of a system with the electron – phonon superconducting mechanism was found in the compound MgB_2 (≈ 40 K). The question arises: Is it possible to increase this value of T_c in terms of the electron – phonon mechanism? The modern theory of solids can answer this question using a rigorous quantitative analysis of electron – phonon interaction effects in metals. For this analysis, the electron-density functional method can be used to calculate the electron and phonon spectra of metals and matrix elements of the electron – phonon interaction. The corresponding calculations are described in detail, for example, in our reviews [13, 14] published in *Physics – Uspekhi*.

In a system with electron – phonon interaction, the superconducting transition temperature can be written as

$$T_c = \frac{\omega_{\ln}}{1.4}\,\exp\left(\frac{1+\lambda}{\lambda-\mu^*}\right), \tag{5}$$

where μ^* is the Coulomb pseudopotential that describes the contribution of the Coulomb interaction to superconductivity. In most standard metals, this contribution is rather small ($\mu^* \approx 0.1$) and may be neglected when the problem of EPI-induced high-temperature superconductivity is considered. The electron – phonon coupling constant λ and the prefactor $\omega_{\ln}$ are expressed using the Eliashberg function $\alpha^2(\omega)\,F(\omega)$ as

$$\lambda = 2\int_0^\infty \frac{\alpha^2(\omega)\,F(\omega)}{\omega}\,\mathrm{d}\omega\,, \tag{6}$$

and

$$\omega_{\ln} = \frac{2}{\lambda}\int_0^\infty \alpha^2(\omega)\,F(\omega)\ln(\omega)\,\mathrm{d}\omega\,. \tag{7}$$

[1] Translated by K A Kikoin, the author of the poem "How Hi T_c was searched for in Russia," published in Russian in: *The Seminar: Papers and Reports*, compiled by B M Bolotovskii and Yu M Bruk (Moscow, Izd. Fiziko-Matematicheskoi Literatury, 2006), p. 245.

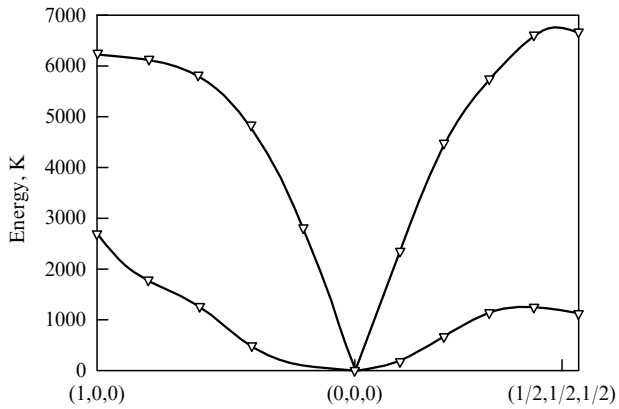

Figure 1. Calculated phonon frequencies of metallic fcc hydrogen at $r_s = 1$.

In turn, the Eliashberg function can be represented in the form

$$\alpha^2(\omega)\,F(\omega) = \frac{1}{N(0)} \sum_{k,q,i} \frac{|g^{\lambda,i}_{k,k+q}|^2}{\omega_{q\lambda} M_i}\,\delta(\varepsilon_k - \varepsilon_F) \times \delta(\varepsilon_{k+q} - \varepsilon_F)\,\delta(\omega - \omega_{q\lambda})\,, \tag{8}$$

where $g^{\lambda,i}_{k,k+q}$ is the EPI matrix element, λ is the phonon mode index, and i is the atom number in the unit cell. All the quantities entering the expression for $\alpha^2(\omega)\,F(\omega)$ are calculated using the density functional method; hence, T_c can easily be calculated without using any fitting parameters.

As an example of this analysis, we note paper [15], where the properties of metallic hydrogen at high pressures were calculated. Figure 1 shows the phonon frequencies calculated in a face-centered cubic (fcc) structure at the pressure $p \approx 20$ Mbar. The energy of the transverse acoustic mode is seen to be substantially lower than that of the longitudinal mode; i.e., the transverse mode is rather 'soft.' The importance of soft modes for high values of T_c was repeatedly discussed in works dealing with superconductivity physics. This can be understood from Fig. 2, which shows the spectral density of the electron–phonon interaction (Eliashberg function). It is seen that the Eliashberg function intensity at the energies corresponding to the transverse mode (1000–2000 K) is significantly higher than in the longitudinal-mode energy range (near 6000 K). The conclusion regarding the importance of soft modes for high values of T_c was previously deduced from the formula

$$\lambda = \frac{N(0)\langle I^2\rangle}{M\langle\omega^2\rangle} \tag{9}$$

for the electron–phonon coupling constant λ. As follows from this formula, λ increases with decreasing $\langle\omega^2\rangle$, i.e., for soft phonon modes. We note that the transverse mode is soft only in a conventional sense, because it is small compared to the longitudinal mode, but its absolute values ($\sim$ 1000–2000 K) are not small compared to room temperature. Our calculations with Eqns (5)–(7) for metallic hydrogen give $\lambda = 6.1$ and, correspondingly, $T_c = 600$K, which is well above room temperature [15]. Of course, it is impossible to use the superconductivity of metallic hydrogen in practice, and a pressure of 20 Mbar cannot be generated under laboratory conditions.

Pickett [16] comprehensively analyzed the possibilities of a significant increase in T_c due to the electron–phonon interaction in systems such as MgB_2 and boron-doped diamond. The analysis results for MgB_2 demonstrate that electrons in this compound strongly interact with only two phonon modes (i.e., bending modes with $\omega_a \approx 20-25$ meV) of the nine modes existing in this compound. Moreover, this interaction is bounded by small values of wave vectors **q** (12% of the total Brillouin zone). Nevertheless, $T_c = 40$ K for MgB_2! The question arises: What values of T_c could be achieved if the interaction of electrons with all modes was strong? In this case, the EPI constant could be $\lambda = 22.5$. In the limit of high values of λ, T_c can be written as

$$T_c = 0.18\sqrt{\lambda\langle\omega^2\rangle} = 0.18\int_0^\infty \omega\alpha^2(\omega)\,F(\omega)\,\mathrm{d}\omega\,. \tag{10}$$

As was shown in [16], at $\lambda = 22.5$ K, temperature T_c would reach 300–430 K! The expression for $\lambda\langle\omega^2\rangle$ can be rewritten as

$$\lambda\langle\omega^2\rangle = \sum_i \frac{N_i(0)\langle I_i^2\rangle}{M_i}\,, \tag{11}$$

where $\langle I_i^2\rangle$ is the EPI matrix element on the Fermi surface,

$$\langle I_i^2\rangle = \sum_{n,k} \left|\left\langle nk\left|\frac{\partial V_{ie}(\mathbf{r}-\mathbf{R}_i)}{\partial \mathbf{R}_i}\right|nk\right\rangle\right|^2 \delta(\varepsilon_k - \varepsilon_F)\,. \tag{12}$$

Here, $V_{ie}(\mathbf{r}-\mathbf{R}_i)$ is the self-consistent ion potential. Pickett [16] also showed that the situations with superconductivity in MgB_2 and boron-doped diamond have many common features. Both systems have strong covalent bonds, which result in large values of $\langle I_i^2\rangle$; moreover, small ionic masses in these systems also favor an increase in the coupling constant λ. The substantial difference between these systems consists in the fact that the electron system of MgB_2 is two-dimensional and that of boron-doped diamond is three-dimensional. This leads to a small density of electron states in boron-doped diamond.

Unfortunately, Pickett [16] specified no concrete methods to achieve the above extremely high values of T_c in MgB_2. He only noted the importance of the further search for compounds with a quasi-two-dimensional electron system and

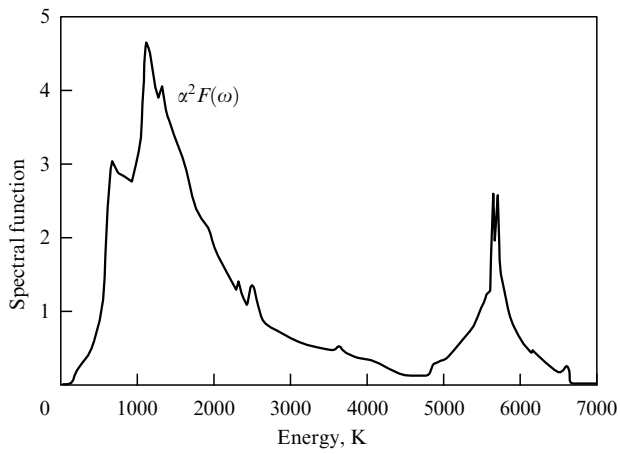

Figure 2. Calculated spectral density of the electron–phonon interaction in metallic fcc hydrogen at $r_s = 1$.

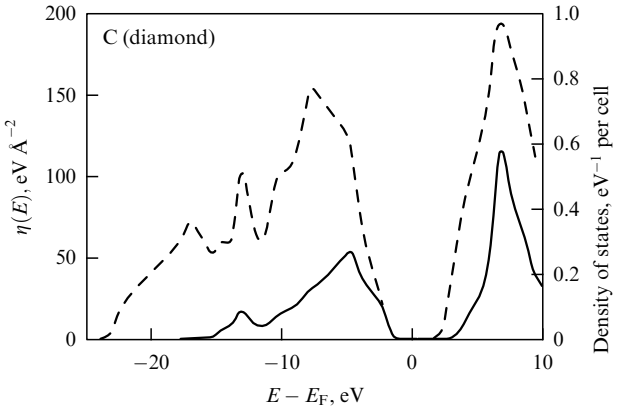

Figure 3. Electron-state density (dashed line) and the Hopfield parameter for diamond (solid line) (borrowed from [18]).

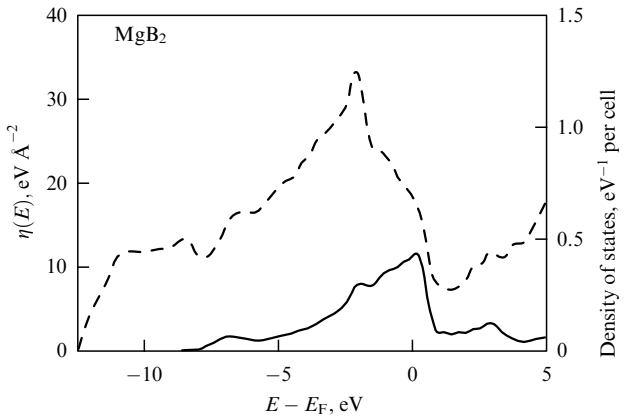

Figure 4. The density of electron states (dashed line) and the Hopfield parameter for MgB_2 (solid line) (borrowed from [18]).

strong covalent bonds. The authors of [17, 18] used another approach to the problem of high-temperature superconductivity in EPI systems. They rewrote $N(0)\langle I_i^2\rangle$ not only for energies at the Fermi surface but also for any energies using the Hopfield parameter η,

$$\eta_i(E) = \sum_{n,k} \left| \left\langle nk \left| \frac{\partial V_{\rm ie}}{\partial \mathbf{R}_i} \right| nk \right\rangle \right|^2 \delta(E - \varepsilon_k + \varepsilon_{\rm F}) \,. \qquad (13)$$

With the density functional method, the authors of [17, 18] calculated $N(0)\langle I_i^2\rangle$ for a number of systems, including aluminum. The calculation results for diamond and MgB_2 are shown in Figs 3 and 4 borrowed from [18]. As is seen in Fig. 3, the $\eta(E)$ function in doped diamond can reach rather high values if the chemical potential of the system is placed 6 eV below or 6 eV above that in pure diamond. The corresponding values of T_c can be rather high. For example, $T_c^{\max} \approx 290$ K in the case of hole doping and $T_c^{\max} \approx 420$ K in the case of electron doping. Unfortunately, it is still unclear whether it is possible to produce diamond with such a high level of doping. As regards high T_c, the situation in MgB_2 is much less optimistic (see Fig. 4). In Al, $N(0)\langle I_i^2\rangle$ very weakly depends on energy, and its absolute value is well below that for systems with covalent bonds.

Unfortunately, we cannot now unambiguously answer the question formulated in the title of this report. This is thought to be a dream rather than a myth. In 1976, Ginzburg published a note titled "High-Temperature Superconductivity: A Myth or Reality?" in *Physics – Uspekhi* [19]. Within almost a decade, this dream concerning high-temperature superconductors was achieved. We hope that the same will be true of room-temperature superconductivity.

Acknowledgments. I am grateful to V L Ginzburg for his constant support in studying the problem of high- and room-temperature superconductivity.

This work was supported by the state program for support of leading scientific schools, scientific programs of the Russian Academy of Sciences, and the Russian Foundation for Basic Research (project no. 08-02-00757).

References

1. Ginzburg V L *Phys. Lett.* **13** 101 (1964)
2. Little W A *Phys. Rev.* **134** A1416 (1964)
3. Cohen M L, Anderson P W, in *Superconductivity in d- and f- Band Metals* (AIP Conf. Proc., Vol. 4, Ed. D H Douglass) (New York: AIP, 1972) p. 17
4. Kirzhnits D A *Usp. Fiz. Nauk* **119** 357 (1976) [*Sov. Phys. Usp.* **19** 530 (1976)]
5. Anderson P W *Science* **316** 1705 (2007)
6. Maksimov E G, Dolgov O V *Usp. Fiz. Nauk* **177** 983 (2007) [*Phys. Usp.* **50** 933 (2007)]
7. Ogg R A (Jr.) *Phys. Rev.* **69** 243 (1946)
8. Bardeen J, Cooper L N, Schrieffer J R *Phys. Rev.* **108** 1175 (1957)
9. Schafroth M R *Phys. Rev.* **96** 1149, 1442 (1954); **100** 463 (1955)
10. Bednorz J G, Müller K A *Z. Phys. B* **64** 189 (1986)
11. Maksimov E G *Usp. Fiz. Nauk* **170** 1033 (2000) [*Phys. Usp.* **43** 965 (2000)]
12. Matsui H et al. *Phys. Rev. Lett.* **90** 217002 (2003)
13. Savrasov S Yu, Maksimov E G *Usp. Fiz. Nauk* **165** 773 (1995) [*Phys. Usp.* **38** 737 (1995)]
14. Maksimov E G, Savrasov D Yu, Savrasov S Yu *Usp. Fiz. Nauk* **167** 353 (1997) [*Phys. Usp.* **40** 337 (1995)]
15. Maksimov E G, Savrasov D Yu *Solid State Commun.* **119** 569 (2001)
16. Pickett W E *J. Supercond. Nov. Magn.* **19** 291 (2006)
17. Cohen M L *J. Supercond. Nov. Magn.* **19** 283 (2006)
18. Moussa J E, Cohen M L *Phys. Rev. B* **74** 094520 (2006); cond-mat/0607832
19. Ginzburg V L *Usp. Fiz. Nauk* **118** 315 (1976) [*Sov. Phys. Usp.* **19** 174 (1976)]

PACS numbers: **74.45.+c**, **74.78.–w**, **81.15.–z**

DOI: 10.1070/PU2008v051n02ABEH006466

DOI: 10.3367/UFNr.0178.200802f.0179

Experiments with atomically smooth thin films of cuprate superconductors: strong electron – phonon coupling and other surprises

I Božović

This paper is based on a presentation prepared for the Scientific Session of the Physical Sciences Department of the Russian Academy of Sciences held on October 4, 2007, in honor of 90th birthday of Academician V L Ginzburg. A short review is presented of our own work only, including some very recent experiments, on molecular beam epitaxy of thin films of high-temperature superconductors (HTS). We have developed a technique to fabricate HTS heterostructures with atomically smooth surfaces and interfaces. This has enabled a series of novel or improved experiments that

allowed us to address several key questions related to the physics of HTS such as how it relates to the proximal antiferromagnetic and pseudo-gap states. Firm experimental evidence is obtained that in HTS cuprates coupling of electrons to certain lattice vibrations is very strong. Next, we have observed interface superconductivity in bilayers consisting of two non-superconducting cuprates; the superfluid is confined within a $1-2$ unit-cell-thick layer next to the interface. In the long run, this discovery may revive the search for HTS in novel metal-insulator (MIMIM...) superlattices in which the mobile electrons in metallic layers are paired by interaction that is enhanced in or originates from the dielectric layers, as it was proposed by VLG forty years ago [1, 2].

1. The oxide molecular beam epitaxy (MBE) system at BNL

The experiments to be described in this review are based on advanced 'digital' synthesis technique whereby atomic layers of complex oxides are deposited one at a time, allowing for 'atomic-layer engineering' of the sample as needed for a particular experiment [3]. The enabling hardware is the 'next-generation' oxide MBE system (see Fig. 1) of our design and construction [4]. It is equipped with several state-of-the-art surface analytical tools that allow for unprecedented control of the film growth process based on *in-situ*, real-time, atomic-level monitoring of the film surface [4, 5]. Here we give a short description of this apparatus, now located at Brookhaven National Laboratory (BNL).

The main growth chamber (Fig. 1a) holds 16 spools ('arms'), each of which contains a metal atom source, a pneumatic linear-motion shutter, a gate valve and a turbomolecular pump. It is thus possible to recharge, service, outgas or change each source without breaking the vacuum in the main chamber, even while a film is being grown. Conversely, it is also possible to valve-off all the sources, vent the main chamber, service whatever may be needed, pump the chamber down, and grow films later the same day. Because of this high level of modularity the system up-time (say, the fraction of time when it is possible to grow films) is essentially 100%, despite considerable system complexity. This performance is pretty much unique today among research-grade MBE systems and it has been the key 'secret' of the group's success.

For most elements, we use resistively heated thermal effusion sources (also called Knudsen cells, or K-cells for short), stabilized to a high level ($\Delta T = 0.1-1\,^{\circ}\mathrm{C}$). Depending on the element, we use K-cells of different type: low-temperature (for Ca, Sr, or Ba), standard (for Bi, Mn, Au), high-temperature (for La, Ti) or dual-filament (for Cu). The latter type allows one to keep the crucible lip hotter than the bottom, and thus to prevent the source material build up (with concomitant reduction in flux of evaporated atoms) near the top of the crucible. For refractory elements with the melting point too high for resistively heated effusion cells, we have special rod-fed electron-beam sources, made to match the K-cells in physical dimensions so that they are interchangeable. Altogether, with this variety of source types, we can cover most of the elements in the periodic table.

The growth chamber is also provided with a sample manipulator (6 degrees of freedom) that carries a sample holder equipped with four UHV-compatible quartz-lamp heaters, each of which is powered and controlled independently. The sample manipulator also supports a set of four water-cooled nozzles for delivery of ozone or another reactive gas.

A scanning quartz-crystal rate monitor (QCM) is mounted on a separate motorized and computer-controlled manipulator that allows for x, y, z motion. The deposition rate, for each source, can be mapped accurately over the wafer area.

The MBE machine also includes a custom-made 16-channel atomic absorption spectroscopy (AAS) system. Each AAS channel contains a hollow-cathode lamp matched to the source element, a mechanical chopper, fiber optics to guide the light to and from the source spool, a monochromatic filter, a photo-multiplier detector, a lock-in amplifier, an a/d converter, and supporting electronics. AAS allows us to accurately monitor the atomic fluxes in real-time (i.e., during film deposition). This capability is critically important to ensure the correct atom count, since due to exposure to ozone the evaporation rates of some source materials change substantially during growth. This is particularly the case for reactive metals such as Ca, Sr, or Ba that readily oxidize in ozone atmosphere, which causes the evaporation rates to drop. For this reason, we use AAS to monitor the atomic fluxes in real time and feed this information to the computer that controls the film growth. The corrections are implemented instantaneously by adjusting the shuttering times, while

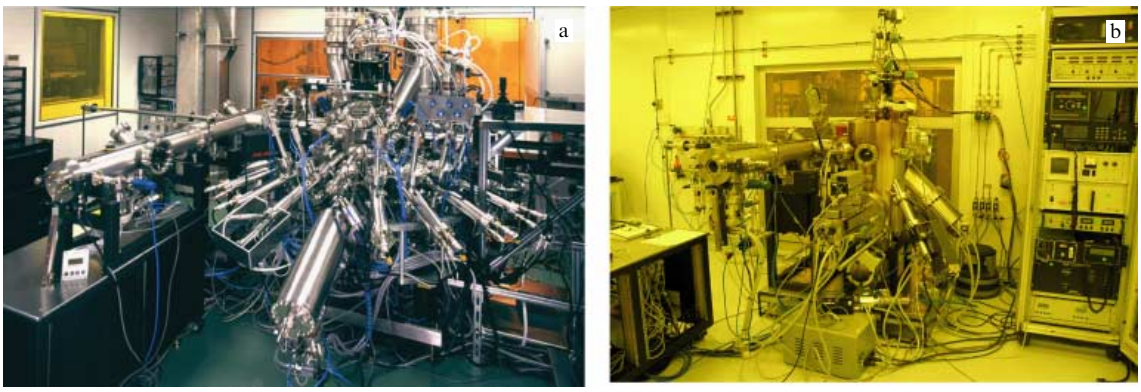

Figure 1. (a) The growth chamber of the MBE system at BNL is equipped with 16 metal atom sources, a pure ozone source (providing high oxidation power in high vacuum), a scanning quartz-crystal rate monitor, a 16-channel atomic absorption spectroscopy system, a scanning RHEED system, and a time-of-flight ion scattering and recoil spectroscopy system. (b) The processing chamber that allows for key lithographic steps (metallization, insulation, ion-milling, and ashing) to be done without breaking vacuum. It is located in a clean room which allows the substrates to be cleaned in a class-100 dust-free environment and loaded into the system for thin film deposition and processing.

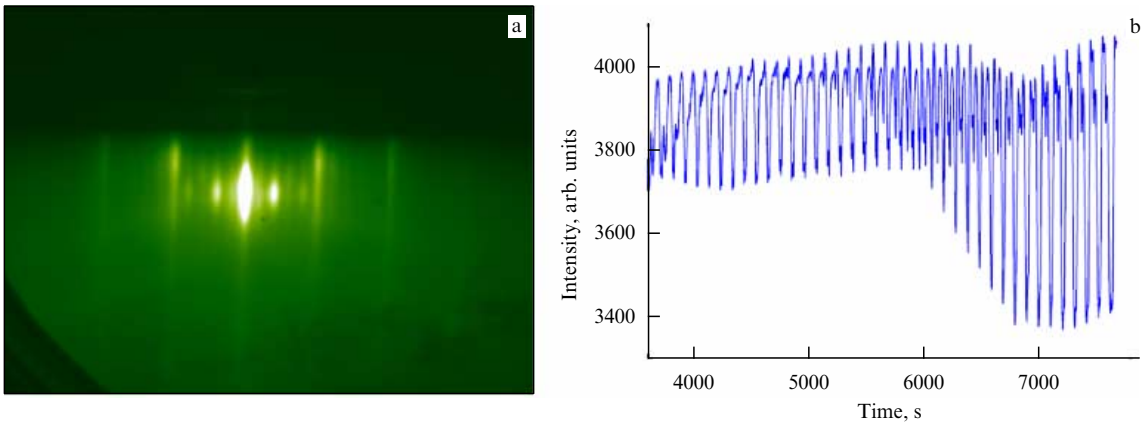

Figure 2. (a) A RHEED image from a thin film of $La_{2-x}Sr_xCuO_4$, viewed along the (100) crystallographic direction. The very bright spot near the center comes from the specular reflection. (b) RHEED oscillations during growth of this film. The intensity of reflectance is measured at the specular spot, as a function of time. The oscillations originate from periodic surface roughening and smoothing. The maximum reflectance is approximately constant, evidencing that the atomic smoothness of the surface is maintained as the film grows thicker. The beating comes from a small error in the absolute growth rate — the shutter opening time was not perfectly adjusted to deposit exactly one atomic mono-layer at a time.

the source temperature is kept constant to a high precision. This mode of operation provides for much better accuracy than the traditional one of adjusting the atomic fluxes by changing the source temperature, because the thermal response is much slower (and oscillatory). The 16 independent AAS channels, one for each source, can all of be operated simultaneously, since the wavelength filtering ensures that there is no cross-talk between different channels.

A Reflection High Energy Electron Diffraction (RHEED) system provides real-time information on the crystalline structure of the surface. A typical diffractogram is shown in Fig. 2a.

A Time-of-Flight Ion Scattering and Recoil Spectroscopy (TOF-ISARS) system is also integrated within the growth chamber. It provides quantitative information on the chemical composition of surface layers in real-time during film growth [5]. The principle of operation is as follows: a source of ions (e.g., K^+) provides a monochromatic ($E = 10$ KeV) beam, which is chopped by electrostatic steering. Each time the beam hits the collimator a bunch of ions makes it through and we monitor accurately their time of arrival at a multichannel detector. The projectile ions hit the surface of the film and get scattered; one can measure their energy and momentum. This is called Ion scattering spectroscopy (ISS) and it is similar to the more familiar Rutherford backscattering spectroscopy (RBS), except that here the ions impinge at the surface with a low energy and at a nearly grazing angle. This provides for great surface sensitivity — we are probing only one or two top atomic monolayers. Some ions and neutral atoms are sputtered away from the surface, collected and mass-analyzed. This is called Direct Recoil Spectroscopy (DRS) and it provides information on the chemical composition of the surface. The TOF-ISARS apparatus built into our MBE system has four detectors at different angles, including a Mass Spectroscopy of Recoiled Ions (MSRI) analyzer. The later is supplied with a built-in automatic compensation for multiple scattering so that it can 'focus in time' the ions of the same mass irrespective of their energy and thus achieve the highest mass resolution — enough to resolve all the naturally occurring isotopes, see Fig. 3.

An important integral part of the MBE system at BNL is the processing chamber shown in Fig. 1b. It contains several

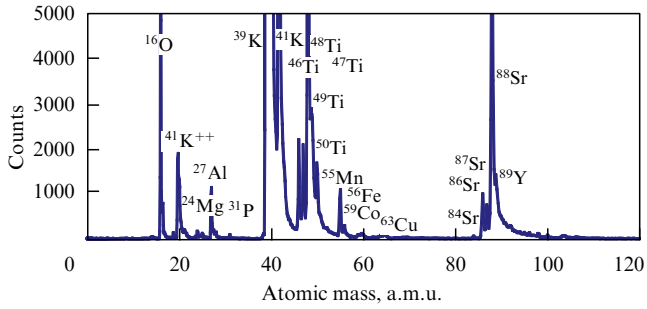

Figure 3. Mass spectrum of ions at the surface of a $SrTiO_3$ substrate obtained using the MSRI analyzer of TOF-ISARS system. The mass resolution is high enough to clearly identify the naturally occurring isotopes. This particular substrate was contaminated from exposure to a hot stainless-steel holder in a different chamber and all the contaminant ions can be seen. TOF-ISARS provides precious information on the chemical composition of the film surface, *in situ* and during film growth.

tools for lithographic operations: (i) a 5-pocket electron-beam evaporator, used to deposit metallization (usually Au, Ag, or Nb) and insulation layers (Al_2O_3, SiO_2, MgO), (ii) an oxygen plasma source for ashing photoresist residue and cleaning the surface *in-situ*, and (iii) a two-inch-diameter ion-beam source that enables lithographic features to be fabricated by ion milling. A liquid-nitrogen cooled, 6-degree-of-freedom sample manipulator allows for complex rotation patterns. The large-diameter, parallel ion beam makes it possible to fabricate deep trenches and other vertical lithographic features, as well as very shallow (low-angle) ramps. The processing chamber is located in a clean room; this allows the substrates to be cleaned in a class-100 environment and loaded dust-free into the system for subsequent film deposition and processing. The two chambers are connected by a 20-foot long transfer chamber that can maintain ultra-high vacuum on the 10^{11} Torr scale.

2. Atomically smooth HTS films grown by MBE

Leveraging on these advances in the apparatus and in the technique, we have succeeded in developing the technology for reproducible fabrication of atomically smooth films of cuprate superconductors and other related complex oxides

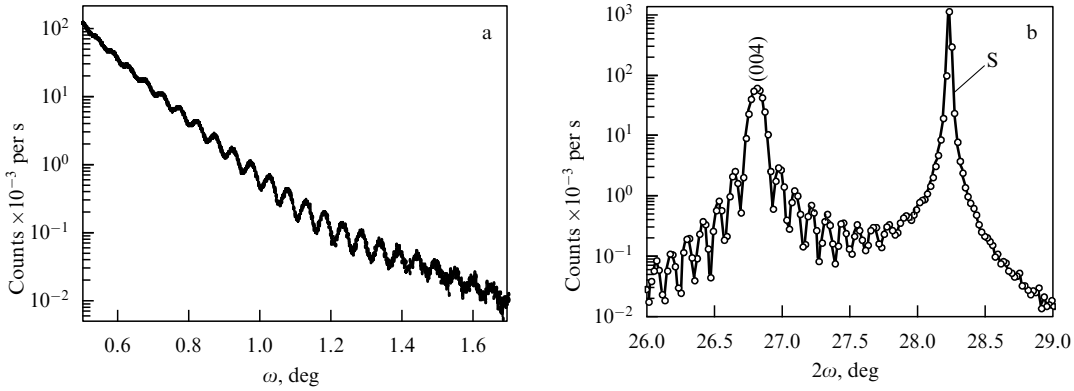

Figure 4. (a) Low-angle X-ray reflectance oscillations from a $La_{1.85}Sr_{0.15}CuO_4$ film, 78 nm thick, grown on top of a LaSrAlO4 substrate [4]. These oscillations are analogous to the Fabry – Perot interference between light beams reflected from two mirrors that are parallel and perfect on the scale of the wavelength of light. (Here, $\lambda = 1.54$ Å) (b) X-ray diffraction (the $\Theta - 2\Theta$ scan) near the (004) reflection from a $La_{1.85}Sr_{0.15}CuO_4$ film. Finite thickness oscillations are seen as side-bands to the strong Bragg reflections from the film and the substrate. The difference in angle between the two successive sidebands is determined by the total film thickness, while the position of Bragg peaks is determined by the lattice constant.

[5 – 8]. The key indicators are undamped RHEED oscillations observed during film growth, spectacular finite-thickness interference patterns seen in X-ray scattering, and flat, defect-free surfaces directly observed in scanning electron microscopy and atomic force microscopy (AFM) images.

In Fig. 2a we show a RHEED pattern observed from a very flat $La_{1.85}Sr_{0.15}CuO_4$ (LSCO) film during growth. Notice that the pattern is dominated by a very strong and sharp spot from the specular reflectance; this is an indication that the surface is very smooth. If we measure the reflectance intensity at this spot as a function of time, we observe regular oscillations such as seen in Fig. 2b. These oscillations come from periodic surface roughening and smoothing. The initial substrate surface is atomically flat. When the first layer is nucleated, the surface gets progressively rougher as the islands get more numerous. However, once that a half of the surface is covered, the reflectance starts increasing again as the islands grow in size and coalesce, until the layer is completed, at which point the reflectance reaches the second maximum. If the film growth is perfect, after each such cycle the surface should get atomically smooth again, and the reflectance maximum should not decrease with time. In contrast, a decrease in reflectance and damping of the intensity of oscillations is a signal of progressive roughening of the film surface as the growth proceeds. This is apparently not the case in Fig. 2b; indeed, in many instances, we have observed the maximum RHEED intensity to increase with the film thickness. On occasion one can discern beating, i.e., the presence of the second, much longer period in RHEED oscillations, as seen in Fig. 2b; this indicates a small error in the absolute calibration of deposition rates, which can be evaluated from such a graph and corrected subsequently.

In Fig. 4a, we show the X-ray reflectance measured at very low (nearly grazing) angles from a very flat LSCO film grown by MBE. Pronounced oscillations are seen in the intensity as a function of the angle of incidence. This is analogous to Fabry – Perot fringes that result from interference between the light beams reflected from two mirrors. Fabry – Perot oscillations are pronounced only if the two mirrors are parallel and perfect on the scale of the wavelength of light employed. Here, the wavelength of the X-ray radiation is 1.54 Å. In Fig. 4b we show the standard $\Theta - 2\Theta$ diffraction pattern taken at a larger angle from a similar film. Apart from the very strong Bragg reflections that originate in diffraction from the film and the substrate, one can see pronounced sidebands, the so-called finite-thickness oscillations. The separation between the Bragg peaks is determined by the film lattice constant, while the difference in angle between the two successive sidebands is determined by the total film thickness. This is essentially the same phenomenon as what is shown in Fig. 4a; the interference occurs between the X-rays reflected from the film surface and from the film/substrate interface. Indeed, this indicates that the two surfaces are flat and parallel to one another on the Å length scale.

In Fig. 5 we show an AFM image of a LSCO film grown on a $SrTiO_3$ substrate by MBE. Apparently the film is atomically flat, except for some one-unit-cell tall steps. These originate from the substrate; the commercially available ones are never polished exactly at the desired crystallographic plane but rather miscut by 0.1 – 0.5°. This generates few hundred angstroms wide terraces at the substrate surface that are typically separated by one-unit-cell tall steps. This causes occurrence of similar steps and terraces at the surface of growing film. Nevertheless, in the film shown in Fig. 5, the rms surface roughness over the area as large as 2,500 μm^2 was no more than 2 – 3 Å. This is essentially a single atom height, definitely much less than the 1 UC height, which in LSCO is $c_0 = 13$ Å.

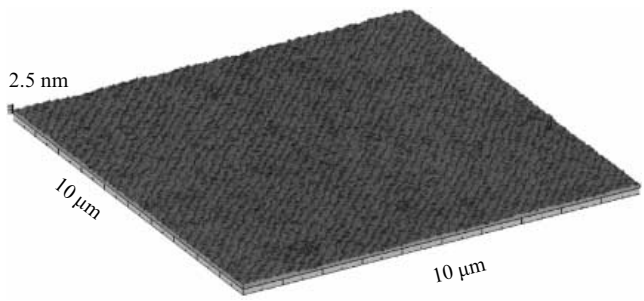

Figure 5. Atomic force microscopy image of a $La_{1.85}Sr_{0.15}CuO_4$ film, 78 nm thick, grown on top of a $LaSrAlO_4$ substrate [4]. It shows terraces, about 300 nm wide, between one-unit-cell-tall steps, as a consequence of the slight (0.1°) miscut of the substrate. The rms surface roughness of this film was less than 0.3 nm – essentially just a single atom height and much less than the unit cell height, $c_0 = 1.3$ nm – over the area of 2,500 μm^2.

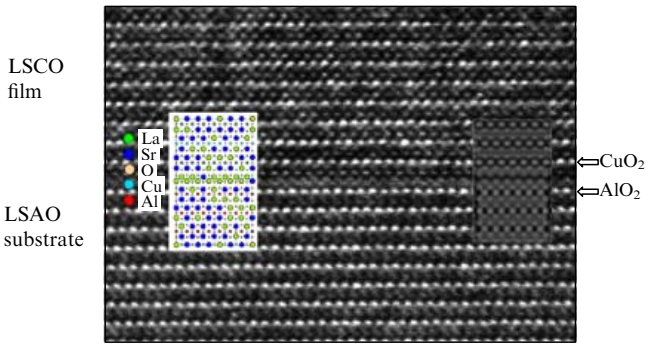

Figure 6. A cross-section image obtained by high-resolution Transmission Electron Microscopy (HR-TEM) of a $La_{1.85}Sr_{0.15}CuO_4$ film grown by MBE on $LaSrAlO_4$ substrate [9]. The micrograph shows formation of an unusual 'interface compound' — the sequence of reconstructed atomic layers that compensate for the polarization discontinuity at the interface. Knowledge and control of the right atomic-layer sequence is the secret of perfect hetero-epitaxy.

One important secret of perfect heteroepitaxy is the right sequence of atomic layers at the interface between the substrate and the film. If both are complex oxides, frequently one can observe formation of an interface layer of a third compound — sometimes a rather unusual one that does not exist in the bulk form. An instructive illustration is provided in Fig. 6 that shows an atomic lattice image of the interface between a LaSrAlO4 substrate and a $La_{1.85}Sr_{0.15}CuO_4$ film obtained by high-resolution transmission electron microscopy [9].

While atomically smooth HTS films were occasionally obtained in other laboratories, our group has been achieving this on a day-to-day basis. In the last year or so, the yield was essentially 100% (except for an occasional re-calibration growth right after we recharge the sources). This high yield of useful samples speeds up learning and enables fast progress. Thus it became possible to perform some unique experiments that are described in what follows.

3. HTS and the antiferromagnetic (AF) state

We have studied proximity effects between the HTS and the anti-ferromagnetic (AF) states, and found that they separate sharply, on the atomic scale [7]. The key piece of evidence is presented in Fig. 7. Trilayer junctions (Fig. 7a) were fabricated with HTS electrodes made out of LSCO ($T_c \approx 45$ K) and the insulating barrier consisting of just a single unit cell thick La_2CuO_4 (LCO) layer. As seen in Fig. 7b, there was no observable supercurrent even in the largest (80 μm diameter) junctions. The difference between three families of curves comes from different junction cross section; the area scaling was excellent and so was the uniformity among the junctions of the same nominal diameter [7]. This illustrates well the perfection of atomic layering: a single unit cell (1UC) thick barrier has no pinholes over macroscopic area. Note that we have revisited these findings recently at BNL and reproduced them over a dozen times, without a single exception.

In terms of fundamental physics of HTS, the significance of the above result is that it shows that the HTS phase and its 'parent' AF insulator phase do not mix but rather phase-separate very sharply, on the length scale of 1 Å. This corresponds to the AF barrier height of about 1 eV. Hence, the two phases are not degenerate (or nearly degenerate) in energy contrary to what has been postulated in a class of theoretical models for HTS.

The above experimental finding also revealed that there was no depletion/accumulation of charge between the superconducting (LSCO) and insulating (LCO) layers. The fact that the charge carriers stay in the doped layers indicates that the Coulomb interaction must be poorly screened along the *c*-axis. The same conclusions follow also from the 'reverse' experiment, illustrated in Fig. 8: a superlattice containing 1UC thick HTS layers separated by thicker insulating LCO layers has a high T_c and a sharp superconducting transition.

Independent verification of these statements came from a nice set of materials-physics experiments performed by I Felner and his group [10] on La-Sr-Ru-Cu-O (Ru-1212, 1222, -2212) compounds. These materials are unusual insofar that they show simultaneously high-temperature supercon-

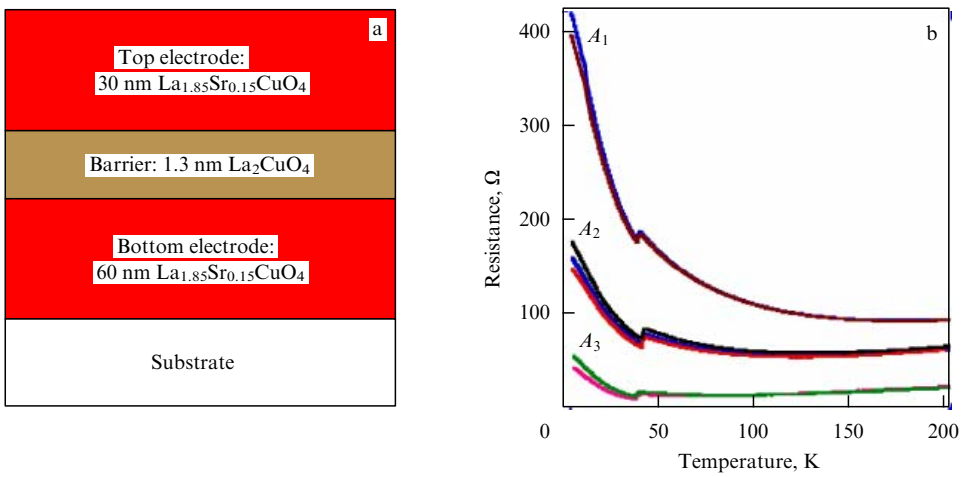

Figure 7. (a) A sketch of a trilayer SIS junction with one-unit-cell (1UC) thick LCO barrier. (b) The temperature dependence of resistance in three sets of such junctions with the mesa cross-section $A_1 = 1.8 \times 10^{-6}$ cm^2, $A_2 = 3.1 \times 10^{-6}$ cm^2, and $A_3 = 7.1 \times 10^{-6}$ cm^2, respectively [7]. Note that below ~ 40 K the LSCO electrodes and leads are superconducting and the voltage drops only across the LCO barrier. The absence of supercurrent and the high resistance seen even at the lowest temperature measured (4.2 K) indicate the absence of pinholes and shorts, but also that the LCO barrier height is substantial (about 1 eV).

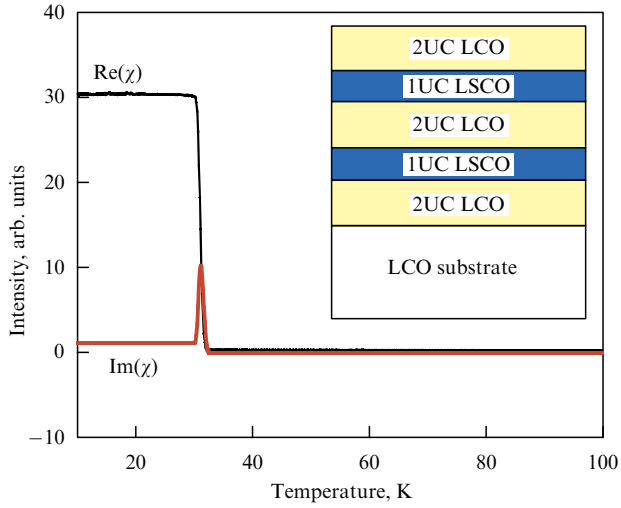

Figure 8. The temperature dependence of susceptibility (measured by the mutual inductance technique) of a superlattice film synthesized by alternating two-unit-cell thick layers of insulating La_2CuO_4 with one-unit-cell thick layers of $La_{1.85}Sr_{0.15}CuO_4$. Inset: the schematic structure of superlattice film [7].

ductivity with T_c as high as 40 – 50 K that resides in the CuO_2 layers, and antiferromagnetism with $T_N = 125-180$ K that originates from Ru magnetic moments. Felner et al. have demonstrated that T_c and T_N can be tuned independently of one another by site-selective chemical doping. In other words, HTS state is not influenced by the presence or absence of the AF state and v.v., even though the layers in which these states reside are separated by just few Ångstroms. Clearly, this would not be possible if the two states were degenerate and mixed over a large length-scale; in that case, one would only see a homogeneous mixture of the two. Given the experimental fact that the two states apparently do phase-separate on an extremely short length scale, it is not surprising that one can have in some samples many small or large islands of one phase in the matrix of the other phase, and be able to detect signals of their simultaneous presence. But this should not be confused with the two order parameters coexisting — i.e., existing in the same space at the same time as has been claimed in some papers. It is not obvious to the present author how a material could be an insulator and a superconductor simultaneously.

4. HTS and the pseudogap (PG) state

Next, we have studied proximity effects between the HTS and the so-called pseudo-gap (PG) state that is realized in underdoped cuprates. In stark contrast to the HTS-AF case, here we indeed observed [11] the so-called Giant Proximity Effect (GPE). When an underdoped layer is sandwiched between two optimally doped HTS layers, supercurrent can flow even through very thick 'barrier' layers.

In Fig. 9a, we have sketched a trilayer with the superconducting (S) electrodes made of LSCO with $T_c \approx 45$ K. The normal-metal (N′) barrier were made of underdoped $La_2CuO_{4+\delta}$ (LCO) with the typical $T_c \approx 25$ K and thickness $d = 200$ Å. The $I-V$ measurements were made as the function of temperature and we found that the devices behaved as SN′S Josephson junctions for $T_c' < T < T_c$. In Fig. 9b, we show how such a junction responds to microwave radiation ($\nu = 20$ GHz) at $T = 30$ K, i.e., above the T_c' of the barrier. One can see clear and sharp current jumps (Shapiro steps) at the voltages given by $nh\nu = (2e)\,V$, where $n = 1, 2, 3, \ldots$ This is clearly a *single* Josephson junction — there are no multiple voltage jumps characteristic of intrinsic junctions or a series of random weak links.

We believe that this GPE is genuine. In Ref. [11] we provided firm evidence that we have eliminated the key experimental hurdle in this field — micro-shorts, i.e., superconducting filaments connecting the electrodes. Our HTS trilayer junctions are free of any secondary phase precipitates and have atomically smooth interfaces — the rms surface roughness is much smaller than the barrier thickness. Further, we think that GPE is not the conventional S – N proximity effect. In our HTS-based SN′S junctions supercurrent flows across a barrier 100 times thicker than the superconducting coherence length, the mean-free-path of the charge carriers,

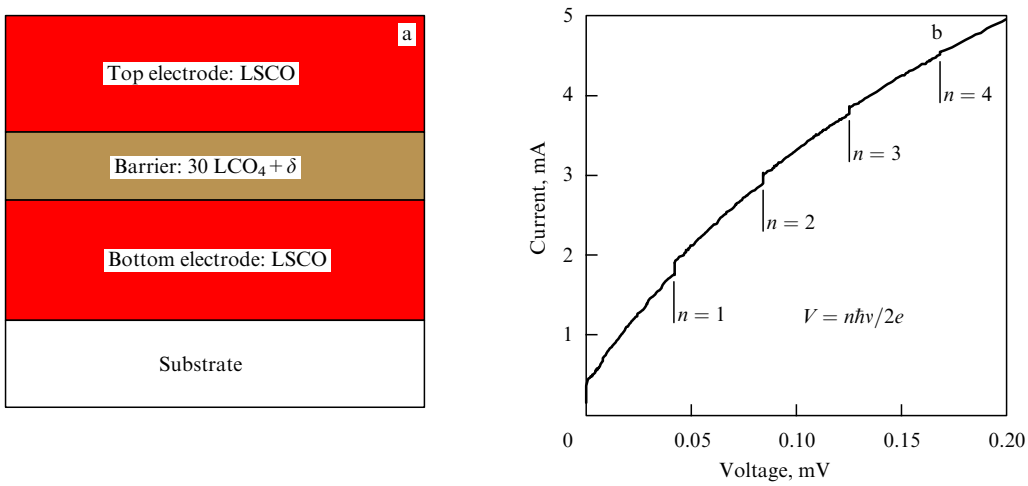

Figure 9. (a) (a) A schematic cross-section of a SNS trilayer junctions with the barrier thickness $d = 200$ Å. (b) The Shapiro steps induced in such a junction at $T = 30$ K (i.e., well above T_c of the N′ layer) by microwave radiation ($\nu = 20$ GHz) [11]. The steps occur at the voltages given by $V = nh\nu/2e$, for $n = 1, 2, 3, \ldots$, as expected for a single Josephson junction. This implies a 'Giant Proximity Effect' — the length scale is two orders-of-magnitude larger than what one would expect from the conventional theory and from the fact that both the coherence length in the HTS electrodes and the mean free path in the N′ layer are extremely short.

and the induced coherence length in N that one would have inferred from the conventional theory of the proximity effect. GPE may be the first really unconventional property of the *superconducting* state in the cuprates, and it imposes a new experimental constraint on the theory of HTS. We are continuing investigation of this effect at BNL, now using as the barrier underdoped LSCO with various level of Sr doping. So far the results seem consistent with our previous findings; hopefully we will be able to report some further advances before too long.

5. Interface Superconductivity

Superconductivity confined to nanometer-thick layers has been a long standing goal but very difficult to achieve. In ordinary metals the high electron density restricts carrier depletion and accumulation to a region much narrower then the superconducting coherence length. In copper oxides, the carrier density is low, the critical temperature high and the coherence length very short, so this provides a unique opportunity provided one can fabricate atomically perfect layers and interfaces. We have recently succeeded in fabricating virtually perfect heterostructures consisting of a metal ($M = La_{1.55}Sr_{0.45}CuO_4$) and an insulator layer ($I = La_2CuO_4$), neither of which is superconducting by itself — yet in the bilayers we reproducibly observe $T_c = 30$ K. By virtue of digital control of the layer thickness inherent to our atomic-layer MBE technique, we have established that in such heterostructures the HTS phase is confined within 1 – 2 unit cells from the interface. The detailed account of results, including the thickness and sequence dependence, the surface characterization by RHEED and TOF-ISARS etc., should be published soon [12]. One important finding is that interfaces appear to 'cross-talk' over large distances, as much as 500 Å — yet another indication that in cuprates the long-range Coulomb interaction is poorly screened along the *c*-axis.

We anticipate that the discovery of interface superconductivity will trigger further advances in several directions. For one, this makes reproducibly available robust ultra-thin HTS films, possibly including some with superconductivity confined to just a single CuO_2 plane. This should allow for a clean study of topological excitations such as vortex-anti-vortex pairs fluctuations in a 2D HTS gas. It may open the door to fabrication of practical three-terminal superconducting devices. Last but not least, this removes at least one important psychological barrier on the path to realization of Ginzburg's multilayer excitonic superconductor [1, 2]. We have demonstrated now that HTS can be sustained within a single unit cell layer, and that it can be influenced and enhanced across the interface from the proximal layer. The future will tell how far one can go using interface engineering to manipulate and control the inter-layer interactions.

6. Direct experimental evidence for strong electron-phonon coupling

Ever since the discovery of HTS in 1986, it has been a matter of heated debate whether coupling of charge excitations to the crystal lattice in cuprates is weak and essentially irrelevant or strong and crucial for the phenomenon. The opponents argue that there is essentially no oxygen isotope effect on T_c at optimal doping and hence no change in the ionic kinetic energy upon condensation, and that the electron – phonon coupling constant λ estimated from transport measurements or determined from *ab initio* band-structure calculations is small, $\lambda \approx 0.3$ in LSCO and $\lambda \approx 0.1$ in YBCO [13 – 19]. The proponents point out that a large (even too large) oxygen isotope effect is seen at other doping levels and in other physical observables (penetration depth, superconducting gap, pseudogap, effective mass, etc.), that large phonon anomalies have been detected in neutron scattering, and that tunneling spectroscopy shows phonon features coupled to the superconducting gap [20 – 31]. Other arguments, theoretical and experimental, abound on both sides of the divide.

Recently it has been discovered that intense short light pulses cause 'colossal' (larger then thermal) expansion in lanthanum cuprate films [32]. In this experiment, a thin LCO film was exposed to intense femtosecond (fs) light pulses. The evolution of crystallographic structure was monitored in real time by pulsed electron diffraction. The principle of the experiment is illustrated in Fig. 10a. The key result is shown in Fig. 10b: the c-axis lattice constant intermittently expands by as much as 0. Å. This lattice expansion is colossal if one compares it to the amplitudes of thermal lattice vibrations — the thermal expansion coefficient in LCO is 8.5×10^{-6} K^{-1}, so normally the crystal should have molten.

The fact that photo-doping induces colossal expansion implies very strong coupling of the lattice to charge-transfer excitations. This conclusion does not depend on theoretical modeling and follows essentially directly from the experimental data. Lattice expansion cannot come from magnons, plasmons, excitons, etc. More specifically, expansion along the *c*-axis can only come from *c*-axis *longitudinal acoustic phonons* (cLAPs). Strong coupling to cLAPs is unusual and characteristic of charged-layer superlattice structures; yet, it has been overlooked so far.

On the other hand, one can also conclude from rather general and detail-insensitive theoretical considerations [33] that the coupling to out-of-plane optic vibrations also must be strong. Generally, lattice expansion accompanies a reduction in crystal cohesion energy. In cuprates (and other related oxides) the cohesion is primarily of ionic origin and can be estimated as

$$U = \frac{e^2}{2} \sum \frac{q_i q_j}{|r_i - r_j|} + \frac{1}{2} \sum A_{ij} \exp\left(-B_{ij} |r_i - r_j|\right).$$

The first term is the Madelung energy (U_M); r_i and r_j denote the positions of the ions and q_1, q_j are their charges. The second term is the core repulsion energy modeled as the sum of nearest-neighbors repulsion terms in the standard Born – Mayer form. The sums are over all i, j with $r_i \neq r_j$. This simple framework accounts well for a range of properties — the cohesion energy, the charge-transfer gap, the crystal structure, the compressibility, and even the critical pressure for the orthorombic-to-tetragonal phase transition. It is convenient to fix the parameters A_{ij} and B_{ij} in such a way that the minimum of total energy coincides with the experimentally determined structure. Van der Waals interactions and covalency of the in-plane Cu – O bonds are included implicitly and are very small ($< 1\%$) terms anyway. Then one can allow for the (small) changes in q_i caused by chemical or photo-doping and predict the induced lattice distortions. We have tested how this model works in the case of chemical doping, where comprehensive neutron diffraction data have been reported and provide detailed information on the dependence of all atomic positions on the doping level x. We have found quantitative agreement without any fitting. To

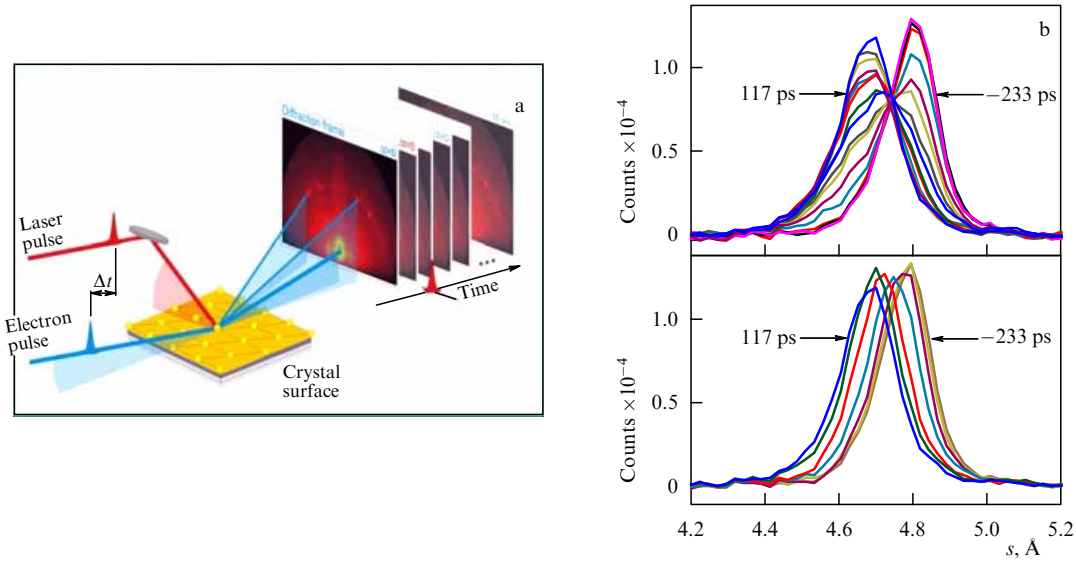

Figure 10. (a) Schematics of the ultrafast RHEED experiment of Gedik et al. [32]. An $La_2CuO_{4+\delta}$ film grown by MBE was photo-excited by intense short light pulses and the surface structure was analyzed using pico-second electron diffraction. By scanning the delay time one obtains RHEED 'movies' that show time-resolved changes in the crystal structure. (b) The main result: upon intense photo-illumination, the film expands along the c-axis by as much as 0.3 Å ($\sim$ 2.5%).

the first order, the ionic displacements are of purely electrostatic origin, i.e., just the consequence of the changes in ionic charges. Applying the same algorithm to photo-doping of epitaxially constrained films, we predict the *c*-axis expansion comparable to the one observed by Gedik et al., see Fig. 11. Moreover, the same simulation predicts significant intra-cell distortions, i.e., *c*-axis displacements of La and apical oxygen (O2) ions. In terms of the normal modes of the system, this implies strong coupling to two Raman active modes of A_{1g} symmetry, viz. vibrations of the La dumbbell at about 230 cm^{-1} and of the O2 dumbbell at 440 cm^{-1}.

The above conclusions may sound strange at the first glance. In the experiment of Gedik et al., the pump light beam was hitting the film with the electric field *parallel* to the CuO_2 planes, and yet we claim that this causes ionic motion in the *perpendicular* (out-of-plane) direction. In fact, this had been observed long ago but just overlooked. In Fig. 12, we reproduce Raman scattering data from Ref. [34]. The first panel (Fig. 12a) shows that the intensity of the apical-oxygen vibration mode at $\sim$ 500 cm^{-1} depends sensitively on the wavelength of the laser light. The second panel (Fig. 12b) shows in more detail how this intensity changes as a function of the photon energy, and compares this to the absorption coefficient in the material (for the same angle of incidence). The two spectral curves track one another; this is a clear indication of Resonant Raman scattering. The bizarre point (that even we missed ourselves in the original paper) is that the electric field of the light was *in-plane* and the ionic motion *out-of-plane*. A signature (anti-resonance) of *c*-axis phonons has been observed in *ab*-plane reflectance spectra as well [35]. Barring experimental artifacts, the only explanation I could think of is that the two subsystems, electrons and ions, are strongly coupled. If this is indeed the case, then if the mobile charges redistribute within the CuO_2 plane, the out-of-plane ions must move accordingly — and conversely, if these ions vibrate along the *c*-axis, this must cause a concomitant redistribution of the electron charge density within the CuO_2 plane.

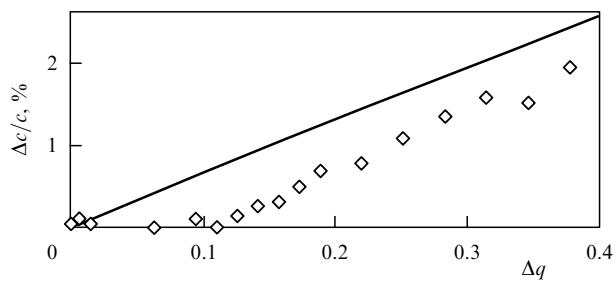

Figure 11. Colossal photo-induced expansion along the crystallographic *c*-axis in an MBE-grown $La_2CuO_{4+\delta}$ film: (◇) the experiment [32]; (the solid line) the calculations [33].

The root cause of this strong coupling is the Coulomb interaction which is indeed poorly screened in the *c*-axis direction — the fact I knew ever since recording the first polarized reflectance spectra of $YBa_2Cu_3O_7$ (YBCO) and $Bi_2Sr_2CaCu_2O_8$ (BSCCO) single crystals back in 1988–1989. In the *ab*-plane polarization, BSCCO looks like a metal (albeit a bad, over-damped one), but in the *c*-axis polarization it looks like the kitchen salt — there is no Drude peak, just strong dipole-allowed phonons. It took well over a decade before the (Josephson) plasma frequency along the *c*-axis in BSCCO was actually measured because it occurs in the microwave region — over an order-of-magnitude lower than the frequency of the optic phonons under discussion here.

The main problem here is that we expect the same effects to occur in other structurally and chemically similar ionic oxides. Indeed, some of these like e.g. $La_{0.5}Sr_{0.5}CoO_3$ and $Ca_{0.5}Sr_{0.5}RuO_3$ have infrared and Raman spectra (and other physical properties) quite alike to those seen in the cuprates [36]. However, none of these other oxides show HTS if they are superconducting at all. So clearly for HTS it is not enough that the electrons are strongly coupled to the lattice (including

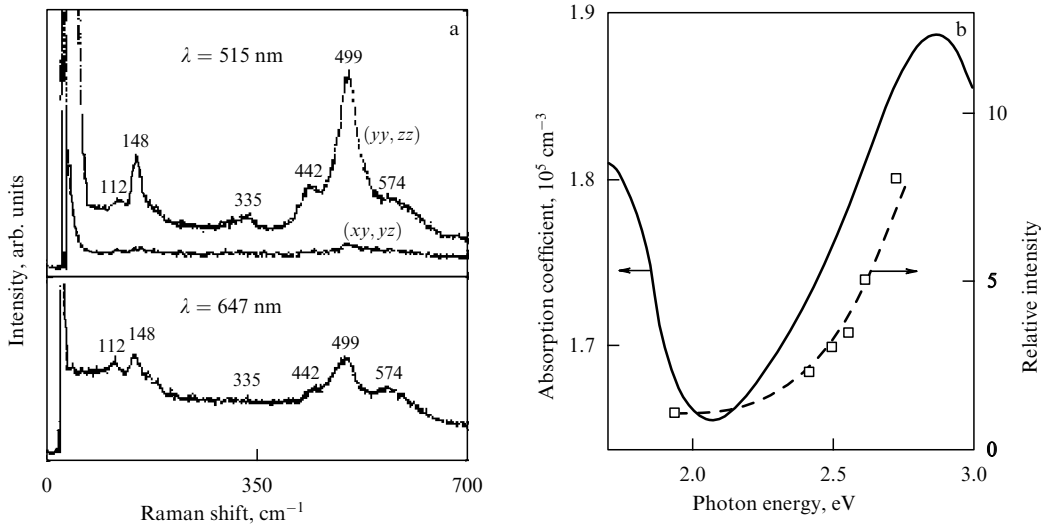

Figure 12. Raman scattering spectra of a $YBa_2Cu_3O_7$ film [33]. Note that the intensity of the strong feature at 499 cm^{-1}, the *c*-axis vibration of the apical oxygen, strongly depends on the wavelength of light. (b) A comparison of the intensity of this Raman-active mode to the absorption coefficient measured in the same sample as the function of photon energy [34].

the out-of-plane modes) — there ought to be something very specific to the cuprates that we are missing here. Many researchers in the HTS field believe that this uniqueness is in the strong electron correlations, spin 1/2, and the large $J \sim 0.13$ eV. However, even if this is the case, it seems to me hazardous to ignore the fact that in-plane charge excitations are strongly coupled to *c*-axis lattice vibrations — that *these excitations cannot be separated* — since they are ultimately responsible for both the normal state conductivity and HTS. In particular, if one wants to understand the doping phase diagram, one should be aware of the fact that between the undoped and optimally doped cuprates the Madelung energy may change by more then 1 eV *per atom* [33]. It is thus not surprising to see e.g. transfer of spectral weight in optical conductivity upon doping from the high-energy (1 – 2 eV region) to the Drude peak at low frequency [37], but it is hard to see how one could describe this using just a low-energy effective Hamiltonian.

7. Fingerprints of a polaronic metal

If indeed the electron – phonon coupling is very strong, at low density of doped charge carriers this should lead to small polaron formation and some sort of hopping transport with semiconductor-like temperature dependence. What to expect at a high doping density is less clear theoretically. Almost half-a-century ago T. Holstein speculated that at low enough temperature (when $k_B T$ gets smaller then the polaron bandwidth) a 'polaronic metal' state with coherent transport should emerge [38, 39]. I am unaware whether this has ever been unambiguously observed in any material — and even whether it is a theoretically viable concept. On the other hand, if such a state existed I can say how it should look like to a spectroscopist.

Using the simplest possible toy model (classical and analytically solvable) of a non-interacting (Drude) gas of polarons one can indeed predict some unusual features in the optical spectra [40]. The reflectance should not show a sharp

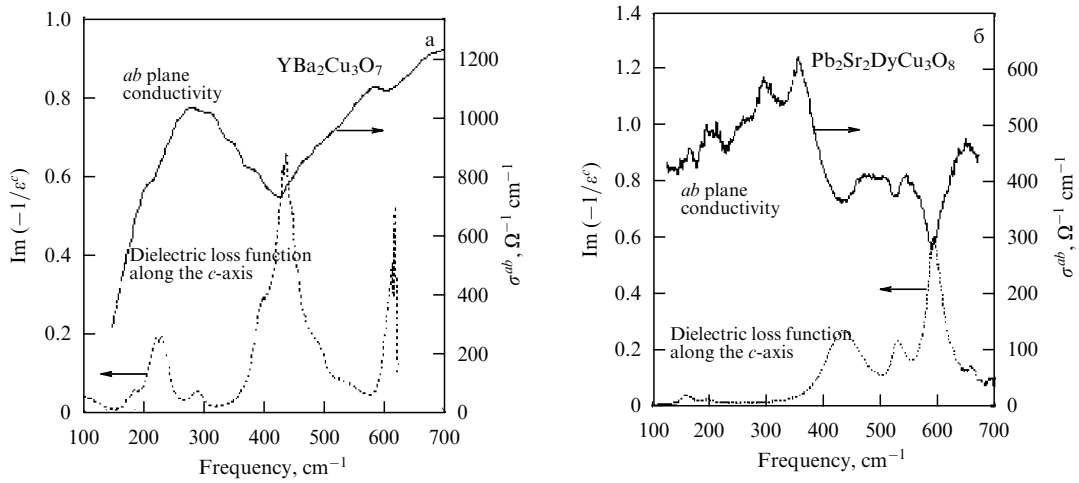

Figure 13. (a) The in-plane optical conductivity in $YBa_2Cu_3O_7$ shows minima that correspond exactly to the phonon peaks in the *c*-axis dielectric loss function; this may be indicative of strong coupling of out-of-plane phonons to the electrons in CuO_2 plane. (b) The same in $Pb_2Sr_2DyCu_3O_8$ [35].

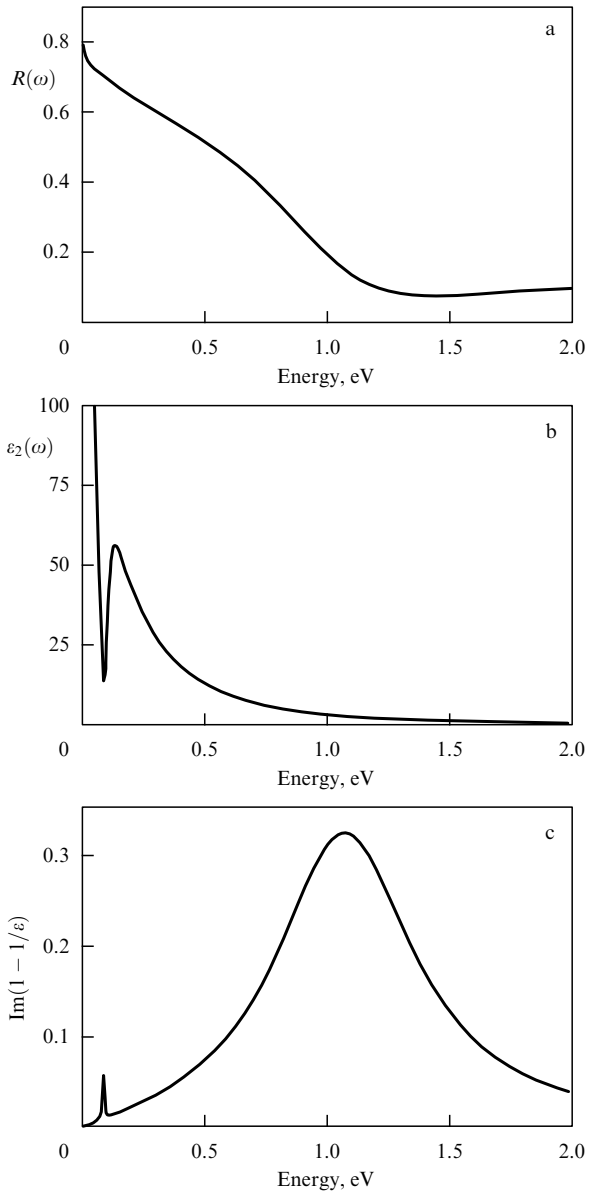

Figure 14. (a) The reflectance of a Drude gas of small polarons at high temperature. (b) At low temperature, the imaginary part of the complex dielectric function shows a pseudo-gap and (c) the dielectric loss function shows two distinct collective excitations, at high energy the usual plasmons and at low energy the longitudinal oscillations of the phonon 'clouds' [40].

plasma edge; at high frequencies well above the Franck–Condon ('undressing') transition the electron sees the large bare electron–phonon coupling and its motion gets overdamped, see Fig. 14a. More interesting things are expected to occur at low temperature and low frequencies: in the optical conductivity one would expect to see a pronounced minimum, something like a pseudo-gap, see Fig. 14b. This is related to the existence of second collective excitation in the polaron gas. At high frequency, there are plasma oscillations of essentially bare electrons. But since here we have an additional internal degree of freedom, i.e., the relative motion of the electron against its phonon cloud, there is a frequency at which the electrons don't oscillate (so there is no absorption) yet there are resonant longitudinal collective oscillations of the phonon 'clouds'. This excitation is not a plasmon, since it is charge-neutral. Neither is it a sound wave, since it is not acoustic — there is a finite restitution force. This prediction is not model-dependent — one should expect this from just counting the degrees of freedom. The new low-energy collective excitation should be observable at low temperature e.g. by high-resolution electron energy loss spectroscopy (HREELS) as a small sharp peak in the dielectric loss function, see Fig. 14c. This peak would be a clear fingerprint of the Polaron Metal — provided such an entity existed.

8. Conclusions

Based on our experiments with atomically smooth HTS thin films and heterostructures (multilayers, superlattices) we have concluded that HTS and AF states phase separate on Å scale while HTS and PG states mix over few orders-of-magnitude larger length scale. This indicates that HTS and AF states are well separated in energy while HTS and PG states must be almost degenerate.

Next, in such heterostructures we have observed interface superconductivity with a high T_c. It seems that HTS with the bulk T_c can be sustained in one-unit-cell thick cuprate layers. This discovery should have an impetus on studies of fluctuations in 2D superconductors as well as on HTS device physics. It also opens the field for study of HTS induced or enhanced by interactions and pairing across the interface, and putting to real test the decades-old prophecy of VLG.

Last but not least, picosecond diffraction experiments show colossal photo-induced expansion, which proves that there is strong coupling of in-plane charge excitations to c-axis acoustic phonons. Our model calculations indicate that out-of-plane optic phonons must strongly couple as well. We believe that this must be an important aspect of HTS physics in particular for understanding of the doping phase diagram.

More generally, we have shown that by atomic-layer engineering one can obtain unique samples and enable novel experiments to shed light on some basic physics problems such as the nature of HTS phenomenon.

Acknowledgment. The experiments at BNL were done in collaboration with G Logvenov, A Gozar, A Bollinger, and V Butko, and the numerical simulation in collaboration with Z Radovic and N Bozovic; their contributions were indispensable for the work reviewed here. I am also grateful for useful discussion and comments to V L Ginzburg, N Aschcroft, T H Geballe, M L Cohen, J C Phillips, J C Davis, J Zaanen, A Tsvelik, P Allen, and R Konik. This research has been supported by US DOE grant no. MA-509-MACA.

References

1. Ginzburg V L *Phys. Lett.* **13** 101 (1964)
2. Ginzburg V L *Zh. Eksp. Teor. Fiz.* **47** 2318 (1964) [*Sov. Phys. JETP* **20** 1549 (1965)]
3. Bozovic I, Eckstein J N, Virshup G F *Physica C* **235–240** 178 (1994)
4. Bozovic I *IEEE Trans. Appl. Superconduct.* **11** 2686 (2001)
5. Gozar A, Logvenov G, Butko V Y, Bozovic I *Phys. Rev. B* **75** 201402(R) (2007)
6. Bozovic I et al. *Phys. Rev. Lett.* **89** 107001 (2002)
7. Bozovic I et al. *Nature* **422** 873 (2003)
8. Abbamonte P et al. *Science* **297** 581 (2002)
9. He J et al. *J. Appl. Phys.* **101** 073906 (2007)
10. Felner I, in *Superconducting and Related Oxides: Physics and Nanoengineering V* (Proc. SPIE, Vol. 4811, Eds I Bozovic, D Pavuna) (Bellingham, Wash.: SPIE, 2002) p. 39
11. Bozovic I et al. *Phys. Rev. Lett.* **93** 157002 (2004)
12. Gozar A, Logvenov G, Bollinger A, Bozovic I (to be published)

13. Kapaev V V, Kopaev Yu V *Pis'ma Zh. Eksp. Teor. Fiz.* **68** 211 (1998) [*JETP Lett.* **68** 223 (1998)]
14. Belyavskii V I, Kopaev Yu V *Pis'ma Zh. Eksp. Teor. Fiz.* **73** 87 (2001) [*JETP Lett.* **73** 82 (2001)]
15. Belyavsky V I, Kopaev Yu V *J. Supercond. Nov. Magn.* **19** 251 (2006)
16. Leggett A J *Nature Phys.* **2** 134 (2006)
17. Zaanen J et al. *Nature Phys.* **2** 138 (2006)
18. Scalapino D J *J. Supercond. Nov. Magn.* **19** 195 (2006)
19. Anderson P W *Science* **316** 1705 (2007)
20. Ginzburg V L, Maksimov E G *Physica C* **235 – 240** 193 (1994)
21. Alexandrov A S, Mott N *Polarons and Bipolarons* (Singapore: World Scientific, 1995)
22. Zhao G-M et al. *Nature* **385** 236 (1997)
23. Müller K A *J. Supercond.* **12** 3 (1999)
24. Ginzburg V L *J. Supercond.* **13** 665 (2000)
25. Kulić M L *Phys. Rep.* **338** 1 (2000)
26. Abrikosov A A, in *Superconducting and Related Oxides: Physics and Nanoengineering V* (Proc. SPIE, Vol. 4811, Eds I Bozovic, D Pavuna) (Bellingham, Wash.: SPIE, 2002) p. 1
27. Ponomarev Ya G, Maksimov E G *Pis'ma Zh. Eksp. Teor. Fiz.* **76** 455 (2002) [*JETP Lett.* **76** 394 (2002)]
28. Maksimov E G, Dolgov O V, Kulić M L *Phys. Rev. B* **72** 212505 (2005)
29. Phillips J C *Phys. Rev. B* **71** 184505 (2005)
30. Lee J et al. *Nature* **442** 546 (2006)
31. Newns D M, Tsuei C C *Nature Phys.* **3** 184 (2007)
32. Gedik N et al. *Science* **316** 425 (2007)
33. Radovic Z, Bozovic N, Bozovic I *Phys. Rev. B* **77** 092508 (2008)
34. Kirillov D, Bozovic I, Char K, Kapitulnik A *J. Appl. Phys.* **66** 977 (1989)
35. Reedyk M, Timusk T *Phys. Rev. Lett.* **69** 2705 (1992)
36. Bozovic I et al. *Phys. Rev. Lett.* **73** 1436 (1994)
37. Uchida S et al. *Phys. Rev. B* **43** 7942 (1991)
38. Holstein T *Ann. Phys.* (New York) **8** 325 (1959)
39. Holstein T *Ann. Phys.* (New York) **8** 343 (1959)
40. Bozovic I *Phys. Rev. B* **48** 876 (1993)

PACS numbers: **74.62. – c**, **74.40. – b**, **74.78. – w**

DOI: 10.1070/PU2008v051n02ABEH006467
DOI: 10.3367/UFNr.0178.200802h.0190

Structural design of superconductors based on complex copper oxides

E V Antipov, A M Abakumov

1. Introduction

The design of new materials with important physical properties is one of the challenging problems of modern science. A variety of approaches are being developed in order to overcome labor-consuming exhaustive search of chemical compositions and synthesis conditions and to optimize the solution to this problem. Structural design is one of the most effective methods. This method involves an analysis of chemical composition – structure – property relations for a certain class of materials, possible structure types for a set of chemical elements that can be used to form the required crystal structure, the coordination environment of atoms in the structure, and the character of bonds between various atomic groups. Researchers from the Inorganic Crystal Chemistry Laboratory of the Chemical Department of Moscow State University used a structural design to search for new high-temperature superconductors based on complex copper oxides. In this report, we do not consider the crystal chemistry of high-temperature superconductors in detail. The main purpose is to describe the crystal chemistry principles of designing new superconductors that were used to fabricate new members of this unique family of materials and to predict ways to optimize their properties.

2. Structure and strategy of searching for new high-temperature superconductors based on complex copper oxides

Studying the relation between the composition, structure, and properties of numerous copper-containing high-temperature superconducting (HTSC) oxides has allowed formulating the following structural and chemical criteria required for the appearance of these properties:

(i) a layered structure in which (CuO_2) layers represent an infinite network of copper – oxygen CuO_4 squares connected by their vertices (Fig. 1);

(ii) optimum Cu – O interatomic distances in the layer plane (1.90 – 1.97 Å) to provide the overlapping of the $3d_{x^2-y^2}$ copper orbitals and the $2p_{x,y}$ oxygen orbitals with the formation of delocalized states in the σ^* band; and

(iii) an optimum carrier concentration in the (CuO_2) layers that corresponds to the formal copper oxidation state +2.05 to +2.25 for hole-doped superconductors and +1.8 to +1.9 for electron-doped superconductors.

Copper atoms can also be bound to oxygen atoms located in neighboring layers. However, these bonds are significantly longer and exceed 2.2 Å. Copper cations in the structures of superconductors have different chemical bonds with oxygen atoms: strong (planar) bonds in the (CuO_2) layer plane and much weaker (axial) bonds in the normal direction. The structures of the superconductors based on complex copper oxides are layered, and the framework structures of these oxides do not have superconducting properties.

Due to its negative charge, the (CuO_2) layer should be located between positive-charged or neutral cation – anion layers. Obviously, the most convenient layers are (AO) or ($A'\square$) (where $\square$ is an anion vacancy) layers. Figure 2 shows the (CuO_2) layer located between such layers in the two simplest structures, perovskite ABO_3 and $CaCuO_2$ (tetragonal anion-deficient perovskite structure). The structure (i.e., atomic positions and geometric characteristics) of this layer is optimum for the perovskite structure ABO_3, which contains layers of two types, (AO) and (BO_2), alternating along a fourfold axis. Therefore, all superconducting complex copper oxides have structures that are derivative of perovskite or contain a perovskite-like fragment as one of the structural blocks.

A complex oxide with a perovskite structure can be synthesized if the electric neutrality criterion is satisfied and the cation – anion distances correspond to the Goldschmidt

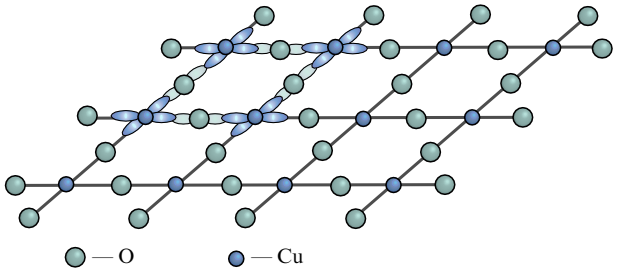

Figure 1. Structure of the copper – oxygen (CuO_2) layer.

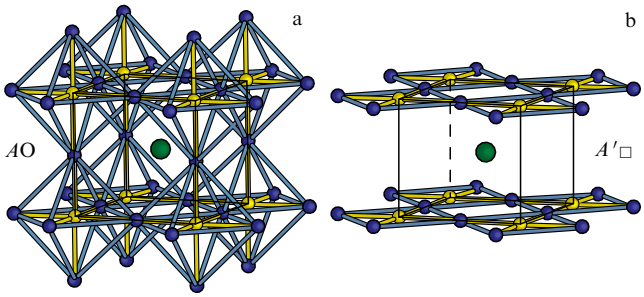

Figure 2. Structures of ABO_3 perovskite (a) and $CaCuO_2$ (b), in which (CuO_2) layers alternates with (AO) or $(A'\square)$ layers.

criterion $d_{A-O} \approx \sqrt{2}d_{B-O}$. When Cu^{2+} is chosen as the B cation, electric neutrality is the main problem. The copper cations in the (CuO_2) layers have the formal oxidation state close to +2; therefore, the formal charge of this layer should be close to −2, and the charge of the (AO) layer should correspondingly be equal to +2. This makes it difficult to choose the A-type cation, since metals with the formal charge +4 have very small radii, coordination numbers, and interatomic distances to oxygen. These contradictions can be resolved by synthesizing compounds with anion-deficient perovskite-like ABO_{3-x} structures ($0 < x \leqslant 1$, e.g., $CaCuO_2$ or $YBa_2Cu_3O_{7-\delta}$) or compounds with intergrowth structures, which represent most well-known superconducting complex copper oxides.

Despite the variety of compositions of superconducting phases with intergrowth structures, they can be described by the general formula $B_mA_2A'_{n-1}Cu_nO_{2n+2+x}$, which can be represented as the sequence of layers

$$(AO)\,(BO_x)_m(AO)\,(CuO_2)\left[(A'\square)(CuO_2)\right]_{n-1} \times (AO)(BO_x)_m(AO)\,,$$

where $0 \leqslant x \leqslant 1$, $m = 0, 1, 2$, $n = 1, 2, 3, \ldots$, A and A' are the respective cations of alkaline-earth or rare-earth metals and B is the smaller cation (e.g., Hg^{2+}, Tl^{3+}, Bi^{3+}). These layers are formally joined to yield blocks of the perovskite, fluorite, or sodium chloride type, since the arrangement of cations and anions in these fragments corresponds to their arrangement in these simplest inorganic structures. For the fluorite block (R_2O_2), the sequence of three $(R)\,O_2(R)$ layers (where R is a tri- or tetravalent rare-earth element) appears instead of the $(A'\square)$ layer. Superconducting (CuO_2) layers are located in perovskite blocks, and their number per unit cell varies from 1 to n (usually, n does not exceed 5–7). If $n \geqslant 2$, oxygen-free $(A'\square)$ layers or a fluorite block at $n = 2$ are placed between these layers. The remaining dielectric blocks ensure structure stability; in particular, they compensate for the negative charge of the (CuO_2) layer. These fragments have a positive formal charge, which can be varied by heterovalent cation (anion) substitution or a change in the oxygen content; as a result, the hole concentration that is optimal for superconductivity can be achieved in the conduction band. Figure 3 shows a schematic diagram for the formation of an intergrowth structure, in which the perovskite block alternates with the NaCl and fluorite blocks.

The lattice parameters of the cubic unit cells of a number of oxides with NaCl- and CaF_2-type structures fall in the range 5.2–5.7 Å. The cation–cation distances in these structures are close to the corresponding distances in perovskite-type structures, in which the parameter a is

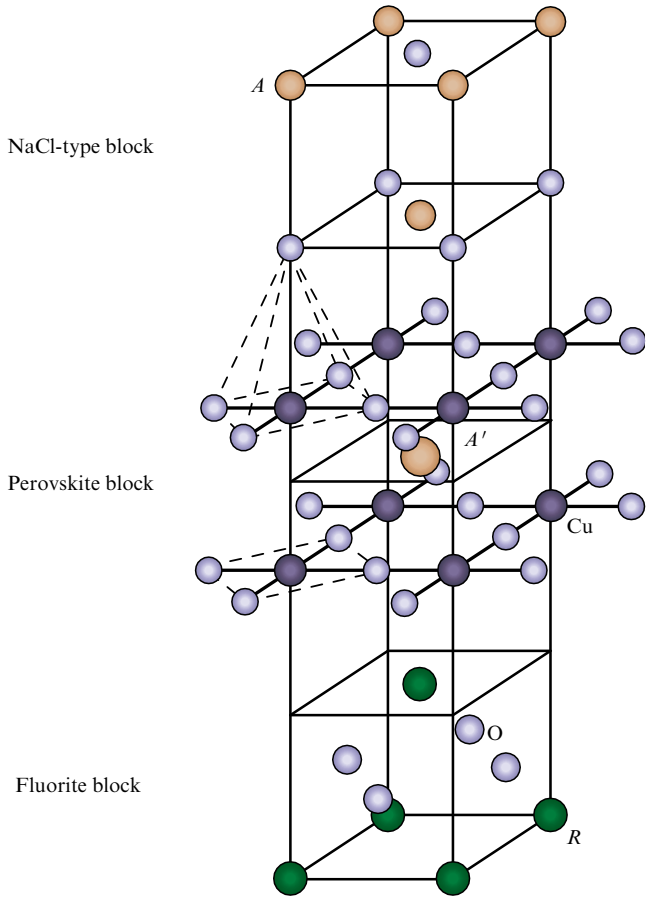

Figure 3. Schematic diagram for the formation of an intergrowth structure with alternating structural blocks of the NaCl, perovskite, and fluorite types.

usually 3.7–4.1 Å ($a_{NaCl} \approx a_{CaF_2} \approx \sqrt{2}a_{per}$). The face-centered cubic unit cells of the NaCl and fluorite types can be transformed into body-centered tetragonal cells with parameters a close to a_{per}. It is important that the cation motifs in the perovskite unit cell and the transformed fluorite and NaCl unit cells be the same and that the oxygen atom positions be different.

The layered character of the structures of all well-known copper HTSCs agrees with Ginzburg's "quasi-two-dimensional model," in which a planar conductor [in our case, copper-containing (CuO_2) layers] touches an insulator [blocks of the fluorite or sodium chloride type or $(AO/(A'\square)$ layers], e.g., a dielectric film. The development of this concept leads to the alternation of thin conducting and dielectric layers as in a 'sandwich' [1].

Structures with such layer sequences are stable only if the interatomic distances in any layer match with those in the upper and lower neighboring layers in the (ab) plane. A mismatch causes strong distortions in the (CuO_2) layers, which results in the degradation of superconducting properties down to the suppression of superconductivity. In the structures of Bi-containing $Bi_2Sr_2Ca_{n-1}Cu_nO_{2n+4+\delta}$ superconductors, the in-plane Cu–O distances fall in the range 1.9–1.95 Å; in this case, the Sr–O and Bi–O interatomic distances should be 2.7–2.75 Å, which is typical of the strontium cation and too large for the bismuth cation. Cooperative atomic displacements in the $(BiO_{1+\delta/2})$ layers eventually lead to the formation of the interatomic distances

and coordination numbers typical of this cation. The sequence of such atomic displacements (incommensurate modulations) becomes possible due to the introduction of an additional oxygen atom (δ) into approximately every fifth cell. Otherwise, the displacements of Bi and O atoms would result in the location of like-charged ions in two successive (BiO) layers immediately above each other. The cooperative displacements and the introduction of an additional oxygen atom restore the matching of alternating layers in Bi – HTSC structures but introduce distortions in these layers, including the (CuO_2) layer. In a strongly distorted $Bi_{2+x}Sr_{2-x}CuO_{6+\delta}$ structure, T_c does not exceed 20 K in spite of the hole concentration in the conduction band that is optimal for superconductors of this type. The superconducting transition temperature increases to 86 and 108 K for the second and third members of the Bi-containing homologous series, which have much smaller distortions in the (CuO_2) layers. However, the possibilities of a further increase in T_c in the family of $Bi_2Sr_2Ca_{n-1}Cu_nO_{2n+4+\delta}$ superconductors due to an increase in the number of (CuO_2) layers in the perovskite block are exhausted, since the amount δ of hyperstoichiometric oxygen bound to bismuth cations by strong bonds cannot vary over a wide range and is similar for all compounds in the family.

Varying the cation composition of the blocks and the formal degree of copper oxidation states (which is accompanied by a change in the Cu – O distances) allows changing the block sizes and producing the required compound via a proper synthesis method. To predict new intergrowth structures, we must take into account the crystal-chemistry specific features of cations (the ionic radius, coordination number, character of the chemical bond with oxygen), the chemical compatibility of ions (the simultaneous absence of strong oxidizers and reducers), and the electric neutrality of the unit cell. The choice of the synthesis method should be dictated by the chemical features of the initial substances and the required degrees of oxidation of individual components in the final structure.

An important crystal-chemistry criterion for a high-T_c superconductor is the absence of strong local distortions in the (CuO_2) layer, which can be induced by a statistical joint location of different cations (e.g., di- and trivalent cations) in the same crystallographic position in neighboring layers. The difference in the crystal-chemistry properties of these cations leads to the formation of different coordination polyhedra with oxygen atoms, including oxygen atoms bound to copper atoms, which causes local distortions in the (CuO_2) layer. As these distortions increase, T_c decreases to the complete suppression of superconductivity.

Figure 4 shows the electron-density distribution of the oxygen atom in the axial position with respect to the copper cation from the (CuO_2) layer in the structure of $Nd_{1.7}Ba_{1.3}Cu_3O_{7.15}$ [2]. The electron density is seen to shift from the fourfold axis, which is caused by the joint location of barium and neodymium cations at the same crystallographic position. As a result of this shift, the Ba and Nd cations acquire their intrinsic coordination environments, which is accompanied by the appearance of various Cu – O axial bonds and strains in the (CuO_2) layer.

We note that the standard structural examination by neutron or X-ray diffraction can hardly reveal such distortions, since the refinement of atomic parameters only results in the enhanced thermal parameters of atoms, which reflect not a dynamic but a static character of displacements. To adequately describe the atomic arrangement, we have to use precise data on perfect single crystals, obtaining which involves significant experimental difficulties. Attfield et al. [3] proposed using the disorder parameter σ^2 that characterizes

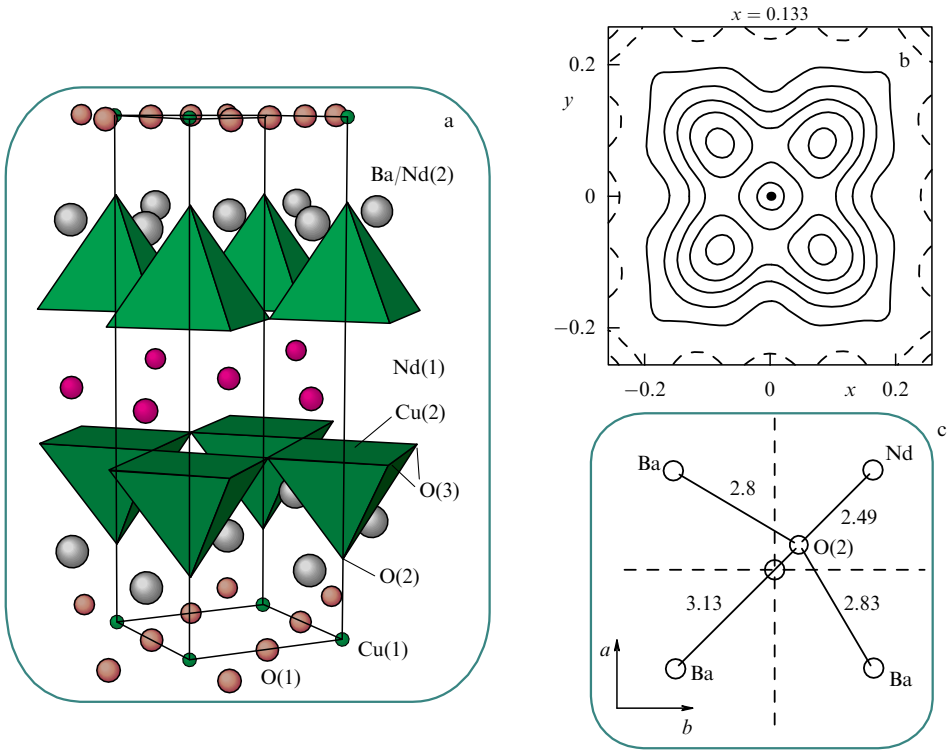

Figure 4. (a) Crystal structure of $Nd_{1.7}Ba_{1.3}Cu_3O_{7.15}$, (b) electron density map of the oxygen atom O(2), and (c) Nd – O(2) and Ba – O(2) interatomic distances.

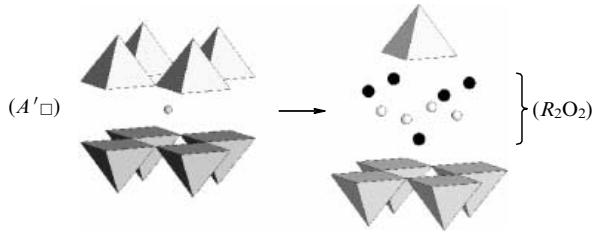

Figure 5. Schematic diagram of the substitution of the fluorite block (R_2O_2) for the $(A'\square)$ layer in the structures of layered copper oxides.

the difference in the sizes of the cations statistically located at the same position, in order to estimate the linear decrease in T_c as this parameter increases.

This reason is thought to be the main factor that results in the low values of T_c or the absence of superconductivity in all intergrowth structures that contain fluorite fragments and tetravalent cations (Ce or Th) apart from trivalent rare-earth cations. Intergrowth structures with a fluorite block can be formally described as the result of a 'substitution' of the fluorite block (R_2O_2) for an $(A'\square)$ layer located between two (CuO_2) layers in a prototype structure. This substitution results from the closeness of the fluorite and perovskite block sizes in the (*ab*) plane and from the charge balance (Fig. 5). Table 1 gives the maximum values of T_c for various fluorite-block-containing superconductors and their prototype structures. The superconducting transition temperatures of the fluorite-block-containing compounds are well below those of the prototype structures. This can be due to the statistical distribution of different cations in the layers next to (CuO_2) layers, which induces a structural disorder and local distortions in these layers.

Table 1. T_c of complex copper oxides with fluorite blocks and the prototype structures.

'Fluorite' phase	T_c	Prototype structure	T_c
$La_{0.9}Sm_{0.9}Sr_{0.2}CuO_{3.97}$	27 K [4]	$La_{1.6}Sr_{0.4}CaCu_2O_6$	60 K [5]
$Pb_2Sr_2Eu_{1.33}Ce_{0.67}Cu_3O_{10}$	24 K [6]	$Pb_2Sr_2Y_{0.6}Ca_{0.4}Cu_3O_8$	70 K [7]
$Bi_2Sr_2Eu_{1.7}Ce_{0.3}Cu_2O_{10+\delta}$	28 K [8]	$Bi_2Sr_2CaCu_2O_{8+\delta}$	86 K [9]
$Eu_2Ba_{1.33}Ce_{0.67}Cu_3O_{8+\delta}$	40 K [10]	$YBa_2Cu_3O_{7-\delta}$	93 K [11]

3. Mercury-containing superconducting complex copper oxides $HgBa_2Ca_n$

The structures of most Cu-containing superconductors have a fragment consisting of three alternating layers, $(CuO_2)(AO)(BO)$ (Fig. 3, NaCl-type block). Structures with such layer sequences are stable only when the interatomic distances in any layer match those in the upper and lower neighboring layers, and the correspondence between the (CuO_2) and (AO) layers is most important. From the standpoint of a geometrical criterion, Ba^{2+}, Sr^{2+}, and La^{3+} are optimum cations for position *A*. The use of alkaline-earth metal cations of proper sizes in this position along with other structural fragments cannot compensate for the excess negative charge of the (CuO_2) layer in oxide structures. For T_c to be high in complex copper oxides, the cation positions in the layers next to (CuO_2) should be occupied by cations of the same type. Otherwise, the difference in the crystal-chemistry properties of the cations placed at the same position causes local distortions in the structure, which decreases T_c and eventually suppresses superconductivity [3].

Since the crystal-chemistry properties of *A*-type cations strongly affect the structure of the (CuO_2) layer and, correspondingly, the conducting properties of compounds, we assumed that compounds with the cations of divalent mercury in the *B*-type position could have the optimum structure. In oxide phases, these cations are characterized by a dumbbell coordination, which is realized, e.g., in $MHgO_2$ (M = Ca, Sr, Ba) structures. For such a coordination to form near Hg^{2+} cations, the structure of a layered oxide should have oxygen atoms only in neighboring layers, and their presence in the layer with the mercury cations is not necessary. The absence of steric difficulties and the weak chemical bond with neighboring cations allow changing the occupation of the anion position with oxygen atoms and varying the hole concentration in the conduction band. We also note that Hg^{2+} cations have the optimum formal charge for achieving the electric neutrality of the structure. In these structures, there should be no mismatch of the (AO), (HgO_δ), and (CuO_2) layers because the Hg–O bond in the (HgO_δ) layer should be too weak to substantially affect the matching with other structural fragments and the superconducting properties of layered copper oxides with this structural block.

Cystal-chemistry has allowed predicting a new family of superconductors $HgBa_2Ca_{n-1}Cu_nO_{2n+2+\delta}$. In Section 4, we briefly discuss their crystal structures and superconducting properties. Detailed information is given in review [12].

4. Crystal structures of $HgBa_2Ca_{n-1}Cu_nO_{2n+2+\delta}$

The structures of the first three members of the family are shown in Fig. 6. The structures of $HgBa_2Ca_{n-1}Cu_nO_{2n+2+\delta}$ can be schematically represented as the following sequence of layers alternating along the unit-cell *c* axis:

$$(HgO_\delta)(BaO)(CuO_2)\{(Ca)(CuO_2)\}_{n-1}(BaO)(HgO_\delta)\,.$$

All compounds have tetragonal primitive cells with similar parameters *a*, and the parameter *c* increases with the perovskite fragment thickness in accordance with the formula $c \approx 9.5 + 3.2 \times (n-1)$[Å].

The structures of $HgBa_2Ca_{n-1}Cu_nO_{2n+2+\delta}$ are very close to the corresponding structures of the compounds of the homologous series $TlBa_2Ca_{n-1}Cu_nO_{2n+2+\delta}$. The main difference is in the number of oxygen atoms in layers with Hg or Tl

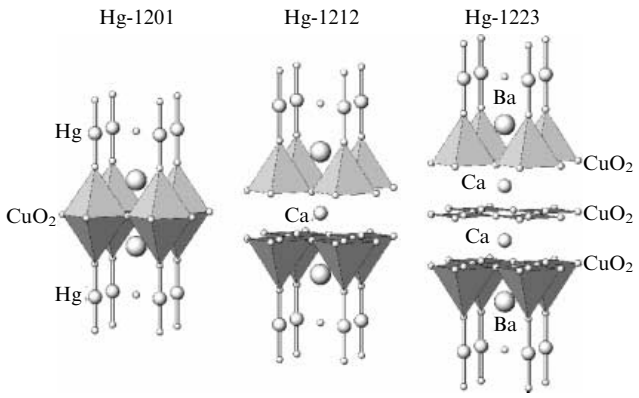

Figure 6. Crystal structures of $HgBa_2Ca_{n-1}Cu_nO_{2n+2+\delta}$ with $n = 1$, 2, and 3.

atoms. In the structures of the Tl-containing superconductors, the filling of the oxygen position δ insignificantly differs from unity irrespective of the number of (CuO_2) layers in the structures, since these oxygen atoms are required for the creation of the characteristic coordination of Tl^{3+} ions. In contrast, in the structures of $HgBa_2Ca_{n-1}Cu_nO_{2n+2+\delta}$, the content of weakly bound overstoichiometric oxygen in the Hg^{2+}-containing layer can vary within very wide limits by heat treatment at various temperatures and partial oxygen pressures. Overstoichiometric oxygen strongly affects the copper oxidation state in (CuO_2) layers and the superconducting transition temperature. For members of the homologous series $HgBa_2Ca_{n-1}Cu_nO_{2n+2+\delta}$, the formal copper oxidation state can be calculated by the formula $V_{Cu} = 2(n+\delta)/n$.

In the structures of this family, the NaCl-type block has the same structure in all compounds and consists of the three alternating layers (BaO), (HgO_δ), and (BaO). On the whole, δ increases with an increase in n; however, the δ ranges of various homologues can overlap. For example, the values of δ obtained by neutron diffraction are 0.06 – 0.23 for Hg-1201 [13, 14] and 0.08 – 0.35 for Hg-1212 [15 – 17]. The Hg^{2+} cations have a specific dumbbell surrounding of the nearest oxygen atoms from (BaO) layers with $d(\mathrm{Hg-O}) \approx 1.95$ Å. Overstoichiometric oxygen atoms from the (HgO_δ) layer are far from mercury atoms ($d(\mathrm{Hg-O}) \approx 2.7-2.76$ Å) and are not involved in the formation of a strong chemical bond with these cations.

As the perovskite-fragment thickness increases, the coordination of the copper atoms in (CuO_2) layers changes from an octahedral coordination in the structure of $HgBa_2CuO_{4+\delta}$ to a tetragonal – pyramidal coordination in $HgBa_2CaCu_2O_{6+\delta}$ and then to a square or tetragonal – pyramidal coordination in $HgBa_2Ca_2Cu_3O_{8+\delta}$ and the structures of the higher homologues. The octahedra and tetragonal pyramids are strongly elongated along the c-axis because of the Jahn – Teller distortion. Table 2 gives the Cu – O and Ba – O distances in the structures with $n = 1-3$.

The specific feature of the structure of Hg-containing superconductors is a very long Cu – O distance to the axial oxygen atom in the copper polyhedra, which vary in the range 2.75 – 2.8 Å for various members of the series; as a result, the interaction between these atoms is very weak. This distance is much longer than the corresponding distances in the structures of other copper-containing superconductors. For example, the Cu – O distance in $YBa_2Cu_3O_7$ ($T_c = 92$ K) is 2.32 Å. Another peculiar feature is the absence of significant atomic displacements in layers due to the absence of mismatch. Introduced oxygen atoms do not cause a superstructure or orthorhombic distortions, since they are located at the center of a square formed by mercury atoms. Therefore, the structure of the (CuO_2) layers in Hg-containing superconductors is closest to the ideal structure, as compared to the structures of the well-known superconducting complex copper oxides. The (CuO_2) layers in Hg-1212 and Hg-1223 are almost planar despite the asymmetric tetragonal – pyramidal copper coordination. This ideal structure is likely to be the main cause of superconductivity in these compounds at temperatures that are maximal among the temperatures of all well-known superconductors.

In $HgBa_2Ca_{n-1}Cu_nO_{2n+2+\delta}$, the in-plane Cu – O distances decrease with increasing δ (due to the oxidation of copper atoms) or with increasing the perovskite-fragment thickness. In the latter case, it is interesting to analyze the relation between the changes in the various interatomic distances when moving to structures with a large number of (CuO_2) layers. For the same of copper oxidation state to be achieved in these structures, the amount of hyperstoichiometric oxygen introduced into the Hg-containing layer should increase as n increases. As a result, the fraction of barium atoms that move toward an additional anion increases, which is accompanied by a decrease in the $Ba-O_{Hg}$ distances and an increase in the $Ba–O_{Cu}$ distances between Ba^{2+} cations and oxygen atoms from the (CuO_2) layer (Fig. 7, Table 2). Thus, the interaction between Ba atoms and these oxygen atoms weakens, which is compensated by a decrease in the in-plane Cu – O distance. Therefore, the sequential increase in

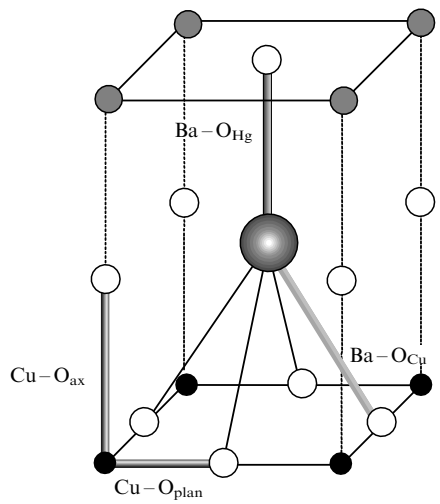

Figure 7. Some interatomic distances in $HgBa_2Ca_{n-1}Cu_nO_{2n+2+\delta}$.

Table 2. Some interatomic distances [Å] in $HgBa_2Ca_{n-1}Cu_nO_{2n+2+\delta}$ ($n = 1-3$).

Compound	δ	$Cu-O_{plan}$	$Cu-O_{ax}$	$Ba-O_{Hg}$	$Ba-O_{Cu}$
Hg-1201	0.06	1.9432	2.803	2.866	2.726
	0.12	1.9426	2.787	2.841	2.733
	0.19	1.9398	2.771	2.834	2.734
	0.23	1.9365	2.750	2.787	2.751
Hg-1212	0.08	1.9320	2.824	2.848	2.733
	0.22	1.9290	2.799	2.807	2.758
	0.28	1.9272	2.798	2.773	2.773
	0.35	1.9263	2.787	2.749	2.778
Hg-1223*	0.41	1.9252	2.751	2.55, 2.94	2.92, 2.63

* Data for two positions of Ba atoms.

the perovskite-fragment thickness in the structures of $HgBa_2Ca_{n-1}Cu_nO_{2n+2+\delta}$ induced by the introduction of an additional $CaCuO_2$ block compresses the in-plane interatomic distances in structures of the higher homologues and can be represented as an anisotropic 'chemical' compression. The in-plane Cu – O interaction strongly affects the critical superconducting transition temperature (see Section 5).

The sequential increase in the perovskite-fragment thickness does not cause substantial changes in the structures of the highest homologues. It is difficult to study the structures of these compounds because of impurities and high stacking-fault concentrations. As n increases, the concentration of these defects, in which the sequences of layers correspond to other members of the family, increases [18].

5. Superconducting properties of $HgBa_2Ca_{n-1}Cu_nO_{2n+2+\delta}$

The superconducting transition temperature of the $HgBa_2Ca_{n-1}Cu_nO_{2n+2+\delta}$ phases depends strongly on two parameters, the oxygen content δ and the number n of (CuO_2) layers in their structures. It is interesting that the dependences of these temperatures have a dome-like shape in both cases [19 – 21].

Figure 8 shows the dependence of T_c on n. The values of T_c correspond to the maximum values obtained for each superconductor. The superconducting transition temperature is seen to increase from the first member of the homologous series (97 K) to the second (127 K) and third (135 K) member, and then to decrease for the fourth (127 K), fifth (110 K, and sixth (107 K) members of this series. One of the possible causes of the decrease in T_c in the higher homologues can be the distortion of the outer (CuO_2) layers with increasing n because of a decrease in the $Cu-O_{ax}$ distance. The enhancement of the interaction between these atoms shifts copper atoms from the plane toward the axial oxygen, which leads to a distortion of the O – Cu – O bond angle and a loss of planarity of these (CuO_2) layers.

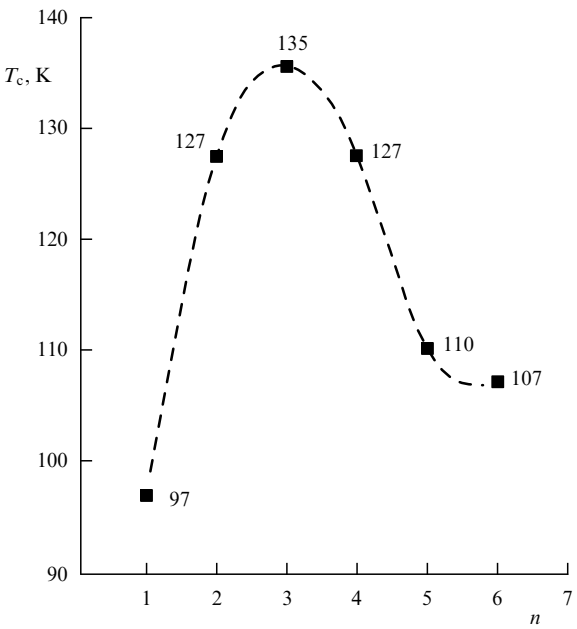

Figure 8. T_c vs. the number n of (CuO_2) layers for the compound $HgBa_2Ca_{n-1}Cu_nO_{2n+2+\delta}$.

Generally, the superconducting transition temperature of a complex superconducting copper oxide depends on the hole concentration in the conduction band (or on the formal degree of copper oxidation). The optimum degree of oxidation for hole-doped superconductors ranges from +2.10 to +2.20, where the compounds typically exhibit maximum values of T_c. Outside this range, T_c decreases. Thus, the dependence of the superconducting transition temperature on the formal copper oxidation state should have a dome-like character. This rule holds in the case of only one type of oxidized elements [i.e., copper atoms in the (CuO_2) layer] in the structure of a superconductor.

If there are several types of copper atoms or another oxidizable element, this dependence is much more complex, since charges can be redistributed between different structural fragments. T_c is also strongly affected by the factors that determine the structure of the (CuO_2) layers.

It was shown above that the structures of the $HgBa_2Ca_{n-1}Cu_nO_{2n+2+\delta}$ compounds are optimal for the appearance of superconductivity, since they have no distortions induced by a mismatch of interatomic distances and a nonuniform cation distribution in neighboring layers. Moreover, the structures of the first members of the homologous series ($HgBa_2CuO_{4+\delta}$ and $HgBa_2CaCu_2O_{6+\delta}$) only have one type of copper atom. Therefore, the dependence of T_c on the formal degree of copper oxidation, which is changed by varying δ, should have a dome-like character for these compounds, which is supported experimentally. Superconductivity in $HgBa_2CuO_{4+\delta}$ can be suppressed as the index δ strongly increases. The nonsuperconducting overoxidized compound Hg-1201 was synthesized at a high pressure. For this compound, $V_{Cu} = +2.28$ corresponds to the V_{Cu} range outside which superconductivity is suppressed [14]; such ranges were established previously for other superconducting copper oxides.

For members of the homologous series with $n \geqslant 2$, it is difficult to use iodometric titration to determine V_{Cu} because of the presence of impurity phases. The Cu – O distance in the (CuO_2) layer depends on the formal copper oxidation state, which is changed by varying δ. Since this layer is planar, the unit-cell parameter a of the Hg-containing superconductors is approximately twice the Cu – O distance. Therefore, a change in the parameter a after various heat treatments indicates the character of the change in δ. Figure 9 shows the $T_c(a)$ dependences for five members of the family that also have a dome-like character. It is interesting that the maximum values of T_c increase in the Hg-1201 – Hg-1212 – Hg-1223 series as the parameter a [hence, the $Cu-O_{plan}$ distance (see Table 2)] decreases. The cause of this increase was discussed in Section 4. Thus, the sequential increase in the perovskite-fragment thickness in this series of compounds can be formally considered a structural modification that causes anisotropic compression of the in-plane interatomic distances, which can lead to an increase in T_c.

Chu et al. [22] were the first to detect a substantial increase in T_c in $HgBa_2Ca_2Cu_3O_{8+\delta}$ at ultrahigh pressures. The superconducting transition temperature of this compound increases sharply with the applied pressure and reaches 164 K at the pressure about 31 GPa [23, 24]. The pressure-induced increase in the superconducting transition temperature in Cu-containing superconductors, which exhibit hole conductivity in the normal state, is a well-known phenomenon. Nevertheless, the specific feature of the experiments performed on Hg-1223 and other compounds of this family lies in achieving

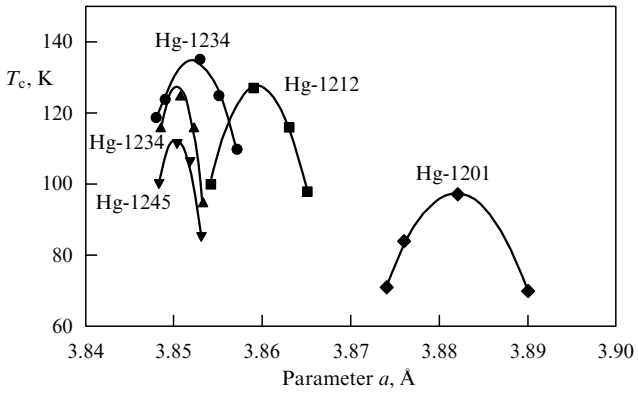

Figure 9. T_c vs. parameter a for $HgBa_2Ca_{n-1}Cu_nO_{2n+2+\delta}$ compounds.

record values of T_c, which are well above those reached previously. These results demonstrate that superconductivity with $T_c = 150-160$ K can exist at atmospheric pressure in structures where the Cu – O distances are identical to those realized in $HgBa_2Ca_{n-1}Cu_nO_{2n+2+\delta}$ at an applied pressure.

Using neutron diffraction under pressure, the authors of [25 – 29] revealed the main trends in the variation of the interatomic distances in these superconductors. As the pressure increases, the Hg – O bond length remains virtually the same because of the strongly covalent character of this bond. The compression of the structures along the c-axis is caused by a significant decrease in the axial Cu – O distance. An isotropic applied pressure also decreases the in-plane Cu – O distance, but to a lesser extent.

Interesting conjectures can be made regarding the different characters of the dependences of the superconducting transition temperature on the applied isotropic pressure and the anisotropic chemical compression of the in-plane Cu – O distances, which is induced by an increase in the perovskite-fragment thickness in the Hg-1201 – Hg-1212 – Hg-1223 series. In this series, the axial Cu – O distances are virtually unchanged (see Table 2), which suggests the strongest effect of the in-plane distance on T_c. The value of $dT_c/d(Cu-O_{plan})$ calculated from the structural data for these compounds with the maximum values of T_c exceeds -1000 K Å^{-1} for this series. However, for isotropic applied pressure, this value is substantially lower (~ -160 K Å^{-1}).

6. Fluoro-substituted derivatives of superconducting mercury-containing cuprates

Important conclusions concerning the doping mechanism and the effect of the in-plane and axial Cu – O distances on T_c in mercury cuprates can be drawn by comparing the characteristics (the anion content, the formal copper oxidation state, the structural parameters, the superconducting transition temperature) of samples in which the optimum level of doping was achieved by the introduction of additional oxygen or fluorine. Oxygen and fluorine are similar from the crystal-chemistry standpoint and have high electric negativity, and their anions have similar ionic radii ($r_{F^-} = 1.29$ Å and $r_{O^{2-}} = 1.35$ Å for coordination number 2). Moreover, many oxide compounds exhibit structural analogues between fluorides and oxofluorides (CaO and NaF, LaOF and CaF_2, La_2CuO_4 and K_2CuF_4, etc.). Therefore, when fluorine is introduced into complex layered copper oxides, related oxofluorides can form. The formal charges of O^{2-} and F^- are different, and, according to a simple ionic model of hole formation in a conducting (CuO_2) layer, the amount of fluorine anions required for a certain doping level is twice that of oxygen anions.

The fluorination of the Hg-1201 phase $HgBa_2CuO_{4.01}$ with $T_c = 61$ K by xenon difluoride XeF_2 leads to an increase in the superconducting transition temperature to the maximal value for this compound ($T_c = 97$ K), the subsequent decrease in T_c, and, eventually, the suppression of superconductivity, presumably because of too high a copper oxidation state (overoxidation) [30]. According to neutron powder diffraction data, the anion content in the Hg-containing layer is $\delta = 0.24(2)$ for an optimally doped sample with $T_c = 97$ K and $\delta = 0.32(2)$ for an overoxidized sample with $T_c = 80$ K. These values are well above the occupations found for oxidized Hg-1201 samples with close values of T_c ($\delta = 0.124(9)$ and $0.19(1)$, respectively) [13]. The dependences of T_c on the fluorine or oxygen content in the Hg-containing layer have a domelike shape; however, the curve for the fluorinated samples shifts toward higher values of δ (Fig. 10a). We can conclude that, like oxygen, fluorine oxidizes copper cations in (CuO_2) layers and that the amount of fluorine required for achieving certain values of T_c and a certain degree of doping is twice that of oxygen, which agrees with the difference in the formal charges O^{2-} and F^-. This finding supports the ionic model of doping in mercury cuprates: the number of holes created by one oxygen atom is twice that induced by one fluorine atom.

For both the fluorinated and oxidized samples, the dependences of T_c on the unit-cell parameter a (or, equivalently, on the $Cu-O_{plan}$ interatomic distance in the (CuO_2) layer plane) can be approximated by one parabolic curve with a maximum ($T_c = 97$ K) at $a = 3.882$ Å (Fig. 10b). Thus, the same superconducting transition temperatures can be achieved not only at the same level of doping but also at similar lengths of the in-plane Cu – O bonds; that is, both parameters control T_c in complex cuprates.

For a certain copper oxidation state, the $Cu-O_{plan}$ distance is virtually independent of the amount of overstoichiometric anions. In contrast, the $Cu-O_{ax}$ distance changes significantly as the degree of filling the anion position in an Hg-containing layer is varied. The dependence of this distance on δ (for oxygen or fluorine) is almost linear (Fig. 10c). An increase in the amount of hyperstoichiometric anions results in compression of the $Cu-O_{ax}$ bond, whose length in the fluorinated compounds is substantially smaller than that in the oxygen-containing compounds having similar values of T_c.

The cause of the decrease in the $Cu-O_{ax}$ distance consists in the extension of the Hg – O dumbbells induced by the increase in the coordination number of mercury atoms due to additional anions in the Hg-containing layer. As a result, an oxygen atom O_{ax} shifts from Hg to a Cu atom, which is accompanied by a noticeable decrease in the $Cu-O_{ax}$ distance, while the $Cu-O_{plan}$ distance and T_c remain virtually unchanged. This change in the interatomic distances can be considered a result of the anisotropic compression of the CuO_6 octahedra, which is equivalent to the effect of a pressure of about 2 GPa applied along the c-axis [29]. For the optimally oxygen-doped Hg-1201 phase, $dT_c/dP \approx 2$ K GPa^{-1} [31]; therefore, in a fluorinated sample with $\delta_F \approx \delta_{opt}$, the superconducting transition temperature should increase by ≈ 4 K. The absence of a difference in the values of T_c for the samples optimally doped by fluorine or oxygen indicates that the compression of the $Cu-O_{ax}$ bond

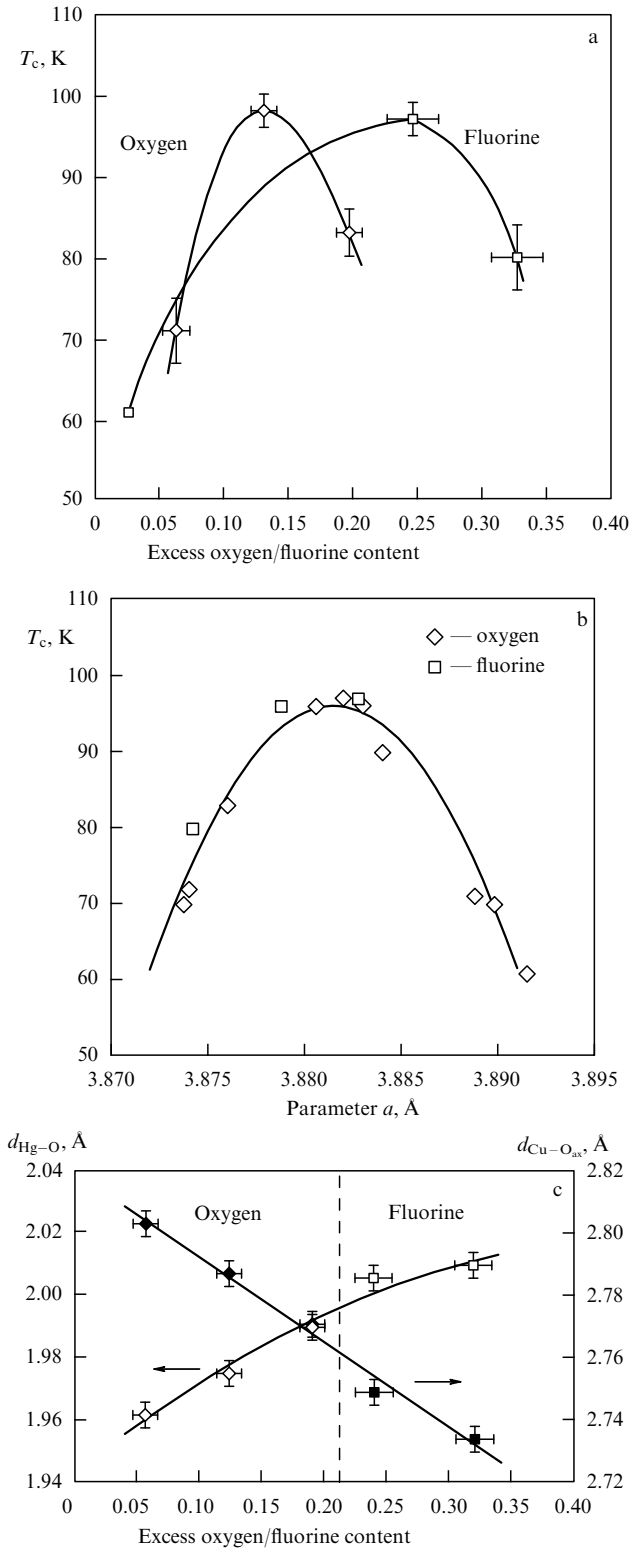

Figure 10. (a) Dependence of T_c on the excess oxygen or fluorine content for the Hg-1201 phase. (b) Dependence of T_c on unit-cell parameter a for Hg-1201 samples with various oxygen and fluorine contents. (c) Dependences of the $Cu-O_{ax}$ and $Hg-O$ interatomic distances on the amount of oxygen or fluorine atoms in the mercury layer.

only weakly affects the increase in T_c in Hg-containing cuprates at an applied pressure and that the most probable cause of this phenomenon lies in a decrease in the $Cu-O_{plan}$ distances.

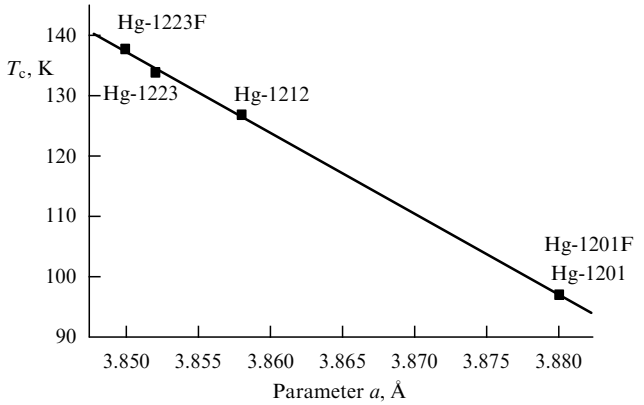

Figure 11. Maximum values of T_c vs. the unit-cell parameter a for oxidized and fluorinated Hg-containing cuprates.

This conclusion is also confirmed by the results of studying fluorinated $HgBa_2Ca_2Cu_3O_{8+\delta}$ (Hg-1223) samples. The initial Hg-1223 sample with $T_c = 100$ K exhibits an increase in T_c upon both fluorination and oxidation; however, T_c of the fluorinated sample is 4 K higher (138 K) than that of the oxidized sample (134 K) [32, 33]. It is interesting that this fluorinated sample has the highest T_c ($T_c = 166$ K at the pressure 23 GPa) among all superconductors [34]. The maximum values of T_c for the first three members of the homologous series of mercury-containing complex $HgBa_2Ca_{n-1}Cu_nO_{2n+2+\delta}$ cuprates and fluorinated Hg-1201 and Hg-1223 samples depend on the parameter a linearly, and we have $dT_c/da \approx -1350$ K Å^{-1} (Fig. 11) [33, 35]. We can state that T_c of these compounds depends on the compression of the (CuO_2) planes induced by the modification of the chemical composition. A similar value of dT_c/da was also detected upon the epitaxial compression of thin $La_{0.9}Sr_{0.1}CuO_4$ single-crystal films [36]. The value of dT_c/da observed upon the fluorination of Hg-1223 is almost an order of magnitude higher than the value induced by applied pressure ($dT_c/dP \approx 1.7$ K GPa$^{-1} \equiv dT_c/da \approx -160$ K Å^{-1}). This difference can result from a structural distortion of the (CuO_2) layers. In Hg-1201, these layers are planar by their symmetry, and, in Hg-1212, the $Cu-O_{plan}-Cu$ angle is close to 180° [17]. For Hg-1223, fluorination exerts a weak effect on the $Cu-O_{plan}-Cu$ angle: it is 178.4° for an oxidized sample [28] and 177.3° for a fluorinated sample [33]. A high applied pressure leads to folded (CuO_2) layers; for example, in Hg-1223, the $Cu-O_{plan}-Cu$ angle decreases to 175.0° at the pressure 2 GPa, which increases T_c to 138 K. The deviation of this valence angle from 180° is also an important parameter affecting T_c; for cuprates with $T_c > 100$ K, this deviation does not exceed 4°.

7. Fluoro-substituted derivatives of other families of superconducting cuprates

The specific feature of the structure of Hg-containing cuprates is that the Hg-containing layer has an anion position that can be partly occupied by oxygen or fluorine atoms, which results in various hole concentrations in the conduction band. A stable dumbbell-like coordination of the Hg^{2+} cations causes the absence of steric difficulties and a weak interaction between anions and mercury cations in this layer. Owing to the formation of a long and weak $Hg-(O, F)$ bond in the layer plane, the introduction of anions into this layer does not lead to significant structural changes. How-

ever, the appearance of overstoichiometric anions in the structure of complex cuprates due to the introduction of fluorine or the substitution of two F^- anions for one O^{2-} anion can lead to structural transformations, which include changes in the coordination polyhedra, the interatomic distances, and the space symmetry up to complete rearrangement of the crystal structure. These transformations can be expected if fluorine anions form strong covalent or ionic bonds with neighboring cations. The fluorination of complex cuprates can be used for both producing new compounds with a structure required for the manifestation of superconducting properties and achieving the required carrier (electron or hole) concentration in the conduction band. The character of the change in the crystal structure is determined by the structure of the initial compound and the excess-anion content [37]:

(i) The replacement of oxygen atoms by the equivalent amount of fluorine atoms only causes insignificant changes in the unit-cell metric, which are related to the small difference in the ionic radii O^{2-} and F^- and to an increase in the in-plane Cu – O bond length due to the decreasing copper oxidation state.

(ii) The introduction of excess fluorine atoms and the completion of the coordination polyhedron of Cu^{2+} cations to an octahedron lead to a sharp increase in the axial Cu – O bond length, which is accompanied by an increase in the distances between the $(Cu(O, F)_2)$ and (AO) layers.

(iii) The occupation of vacant anion positions by fluorine atoms suppresses the structural distortions induced by the ordering of oxygen atoms and anion vacancies.

(iv) The location of fluorine atoms in interlayer voids results in a structure transformation of the crystal structure in order to decrease the forces of electrostatic repulsion between interlayer anions and anions in neighboring layers.

The perovskite-like anion-deficient structure of the $R\mathrm{Ba_2Cu_3O_{6+\delta}}$ (R-123) phases is represented by the idealized sequence of layers

$$-\mathrm{Cu}\square\mathrm{O}_\delta-\mathrm{BaO}-\mathrm{CuO_2}-R\square-\mathrm{CuO_2}-\mathrm{BaO}-\mathrm{Cu}\square\mathrm{O}_\delta-$$

(where $\square$ stand for anion vacancies). The anion positions in the $(\mathrm{Cu}\square\mathrm{O}_\delta)$ layer (Cu1 layer) can be fully vacant at $\delta = 0$, which corresponds to the structure of the tetragonal strongly reduced R-123 phase (which is not a superconductor, $V_{\mathrm{Cu}} = +1.67$). The Cu1 atoms are in the dumbbell coordination characteristic of the Cu^{1+} cations (Fig. 12a). At $\delta \approx 1$, oxygen atoms occupy half the vacant positions in the Cu1 layer in an ordered manner, completing the coordination environment to a square (Fig. 12b). Chains of the CuO_4 squares connected by common vertices are oriented along the b-axis, which results in an orthorhombic distortion of the structure. Compounds with $\delta \approx 1$ have a hole concentration that is near-optimal for this structure and exhibit the highest superconducting transition temperature ($T_c = 93-94$ K) among the compounds of this class.

In 1987, Kistenmacher used simple crystal-chemistry considerations and predicted the presence of complex oxofluoride $YBa_2Cu_3O_6F_2$ in which anion vacancies in the (Cu1) layer are fully occupied by fluorine atoms. The copper oxidation stare in this compound is $V_{\mathrm{Cu}} = +2.33$, which corresponds to the formula $YBa_2Cu_3O_7$ (oxygen-doped Y-123). This oxofluoride should have a tetragonal symmetry due to the substitution of two-dimensional (CuF_2) layers for copper – oxygen chains and could exhibit super-

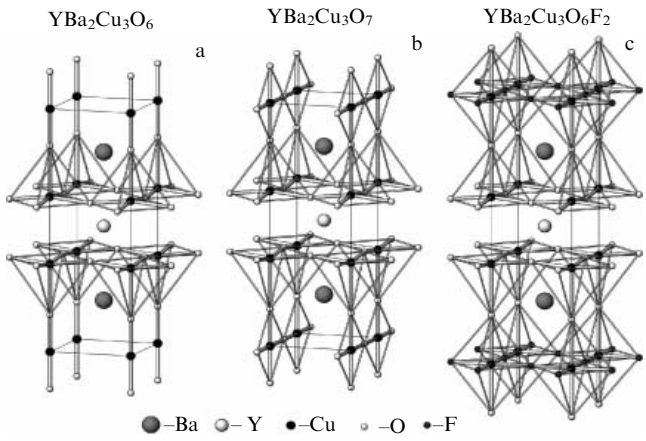

Figure 12. Crystal structures of $YBa_2Cu_3O_6$ (a), $YBa_2Cu_3O_7$ (b), and $YBa_2Cu_3O_6F_2$ (c).

conducting properties [38]. The introduction of fluorine atoms into the structure of the reduced nonsuperconducting compound $YBa_2Cu_3O_{6.11}$ occurs in the vacant anion positions of the (Cu1) layer and is accompanied by the formation of distorted CuO_2F_4 octahedra [39, 40]. According to the proposed structural model, this is accompanied by an increase in the axial Cu – O distance from 1.85 Å in $YBa_2Cu_3O_{6.11}$ to 2.3 – 2.5 Å in the fluorinated compound with the idealized composition $YBa_2Cu_3O_6F_2$ (Fig. 12c). The fluorination of the reduced nonsuperconducting compound $YBa_2Cu_3O_{6.11}$ leads to an increase in the copper oxidation state to $V_{\mathrm{Cu}} = +2.14$ and the appearance of superconductivity at the temperature 94 K with a large superconducting-phase volume ($\approx 25\%$).

One of the simplest copper oxofluorides with superconducting properties could be made from hypothetic perovskite-like $(\mathrm{La, Sr})\mathrm{CuO_2F}$ solid solutions in which the required degree of copper oxidation is achieved via heterovalent substitution in the A sublattice. Such perovskites can be synthesized by fluorination of anion-deficient perovskites, such as $(\mathrm{La}_{1-x}\mathrm{Sr}_x)_8\mathrm{Cu}_8\mathrm{O}_{20-\delta}$ solid solutions, which have the framework structure of an anion-deficient perovskite without (CuO_2) planes and copper atoms with square, tetragonal – pyramidal, and octahedral environments (Fig. 13a). For a compound to be superconducting, fluorination should change the character of the oxygen distribution in the initial structure such that (CuO_2) planes form. When the compound $La_{6.5}Sr_{1.5}Cu_8O_{19.65}$ is fluorinated by xenon difluoride, the perovskite-like $\mathrm{La_{0.813}Sr_{0.187}Cu(O, F)_{3-\delta}}$ phase forms with a tetragonally distorted unit cell with the parameters $a \approx c \approx a_{\mathrm{per}}$ and $c > a$ (Fig. 13b) [41]. The anion positions in the equatorial environment of copper atoms are fully occupied and vacancies concentrate in the axial positions. The Jahn – Teller effect, which occurs because some copper atoms have an octahedral coordination, leads to an increase in the axial distances (2.026 Å) compared to the in-plane distances (1.896 Å) and a tetragonal distortion of the perovskite cell with $c > a$. The oxofluoride $\mathrm{La_{0.813}Sr_{0.187}Cu(O, F)_{3-\delta}}$ is not a superconductor, which can be related to overoxidation, local distortions in (CuO_2) layers, and the possibility of partial substitution of fluorine for oxygen in the (CuO_2) layers (which transform them into $(Cu(O,F)_2$ layers). We believe that the use of other synthesis methods can result in successful synthesis of the oxofluoride $La_{0.85}Sr_{0.15}CuO_2F$ with an ordered oxygen and fluorine

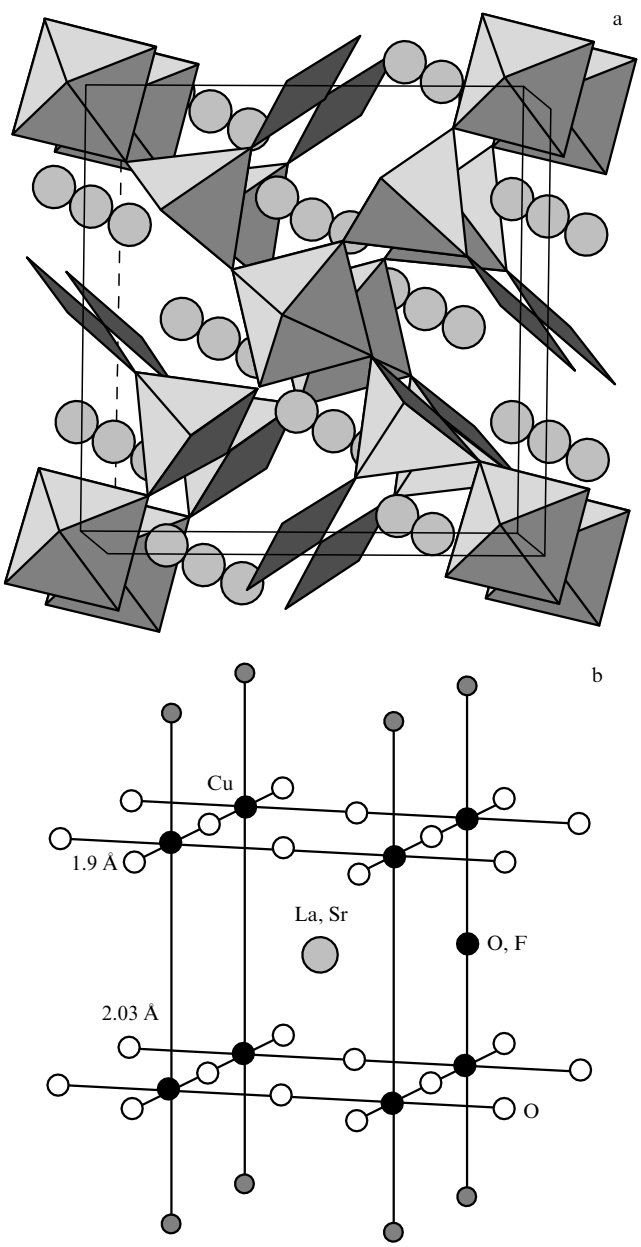

Figure 13. Schematic diagram of the structural transformation of $La_{6.5}Sr_{1.5}Cu_8O_{19.65}$ (a) into $La_{0.813}Sr_{0.187}Cu(O,F)_{3-\delta}$ (b) upon fluorination.

arrangement in the structure with alternating (CuO_2) and ($La_{0.85}Sr_{0.15}F$) layers. Such a compound could be an example of the simplest structure of superconducting cuprates.

For cuprates containing sodium chloride – type blocks, the ionic character of the $A-O$ bond leads to the fact that the strengths of the bonds in the $((R, A)O)$ layers are comparable to those of the bonds between neighboring $((R, A)O)$ layers. The structure of the Bi-containing layered cuprates $Bi_2Sr_2Ca_{n-1}Cu_nO_{2n+4+\delta}$ also contains (Bi_2O_2) blocks with a sodium chloride structure. In contrast to $((R, A)_2O_2)$ blocks with isotropic chemical bonds, only a weak van der Waals interaction is realized between layers in the (Bi_2O_2) block, which is related to the crystal-chemistry properties of the Bi^{3+} cation. The Bi – F bond is substantially ionic, which should result in a change in the structure of the (Bi_2O_2) layers with interstitial fluorine atoms.

The fluorination of the Bi-2201 $Bi_2Sr_{1.6}La_{0.4}CuO_{6.33}$ phase by XeF_2 causes the disappearance of incommensurate modulations (Fig. 14a), which indicates that interstitial fluorine changes the structure of the (Bi_2O_2) blocks [42]. Excess anions are placed in the interstices of the (Bi_2O_2) block, which are tetrahedrally coordinated by Bi atoms such that the (Bi_2O_2) block transforms into a ($Bi_2O_{2-x}F_{2+x}$) block in which Bi atoms are located in a single-cap square antiprism with four short Bi – F bonds and five long Bi – O bonds (Figs 14b – 14d). Blocks with an analogous structure are encountered in representatives of the Aurivillius-phase homologous series, e.g., in Bi_2NbO_5F [43]. In the Bi-2201 phase, the (BiO) layers are almost flat and the distance between the Bi and O layers along the c-axis in these layers does not exceed 0.24 – 0.26 Å; but in the Aurivillius phase, this distance increases to 0.92 – 1.07 Å, leading to the 'splitting' of the (BiO) layer into two layers (one of which

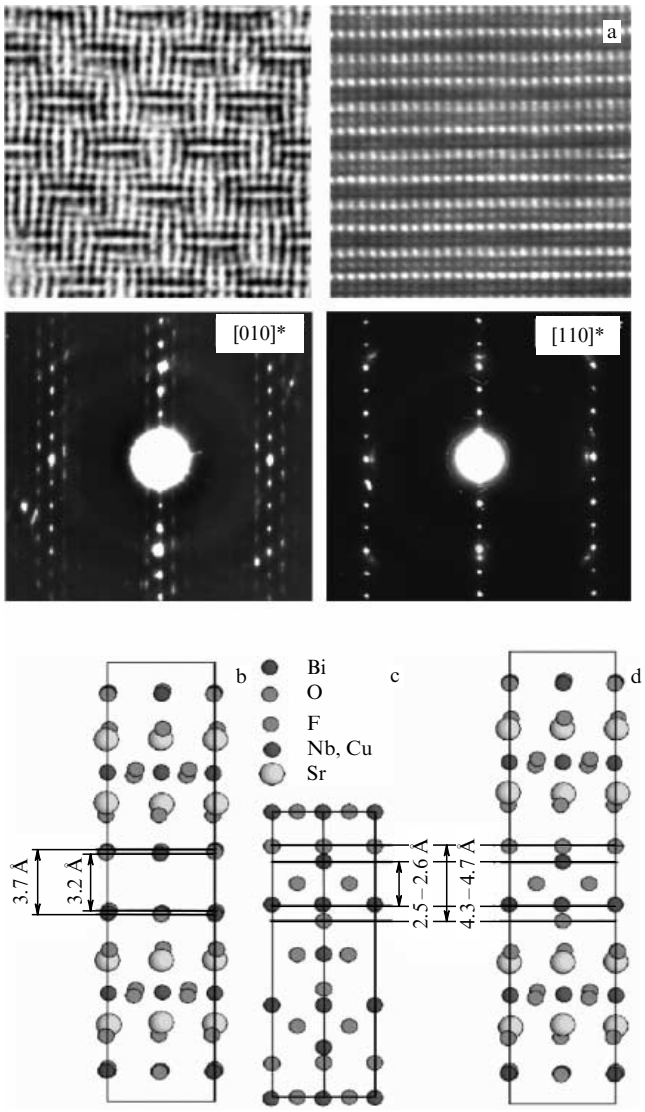

Figure 14. (a) High-resolution transmission electron microscopy images and electron diffraction patterns of the initial and fluorinated Bi-2201 phases, which indicate the disappearance of incommensurate modulations upon fluorination. The crystal structures of $Bi_2Sr_{1.6}La_{0.4}CuO_{6.33}$ (b) and Bi_2NbO_5F (c). (d) A model for the structure of the fluorinated tetragonal Bi-2201 phase.

consists of Bi atoms and the other of O atoms). An increase in the coordination number of bismuth in the fluorinated phase increases the Bi – O distances and the block size in the *ab* plane. As a result, the match is achieved between the ($Bi_2O_2F_2$) blocks and (CuO_2) layers, which leads to the suppression of incommensurate modulations. We note that the fluorinated Bi – 2201 phase has a hybrid structure in which Bi-containing ($Bi_2O_{2-x}F_{2+x}$) blocks (as in the Aurivillius phases) and perovskite $A_2Ca_{n-1}Cu_nO_{2n+2}$ ($n = 1$) blocks are matched; that is, such phases belong to the new family of cuprates $Bi_2A_2Ca_{n-1}Cu_n(O,F)_{2n+6}$, whose representatives can have superconducting properties.

8. Conclusions

In the last two decades of extensive studies of the superconducting properties of complex copper oxides, the possibilities of creating a new class of superconducting cuprates or further optimizing the properties of well-known compounds have been nearly exhausted. Nevertheless, it is too early to state that compounds with T_c higher than in the obtained values cannot exist among the complex cuprates. The increase in T_c in Hg-containing cuprates induced by an applied pressure or fluorination suggests that the chemical modification that causes a decrease in the in-plane $Cu - O_{plan}$ distance without changing the degree of folding the (CuO_2) layers is a promising way for increasing T_c in complex superconducting copper oxides. A simple isovalent cation substitution, which leads to isotropic compression of the structure, is likely to be ineffective. For example, a partial substitution of Sr for Ba atoms decreases T_c, since it is accompanied by a strong decrease in the axial Cu – O bond and the 'folding' of the (CuO_2) layer. A more promising way is thought to consist in the production of metastable layered structures using nontraditional chemical synthesis methods, such as the synthesis of epitaxial films using layer-by-layer deposition onto substrates with chosen lattice parameters, which can create anisotropic compression of the structure of a superconductor in the (*ab*) plane and artificial heterostructures exhibiting an analogous effect.

In this report, we demonstrated that the modification of the anion sublattice upon substituting halogen atoms (e.g., fluorine) for oxygen can modify the structure of complex cuprates to yield new compounds that can be potential high-temperature superconductors. Indeed, as can be seen from Table 3, complex copper oxofluorides often exhibit a T_c comparable to or higher than that of their oxygen analogues. An analogous example can be found among oxochlorides. The compound $(Sr,Ca)_3Cu_2O_{4+\delta}Cl_{2-y}$ has $T_c = 80$ K [44], which is well above the superconducting transition temperature of its oxygen analogue $La_{1.6}Sr_{0.4}CaCu_2O_{6+\delta}$ ($T_c = 60$ K). We note that the synthesis of such compounds requires the application and development of labor-intensive methods in order to produce a compound in its metastable state.

Table 3. Superconducting complex copper oxofluorides.

Oxofluoride	T_c, K	Oxygen analogue	T_c, K
$YBa_2Cu_3O_6F_2$	94	$YBa_2Cu_3O_{6.95}$	92
$Y_2Ba_4Cu_7O_{14}F_2$	62	$Y_2Ba_4Cu_7O_{14.92}$	80
$HgBa_2CuO_4F_{0.24}$	97	$HgBa_2CuO_{4.12}$	97
$HgBa_2CaCu_2O_6F_\delta$	128	$HgBa_2CaCu_2O_{6.22}$	127
$HgBa_2Ca_2Cu_3O_8F_\delta$	138	$HgBa_2Ca_2Cu_3O_{8+\delta}$	134
$Sr_2CuO_2F_{2+\delta}$	46	Sr_2CuO_3	—
$La_2CuO_4F_\delta$, $\delta \leqslant 0.18$	35 – 40	$La_2CuO_{4.032}$	38
$Nd_2CuO_{3.7}F_{0.3}$	27	$Nd_{2-x}Ce_xCuO_4$	24
$Sr_2CaCu_2O_{4.6}F_2$	99		
$Sr_2Ca_2Cu_3O_{6.2}F_{3.2}$	111		
$Sr_2Nd_{0.2}Ca_{0.8}Cu_2O_5F$	85		

References

1. Ginzburg V L *Phys. Lett.* **13** 101 (1964); *Zh. Eksp. Teor. Fiz.* **47** 2318 (1964); [*Sov. Phys. JETP* **20** 1549 (1965)]; *Usp. Fiz. Nauk* **174** 1240 (2004) [*Phys. Usp.* **47** 1155 (2004)]
2. Fomichev D V, D'yachenko O G, Mironov A V, Antipov E V *Physica C* **225** 25 (1994)
3. Attfield J P, Kharlanov A L, McAllister J A *Nature* **394** 157 (1998)
4. Kopnin E M et al. *Sverkhprovodimost'* **5** 530 (1992)
5. Cava R J et al. *Nature* **345** 602 (1990)
6. Kharlanov A L et al. *Physica C* **169** 469 (1990)
7. Cava R J et al. *Nature* **336** 211 (1988)
8. Khasanova N R et al. *Physica C* **190** 522 (1992)
9. Maeda H et al. *Jpn. J. Appl. Phys.* **27** L209 (1988)
10. Sawa H et al. *J. Phys. Soc. Jpn.* **58** 2252 (1989)
11. Wu M K et al. *Phys. Rev. Lett.* **58** 908 (1987)
12. Antipov E V, Abakumov A M, Putilin S N *Supercond. Sci. Technol.* **15** R31 (2002)
13. Aksenov V L et al. *Phys. Rev. B* **55** 3966 (1997)
14. Loureiro S M et al. *Physica C* **243** 1 (1995)
15. Radaelli P G et al. *Physica C* **216** 29 (1993)
16. Loureiro S M et al. *Physica C* **217** 253 (1993)
17. Antipov E V et al. *Physica C* **218** 348 (1993)
18. Van Tendeloo G et al. *Physica C* **223** 219 (1994)
19. Fukuoka A et al. *Phys. Rev. B* **55** 6612 (1997)
20. Zhang Q, Chen X *Physica C* **282 – 287** 905 (1997)
21. Scott B A et al. *Physica C* **230** 239 (1994)
22. Chu C W et al. *Nature* **365** 323 (1993)
23. Gao L et al. *Phys. Rev. B* **50** 4260 (1994)
24. Nuñez-Regueiro M et al. *Science* **262** 97 (1993)
25. Balagurov A M et al. *Phys. Rev. B* **59** 7209 (1999)
26. Hunter B A et al. *Physica C* **221** 1 (1994)
27. Aksenov V L et al. *High Pressure Res.* **14** 127 (1995)
28. Armstrong A R et al. *Phys. Rev. B* **52** 15551 (1995)
29. Aksenov V L et al. *Physica C* **275** 87 (1997)
30. Abakumov A M et al. *Phys. Rev. Lett.* **80** 385 (1998)
31. Cao Y et al. *Phys. Rev. B* **52** 6854 (1995)
32. Putilin S N et al. *Physica C* **338** 52 (2000)
33. Lokshin K A *Phys. Rev. B* **63** 064511 (2001)
34. Monteverde M et al. *Europhys. Lett.* **72** 458 (2005)
35. Wagner J L et al. *Phys. Rev. B* **51** 15407 (1995)
36. Locquet J-P et al. *Nature* **394** 453 (1998)
37. Abakumov A M, Rozova M G, Ardashnikova E I, Antipov E V *Usp. Khim.* **71** 442 (2002) [*Russ. Chem. Rev.* **71** 383 (2002)]
38. Kistenmacher T J *Phys. Rev. B* **36** 7197 (1987)
39. Shpanchenko R V et al. *Physica C* **280** 272 (1997)
40. Van Tendeloo G, Lebedev O I, Shpanchenko R V, Antipov E V *J. Electron Microsc.* **46** 23 (1997)
41. Abakumov A M et al. *J. Solid State Chem.* **149** 189 (2000)
42. Hadermann J et al. *J. Solid State Chem.* **156** 445 (2001)
43. Aurivillius B *Ark. Kemi* **4** 39 (1952)
44. Jin C-Q et al. *Nature* **375** 301 (1995)

PACS numbers: 74.20.Mn, **74.72.–h**
DOI: 10.1070/PU2008v051n02ABEH006468
DOI: 10.3367/UFNr.0178.200802i.0202

With cuprate luggage to room-temperature superconductivity

Yu V Kopaev, V I Belyavsky, V V Kapaev

1. Problems and progress in the physics of cuprates

The high-temperature superconductivity (HTSC) of cuprates was discovered in 1986 [1], when the highest superconducting transition temperature characteristic of conventional superconductors ($T_c = 23.2$ K in Nb_3Ge) was substantially exceeded and a superconducting (SC) transition temperature $T_c \approx 30$ K was achieved in the ceramic $La_{2-x}Ba_xCuO_{4+\delta}$. Within a year after this discovery, the record value of T_c exceeded 90 K ($YBa_2Cu_3O_{6+\delta}$ ceramic). The further search for and creation of new SC materials led to $T_c = 138$ K (Tl-doped $HgBa_2Ca_2Cu_3O_{8+\delta}$ compound) in 1994 and raised the question of room-temperature superconductivity.

Studies over the last two decades have not brought researchers to agreement concerning the superconductivity mechanism in cuprate compounds and have not resulted in a theory similar to the Bardeen–Cooper–Schrieffer (BCS) theory of conventional superconductors [2]. Nevertheless, we must acknowledge significant progress in understanding the nature of cuprate superconductivity that has been achieved in these years.

The key structural element of layered quasi-two-dimensional (2D) cuprates is a (CuO_2) plane (one or several in a unit cell); they differ from conventional superconductors not only in high values of T_c but also in a set of physical properties that cannot be described by the BCS scheme. In cuprates, charge carriers appear due to the doping of the CuO_2 planes of a parent antiferromagnetic (AF) insulator upon nonisovalent atomic substitution or the creation of oxygen vacancies in charge reservoirs outside the conducting planes. The distance between equivalent CuO_2 planes in neighboring unit cells is large compared to the in-plane distance between neighboring copper atoms, which results in a strong conductivity anisotropy at temperatures above T_c and the 2D coherence of the SC state at temperatures below T_c.

In the absence of an external magnetic field, the thermodynamic state of a doped cuprate compound can be described by the temperature T and the carrier concentration in the CuO_2 plane (doping level) x. In the phase diagram (Fig. 1), the SC state field corresponds to a certain doping range $x_* < x < x^*$ inside which the SC transition temperature reaches its maximum value at the optimum doping x_{opt}. Concentrations $x \lesssim x_{opt}$ correspond to underdoped cuprates, and concentrations $x \gtrsim x_{opt}$ to overdoped cuprates.

At $x \gtrsim x_{opt}$ and $T > T_c$, cuprates are 'bad' Fermi liquids, and at $x \lesssim x_{opt}$, over a wide temperature range $T_c < T < T^*$, they exhibit the pseudogap state, whose nature is still unknown [3]. The gap spectrum of quasiparticles at $T > T_c$ demonstrates that the SC phase appears from a certain insulating state rather than from a Fermi liquid, such that the ground states of an insulator and a superconductor, with similar structures and energies, converge near the SC transition line. This behavior corresponds to the concept of strong correlations in cuprates, which result in the competing singlet states of a d-wave superconductor and a flux insulating phase [4].

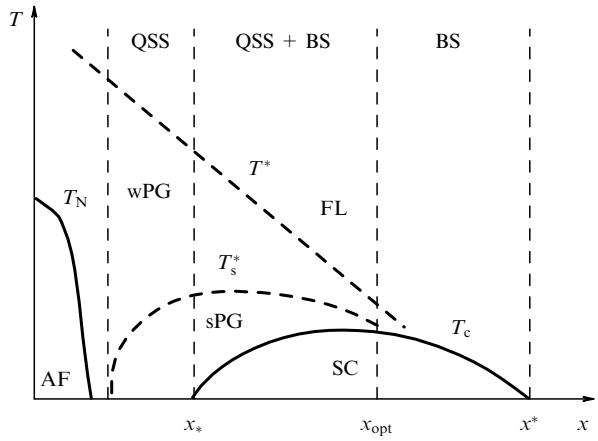

Figure 1. Typical phase diagram of hole-doped cuprates. The Néel (T_N) and SC transition (T_c) temperatures respectively bound the long-range AF and SC order regions. Strong pseudogap (sPG) and weak pseudogap (wPG) regions are separated by a crossover temperature T_s^*. The temperature T^* separates the weak pseudogap from the normal Fermi liquid (FL). The regions in which the bound states (BSs) and quasi-stationary states (QSSs) of K pairs appear are shown, and the region of coexisting BS and QSS is also depicted.

The pseudogap state is divided into a strong pseudogap that is adjacent to T_c and exists over a wide temperature range $T_c < T \lesssim T_s^*$, and a weak pseudogap between T_s^* and T^*. The strong pseudogap has a high nonlinear diamagnetic response [5, 6] and a giant Nernst effect [7] and can be related to a fluctuating SC order in the form of noncoherent long-lived quasi-stationary states of SC pairs [8]. T_s^* corresponds to the breaking of a pair, and T_c corresponds to the appearance of phase coherence in the system of pairs. A consistent theory of cuprate superconductivity should be able to explain both the high values of T_c and the physical properties of these compounds in a large neighborhood of the SC state that includes the strong and weak pseudogaps in the phase diagram.

Strong electron correlations and the unusual symmetry of the pseudogap and the SC order parameter in cuprates are arguments for a purely electron superconductivity mechanism (rather than a phonon mechanism, as in the BCS theory). The studies of this mechanism for strong intracenter Coulomb repulsion in terms of the Hubbard model and the related $t-J$ model are described in a number of reviews [9]. The 2D Hubbard problem has not been exactly solved, and approximate solutions obtained by numerical methods are often in conflict, which leads to reasonable doubts about the usefulness of this approach [10], especially because the unusual isotopic effect in cuprates [11–13] indicates a nontrivial role of phonons in pairing-interaction formation.

For pairing repulsion, the singlet SC order parameter $\Delta(\mathbf{k})$ is a scalar function of the momentum $\mathbf{k}$, and this function should be alternating in its domain after the separation of the phase factor corresponding to the center-of-mass motion of the pair. An analysis of experiments sensitive to the momentum dependence of the order parameter [14, 15] demonstrates that $\Delta(\mathbf{k})$ vanishes at several points in the Fermi contour (FC) that can correspond to an extended s or s + g symmetry ($\Delta(\mathbf{k})$ does not change its sign under rotation through the angle $\pi/2$) or a d symmetry (four zeros as a result of the change in the sign of $\Delta(\mathbf{k})$ upon rotation through the angle $\pi/2$).

Order-parameter zeros open a channel for scattering by nonmagnetic impurities, which is ineffective for the s symmetry and corresponds to the BCS phonon mechanism. This should break the SC state, whose resistance to scattering by nonmagnetic impurities is one of the key tests for a cuprate superconductivity theory.

This theory should explain a number of specific features of cuprates that distinguish them from conventional superconductors. For example, the optical-conductivity measurements in [16] demonstrate that upon SC condensation, the spectral weight is redistributed over a wide energy range $\gtrsim 100\Delta$ rather than in an energy range $\sim \Delta$, as follows from the BCS theory (the high-energy problem [17]). Moreover, the real part of the optical conductivity exhibits the Drude behavior $\sigma_1 \sim \omega^{-2}$ for $T < T_c$; that is, the particle density in the SC condensate is comparable to the density of off-condensate particles. The same conclusion follows from the temperature dependence of the heat capacity [18], which corresponds to a gap-free spectrum of elementary excitations at $T < T_c$, $c_V \sim T$. The key problems of the physics of cuprates also involve the origin and role of the self-organization of an electron system in the form of stripes [19] or the staggered spatial ordering of the system at $T < T_c$ (in the form of an SC-pair density wave [20]).

Although modern approaches to the problem of cuprate superconductivity are often based on different physical concepts (such as the traditional phonon mechanism [21], the resonating valence bond (RVB) scheme [22, 23], the SU(2) charge – spin separation scheme [4], the concept of high-momentum SC pairing [8], the theory of an algebraic Fermi liquid [24], the concept of a quantum critical point [25], and the SO(5) phenomenology [26] or the SU(4) phenomenology [27]), their consequences have many common features [28]. The usefulness of a certain approach is determined by its ability to explain the properties of HTSC compounds and to suggest ways to increase their critical parameters [17].

2. Superconducting pairing with a high momentum

The concept of SC pairing with a high momentum for a screened Coulomb repulsion [8] qualitatively corresponds to experimental data. In contrast to the models adjusted to describe low-energy excitations, it is based on a standard Hamiltonian that involves screening, the effect of the electron – phonon interaction, and the universality of the FC intrinsic in cuprates.

The shape of the FC of doped cuprates that agrees with the angle-resolved photoemission spectroscopy (ARPES) data in [29, 30] is described by the dispersion law

$$\varepsilon(\mathbf{k}) = -2t(\cos k_x + \cos k_y) + 2t' \cos k_x \cos k_y + t''(\cos 2k_x + \cos 2k_y)\,. \qquad (1)$$

Here, the integrals of hopping between the nearest Cu atoms along the diagonal (t') and between the next-to-nearest Cu atoms in the direction of the Cu – O bond (t'') account for the fundamental asymmetry of the excitation spectrum (electron – hole asymmetry), which manifests itself, for example, in tunneling spectra [31].

The FC in Fig. 2 corresponds to the case where $t'/t \approx -0.3$ and $t''/t \approx 0.2$; these ratios correspond to the conditions that are optimal for superconductivity [4]. At a zero pair momentum, a logarithmic singularity occurs in the SC-pairing channel for any dispersion law, because $\varepsilon(\mathbf{k}) = \varepsilon(-\mathbf{k})$; therefore, the sensitivity of the SC state to the dispersion-law parameters indicates the specific features of the pairing kinetics in cuprates.

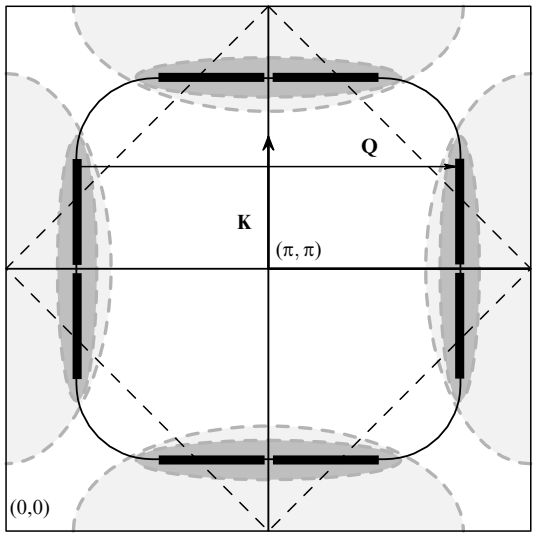

Figure 2. Fermi contour characteristic of underdoped cuprates (thin line). Heavy segments represent the parts of the FC in which mirror nesting occurs for pairs with the total momentum **K** and nesting occurs for pairs with the total momentum **Q**. Bright semiovals indicate the regions of the extended neighborhoods of saddle points, and dark semiovals correspond to the insulating pairing upon **K** pairing. The dashed line indicates the boundary of the magnetic Brillouin zone.

The almost rectilinear FC segments in an extended neighborhood of the saddle point symmetrically split with respect to the points $0, \pm\pi$ and $\pm\pi, 0$ (see Fig. 2) and lead to *nesting* $\varepsilon(\mathbf{k}+\mathbf{Q}) = -\varepsilon(\mathbf{k})$ for a certain incommensurate momentum $\mathbf{Q}$ that is not equal to the momentum (π, π) of the spin AF structure of the parent compound, and to a logarithmic singularity in the static generalized susceptibility $\chi(\mathbf{q})$ at $\mathbf{q} = \mathbf{Q}$, allowing instabilities in the insulating pairing channels. Apart from a spin density wave (SDW) with the AF vector $\mathbf{Q}$, a charge density wave (CDW), a charge current density wave (CCDW), and a spin current density wave (SCDW) can also appear. The insulating gap $\Delta_i(\mathbf{k})$ appears in a certain part of the FC, and dispersion law (1) transforms into the law

$$\varepsilon(\mathbf{k}) = \varepsilon_{1,2}(\mathbf{k}) = \varepsilon_+(\mathbf{k}, \mathbf{Q}) \pm \sqrt{\varepsilon_-^2(\mathbf{k}, \mathbf{Q}) + \Delta_i^2(\mathbf{k})}\,, \qquad (2)$$

where $\varepsilon_\pm(\mathbf{k}, \mathbf{Q}) = \varepsilon(\mathbf{k}) \pm \varepsilon(\mathbf{k}+\mathbf{Q})$.

In the final portion (pair Fermi contour), the universal FC of cuprates satisfies the *mirror nesting* condition $\varepsilon(\mathbf{k}_+) = \varepsilon(\mathbf{k}_-)$ for a pair of particles (**K** pair) with momenta $\mathbf{k}_\pm = \mathbf{K}/2 \pm \mathbf{k}$ at a certain total momentum **K** (**k** is the momentum of the relative motion of the pair). This results in a logarithmic singularity in the SC pairing channel with the momentum **K** and the appearance of the following nontrivial solution of the self-consistency equation:

$$\Delta(\mathbf{k}) = -\frac{1}{2} \sum_{\mathbf{k}'} \frac{U(\mathbf{k}, \mathbf{k}')\, \Delta(\mathbf{k}')}{\sqrt{\xi^2(\mathbf{k}') + \Delta^2(\mathbf{k}')}}\,. \qquad (3)$$

For pairing repulsion, the interaction energy is $U(\mathbf{k}, \mathbf{k}') > 0$ at any momenta $\mathbf{k}$ and $\mathbf{k}'$ before and after scattering, respectively. The nontrivial solution $\Delta(\mathbf{k})$ forms in the vicinity of the pair Fermi contour (PFC), in which the kinetic energy of a **K** pair $2\xi(\mathbf{k}) = \varepsilon(\mathbf{k}_+) + \varepsilon(\mathbf{k}_-)$ becomes zero or

almost zero owing to the competition of scattering inside regions of the same sign of $\Delta(\mathbf{k})$ and between these regions. As a result, we have to reverse the sign of the sum in Eqn (3). The coefficient of the logarithm in Eqn (3) is determined by the difference of the integrals over the momentum space regions where $\Delta(\mathbf{k})$ has different signs. In the absence of an electron–hole asymmetry, the pairing in the case of repulsion turns out to be substantially suppressed, whereas in the case of pairing attraction, the mirror nesting of the FC is sufficient for the appearance of an SC state in the weak-coupling limit. For the mirror nesting of the FC, the sufficient condition for the existence of a nontrivial solution of the self-consistency equation with pairing repulsion is the presence of at least one negative eigenvalue of the linear operator with the kernel $U(\mathbf{k}, \mathbf{k}')$.

For SC pairing with a nonzero pair momentum ($\mathbf{K}$ pairing), a *kinematic restriction* is imposed on the region of the momentum space where the particle momenta $\mathbf{k}_+$ and $\mathbf{k}_-$ can lie. The fact that the arguments $\mathbf{k}$ and $\mathbf{k}'$ of the pairing interaction kernel belong to the kinematically restricted region with a characteristic energy scale ε_0 means the elimination of the contributions of many scattering processes, especially those with large momentum transfers $\mathbf{k}' - \mathbf{k} \equiv \boldsymbol{\kappa}$, to the formation of the SC order parameter.

At small momentum transfers, the number of corresponding transitions inside the regions of the same sign of $\Delta(\mathbf{k})$ is approximately proportional to the areas of these regions, and the number of transitions changing the sign of the right-hand side of Eqn (3) is proportional to the area of a strip of the width $\varkappa$ and the length equal to the zero line length. Therefore, scattering with small momentum transfers strongly suppresses the amplitude of the solution of Eqn (3).

Particle scattering in an SC channel competes with phonon scattering, which is characterized by predominant transitions with relatively small momentum transfers. Phonon scattering decreases the contribution of scattering at small momentum transfers to the SC pairing interaction, which mainly occurs inside the momentum space region where $\Delta(\mathbf{k})$ has the same sign. This decrease in the scattering at small momentum transfers with repulsion favors an increase in T_c by weakening the effect of the thermal-excitation-induced breaking of pairs. The contribution of phonons to the pairing interaction due to the suppression of small momentum transfers under scattering is effective at energies lower than the characteristic phonon energy ω_D and disappears at higher energies. This behavior can cause a kink in the photoemission spectrum [32].

Nesting is accompanied by a scattering limitation at large momentum transfers, which is associated with the appearance of an insulating gap in almost rectilinear FC segments and the related redistribution of the spectral weight between the intersecting branches of the elementary-excitation spectrum [33]. When hole doping shifts the chemical potential toward the region below the lower edge of the insulating gap $2\Delta_i$, the spectral weight of the hole part (which is present in a small neighborhood of the lower-subband top) of the SC branch of the excitation spectrum decreases rapidly and passes from the SC branch to the insulating branch of the spectrum. This results in a suppression of the electron and hole momentum transfers that are significantly higher than $\mathbf{Q}$ during scattering. This *insulating limitation* of momentum transfer leads to an SC state with a small spectral weight.

A deviation from the mirror nesting can be taken into account by replacing almost rectilinear FC segments with straight-line segments at a given average deviation (on the energy scale δ) from the FC, i.e., by cutting off the logarithm from below: $\delta \leqslant \xi \leqslant \varepsilon_0$. The order parameter takes the form

$$\Delta(\mathbf{k}) = \operatorname{sgn} \Delta'(\mathbf{k}) \sqrt{\Delta'(\mathbf{k}) \left[\Delta'(\mathbf{k}) - \delta \operatorname{sgn} \Delta'(\mathbf{k})\right]}\,, \tag{4}$$

where $\Delta'(\mathbf{k})$ is the solution of Eqn (3) at $\delta = 0$. The solution exists if $\delta < |\Delta'|$. As δ decreases, the order-parameter amplitude Δ formally increases, which is accompanied by a decrease in the PFC length and, hence, the amplitude Δ'. Thus, the amplitude Δ as a function of δ reaches its maximum, which corresponds to a certain pair momentum $\mathbf{K}$.

The singularity of the susceptibility $\chi(\mathbf{q})$ at $\mathbf{q} = \mathbf{Q}$ leads to the occurrence of a soft mode in the boson-excitation spectrum and the effective electron–electron interaction

$$V(\mathbf{q}) \approx \gamma^2\, \chi(\mathbf{q})\,, \tag{5}$$

where γ has the meaning of a coupling constant that characterizes the interaction of electrons with the corresponding boson excitations. If $\chi(\mathbf{q})$ is the magnetic susceptibility, Eqn (5) describes the spin-fluctuation electron–electron interaction [34] for the appearance of an SDW with a momentum $\mathbf{Q}$. The singularity in the insulating susceptibility $\chi(\mathbf{q})$ corresponds to the Peierls instability [35]. During the nesting of the FC, the CCDW and SCDW related to the charge and spin current degrees of freedom lead to a singularity in the corresponding susceptibilities at $\mathbf{q} = \mathbf{Q}$ and to the electron–electron interaction of type (5). The coupling of a wave with an incommensurate period $2\pi/Q$ to the crystal lattice forms a commensurate structure with a similar period.

3. Superconducting order parameter

The restrictions on scattering at small and large momentum transfers can be taken into account by cutting off the screened pairing Coulomb interaction from below and from above: $q_l \leqslant \varkappa \leqslant q_r$. The numerical solution of Eqn (3) with such a model potential [36] demonstrates that the softening of the small momentum transfer limitation weakly affects the topological properties of the order parameter. For chosen dispersion law parameters, the amplitude Δ decreases sharply at a certain value of q_l, when the degree of the electron–hole asymmetry becomes insufficient to overcome the deviation of the FC from mirror nesting at a chosen coupling constant.

There exist two classes of solutions, which differ in symmetry with respect to a change in the sign of the projection of the relative motion momentum onto the nesting vector $\mathbf{Q}$ (i.e., symmetric and antisymmetric solutions). An antisymmetric solution with one node at the center of the kinematic limitation region corresponds to the maximum order-parameter amplitude. A symmetric solution with two nodes in the kinematic limitation region has a significantly lower amplitude. The antisymmetric solution with the next order-parameter amplitude has three nodes. A gradual decrease in the order-parameter amplitude corresponds to the alternation of the antisymmetric and symmetric solutions with a sequential increase in the number of nodes by unity. This resembles the node distribution of the wave function of a particle in a potential well in accordance with the oscillation theorem [37]; it should be noted that a node-free solution is absent in the case of repulsion. The degree of division of the kinematic limitation region depends on the pair momentum $\mathbf{K}$, which specifies the shape and size of this

region. As the kinematic limitation region extends along the axis normal to the nesting vector **Q**, the number of regions in which $\Delta(\mathbf{k})$ has a constant sign increases, the region size decreases, the order parameter is distributed between these regions, and its amplitude decreases. The amplitude Δ, which depends exponentially on the coupling constant and the kinematic limitation region parameters, is very sensitive to the choice of the dispersion law parameters and the level of doping.

At $K = 0$, an antisymmetric solution cannot be realized for singlet pairing, because it corresponds to the orbital p symmetry of the order parameter. A symmetric solution with two nodes and a significantly lower amplitude compared to the amplitude of the main solution leads to an order parameter with an extended s or d symmetry.

For the **K** pairing, an antisymmetric solution with the maximum order-parameter amplitude can be realized for each crystallographically equivalent pair momentum $\mathbf{K}_j$. The order parameter is small inside the intersection of different kinematic limitation regions and can be determined over the entire Brillouin zone as a linear combination of the solutions $\Delta_j(\mathbf{k})$ of Eqn (3) in each region,

$$\Delta(\mathbf{R}, \mathbf{k}) = \sum_j \gamma_j \, \exp(\mathrm{i}\mathbf{K}_j\mathbf{R}) \, \Delta_j(\mathbf{k}) \,, \tag{6}$$

where **R** is the center-of-mass radius vector of the **K** pair and the coefficients γ_j are determined by the irreducible representation used to transform order parameter (6). The irreducible representation $A_{1\mathrm{g}}$ results in the g symmetry of the order parameter with two families of zero lines, namely, along the coordinate axes and along the diagonals of the Brillouin zone. The representation $B_{1\mathrm{g}}$ corresponds to a d symmetry with zero lines along the coordinate axes. The symmetric solution with two nodes upon **K** pairing leads to an extended s symmetry in the case of the representation $A_{1\mathrm{g}}$ and to a d symmetry in the case of $B_{1\mathrm{g}}$.

4. Biordered superconducting state and a strong pseudogap

The effective pairing potential $U(r)$ oscillates in real space due to the limitation of the domain of definition of the screened Coulomb repulsion $U(\mathbf{k}, \mathbf{k}')$ in the momentum space upon **K** pairing (Fig. 3). Strong repulsion at small distances corresponds to incomplete limitation of the double occupation [10]. Outside this region, damped oscillations naturally lead to an effective attraction, which is required for the appearance of a bound state in a **K** pair. Apart from the bound state with a negative energy E_i of the relative motion of a **K** pair, the oscillating pairing interaction allows long-lived QSSs of pairs with momenta close to **K**, which are similar to the states of radioactive isotopes exhibiting α decay. The wave functions of the relative motion of a **K** pair that correspond to the bound state and QSS are orthogonal to each other and are mainly localized in a wide real-space region outside the strong intracenter repulsion region (see Fig. 3). The presence of a tunneling barrier $E_\mathrm{b} - E_\mathrm{q}$ and orthogonal wave functions results in a pronounced asymmetry between the spectral weights of filled and vacant QSSs, which is reflected in the asymmetry of the tunneling current – voltage characteristics detected in [38, 39].

K pairs can exist as long-lived QSSs at temperatures above T_c owing to a significant increase in the density of states in a narrow range near the QSS energy E_q. To overcome a potential barrier before the tunneling decomposition of a

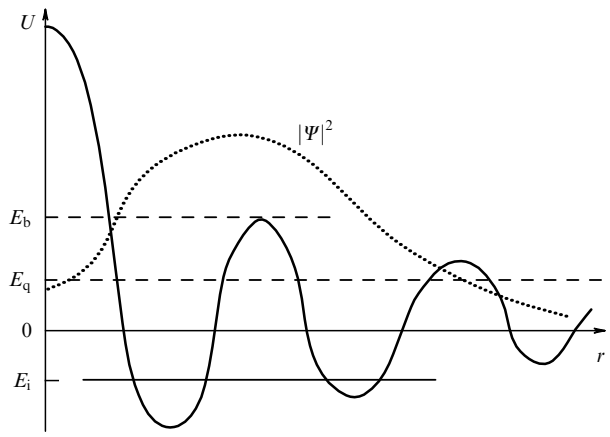

Figure 3. The oscillating pairing interaction $U(r)$ in real space and the squared modulus of the wave function of a **K** pair vs. the distance between the particles forming the pair. The BS and QSS energies of the pair are respectively denoted by E_i and E_q; E_b is the **K**-pair dissociation energy.

noncoherent pair, this pair should accumulate an energy higher than the barrier E_b. Thus, the energy $E_\mathrm{q} - E_\mathrm{i}$ is insufficient to destroy the SC coherence, and the pair breaking energy should exceed $E_\mathrm{b} - E_\mathrm{i}$. The range between the SC transition temperature $T_\mathrm{c} \sim E_\mathrm{q} - E_\mathrm{i}$ and the crossover temperature $T_\mathrm{s}^* \sim E_\mathrm{b} - E_\mathrm{i}$ can be interpreted as the strong pseudogap that is observed in underdoped cuprates at $T > T_\mathrm{c}$. If the peak of the density of states at E_q is smoothed due to an increase in the QSS damping Γ, the strong pseudogap becomes undetectable. In this case, the SC transition from a coherent to a noncoherent state is accompanied by the breaking of pairs at energies about $E_\mathrm{b} - E_\mathrm{i}$, as in the BCS theory.

By analogy with the relation between the problem of two Cooper particles [40] and the BCS theory [2], the pair breaking energy $E_\mathrm{b} - E_\mathrm{i}$ for direct excitation from a bound state to a continuous spectrum corresponds to a momentum-dependent energy gap $\Delta(\mathbf{k})$ in the quasiparticle spectrum. For the strong-pseudogap state, this gap can be represented as $\Delta = (\Delta_\mathrm{c}^2 + \Delta_\mathrm{p}^2)^{1/2}$ due to the noncoherence of the QSS. Here, $\Delta_\mathrm{c} \sim E_\mathrm{q} - E_\mathrm{i}$ corresponds to a transition into a noncoherent QSS state and $\Delta_\mathrm{p} \sim E_\mathrm{b} - E_\mathrm{q}$ corresponds to a transition between two noncoherent states.

On the microscopic level of describing SC, the gap Δ_c and the strong pseudogap Δ_p appear with random phases. Taking the average in the mean-field approximation leads to the vanishing mean value of Δ_p at any temperature, whereas the mean value of Δ_c is nonzero for $T < T_\mathrm{c}$ because of the Bose condensation of **K** pairs from a QSS into a bound state. The root-mean-square value of a strong pseudogap $|\Delta_\mathrm{p}^2| \neq 0$ that corresponds to the decay of the QSS of **K** pairs can manifest itself at temperatures well above T_c.

We note that noncoherent SC pairs existing as a QSS for $T > T_\mathrm{c}$ exhibit their SC properties (Fig. 4) in microwave superconductivity (at frequencies up to 600 GHz [41]) and magnetic properties (Fig. 5), i.e., an enhancement of the diamagnetic response and a giant Nernst effect [5 – 7].

In the mean-field approximation, the diagonal Gor'kov function phenomenologically introduced as [42]

$$G(\omega; \mathbf{k}) = z_\mathbf{k} \left[\frac{u_+^2(\mathbf{k})}{\omega - E(\mathbf{k}) + \mathrm{i}\Gamma} + \frac{u_-^2(\mathbf{k})}{\omega + E(\mathbf{k}) - \mathrm{i}\Gamma} \right] \tag{7}$$

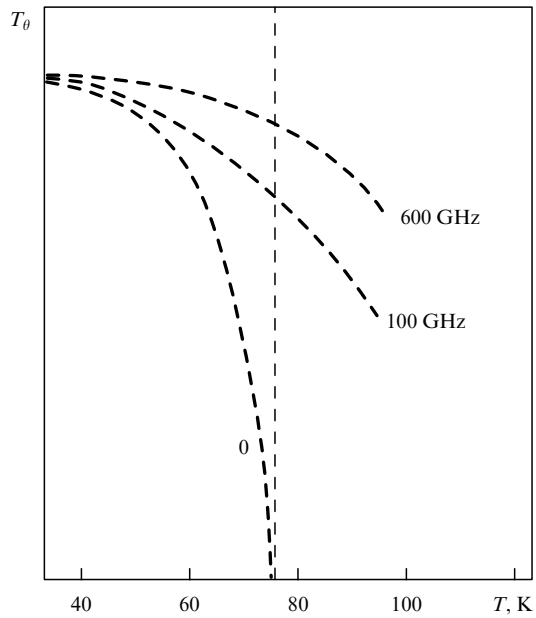

Figure 4. Temperature dependence of the phase rigidity (schematic diagram from the results of optical conductivity measurements [41]). Numerals at the curves are frequencies.

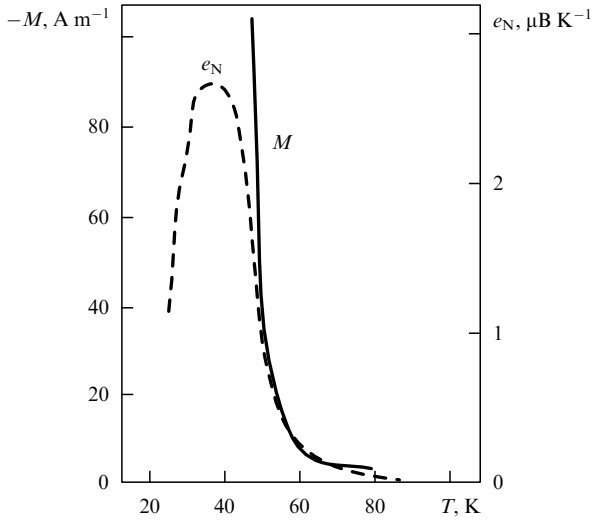

Figure 5. Diamagnetic response (magnetization M) and the Nernst signal e_N in an underdoped Bi-2212 compound (schematic diagram according to [5]).

describes a nonsuperconducting state with an *off-diagonal short-range order* (ODSRO) and corresponds to the presence of noncoherent pairs at $T > T_c$. Here, the quasiparticle energy is

$$E(\mathbf{k}) = \sqrt{\xi_K^2(\mathbf{k}) + |\Delta_c(\mathbf{k})|^2 + |\Delta_p(\mathbf{k})|^2}\,, \tag{8}$$

where $2u_\pm^2 = 1 \pm \xi_K/E$ are coherence factors and $z_\mathbf{k}$ is the momentum-dependent spectral weight of the quasiparticle. The terms in Eqn (7) pertain to pairs above and below the FC. At temperatures below T_c, an ODSRO transforms into an *off-diagonal long-range order* (ODLRO).

The excitation-induced transitions from a bound state to the QSS of the relative **K**-pair motion correspond to small but nonzero damping Γ, whereas the transitions to the stationary states of the continuous spectrum at energies higher than the barrier energy E_b should correspond to the infinitely small damping $\Gamma \to +0$. This leads to the usual Fermi-liquid behavior of diagonal Gor'kov function (7) for $T > T_s^*$ at $\Delta_p = 0$. Thus, as a result of the appearance of a QSS, the behavior of function (7) differs from the Fermi-liquid behavior over a rather wide temperature range of a strong pseudogap at $T < T_s^*$. This range corresponds to transitions between the bound and quasi-stationary states of **K** pairs and is intermediate between the two limiting approaches to the problem of superconductivity, the BCS scheme and the Bose–Einstein condensation of localized pairs. Because $|\Delta_p^2| \neq 0$ in the strong pseudogap state, the coherence factors in diagonal Gor'kov function (7) can overlap in the momentum space even at $T > T_c$, in contrast to the BCS factors (which have a Fermi shape).

The SC state appearing at $T < T_c$ should be described by both the diagonal and off-diagonal (anomalous) Gor'kov functions. We take into account that the strong pseudogap Δ_p averaged over random phases (i.e., corresponding to the mean-field approximation) vanishes (but $|\Delta_p^2| \neq 0$) and that $\Delta_c \neq 0$ at $T < T_c$, and phenomenologically introduce the anomalous Gor'kov function similarly to diagonal function (7),

$$F^+(\omega;\mathbf{k}) = -\frac{z_\mathbf{k}\Delta_c^*}{\big(\omega - E(\mathbf{k}) + \mathrm{i}\Gamma\big)\big(\omega + E(\mathbf{k}) - \mathrm{i}\Gamma\big)}\,. \tag{9}$$

This function becomes zero at $T > T_c$ and describes the ODLRO state at $T < T_c$.

In particular, superposition (6) mixes the states of two **K** pairs with opposite total momenta **K** and $-$**K**. The particles making up these pairs can also form pairs with a nonzero total momentum, which relate the **K** pairing to the conventional Cooper pairing channel (at $K = 0$). In this case, the order parameters Δ_c and Δ_0 in the **K**-pairing and Cooper-pairing channels that correspond to the mean-field approximation are solutions of a set of self-consistency equations. This set decomposes into two independent equations if we neglect the relation between the channels, and determines two temperatures (T_c, T_c') of transitions to states with the respective order parameters Δ_c and Δ_0. It is natural to assume that $T_c' < T_c$, because an antisymmetric solution with the maximum order parameter is allowable upon singlet **K** pairing and because only a symmetric solution is realized in the Cooper channel. Then, the SC transition temperature T_c can be directly obtained from Eqn (3).

Both order parameters Δ_c and Δ_0 that describe a 'biordered' SC state [42, 43] are respectively determined in the neighborhoods of PFC and FC. At $T_c' \lesssim T < T_c$, the Cooper order parameter is small compared to Δ_0, since it is induced by the Δ_c pairing. In this temperature range, the superfluid density ρ_s is proportional to the PFC length. Opening the Cooper channel at $T \approx T_c'$ results in a substantial increase in Δ_0 and ρ_s, because superfluid density is proportional to the FC length at $T \lesssim T_c'$.

In the neighborhood of PFC, two branches ($m = 1, 2$) of the strongly anisotropic quasiparticle spectrum of a biordered superconductor take the form

$$E_m(\mathbf{k}) = \sqrt{\xi_K^2(\mathbf{k}) + |\Delta_p(\mathbf{k})|^2 + |\Delta_c(\mathbf{k}) \pm \Delta_0(\mathbf{k})|^2}\,. \tag{10}$$

The observation of a two-gap spectrum with Δ_1 and Δ_2 near 10 and 50 meV, respectively, in Bi-2212 in a tunneling

experiment (in particular, the suppression of the smaller gap in a strong magnetic field at temperatures 30 – 50 mK) [44] can be considered an argument for a biordered structure of the SC state.

The SC state of cuprates is biordered due to the specific features of their band structure that are associated with the CuO_2 plane and lead to the nesting and mirror nesting of the FC. The specific features of the phase diagram of cuprates (Fig. 1) can be related to the doping-induced evolution of the FC and pairing interaction. The $U(r)$ pairing potential, which oscillates in real space (see Fig. 3), is assumed to change with increasing x such that only a noncoherent QSS of the relative motion of a **K** pair appears in this potential at the weakest doping, which corresponds to a strong pseudogap penetrating into the insulating state at $x < x_*$. In the underdoped region ($x_* < x \lesssim x_{\rm opt}$), a bound state of the pair appears along with the QSS, and the state energy $E_{\rm i}$ and the damping of the QSS Γ increase as x increases until, at $x_{\rm opt}$, the pair breaking energy becomes approximately equal to the energy corresponding to the loss of phase coherence. Then, in the overdoped region ($x_{\rm opt} \lesssim x < x^*$), the pairing interaction only causes a bound state, and superconductivity in this region of the phase diagram corresponds to the BCS scheme. As the degree of doping increases, the **K**-pairing channel gradually makes way for the Cooper channel, and, when x exceeds $x_{\rm opt}$, the decrease in $T_{\rm c}$ with increasing x up to the vanishing of $T_{\rm c}$ at x^* can also be related to the doping dependence of the pairing interaction. Specifically, the enhancement of repulsion at $x > x_{\rm opt}$ increases because the FC leaves the extended neighborhood of the saddle point.

The experimental data that are obtained for cuprates are unusual for the BCS scheme, and the phonon pairing mechanism can be naturally described using the concept of **K** pairing [8].

5. Superconductivity of multilayer cuprates

In the homologous series of cuprates, the SC transition temperature exhibits a universal dependence on the number n of CuO_2 planes in a unit cell. As n increases, the $T_{\rm c}(n)$ function first increases and reaches a maximum at $n = 3$, and then decreases monotonically. Explaining the $T_{\rm c}(n)$ dependence is a challenging problem of the physics of cuprates [17]. Figure 6 shows the $T_{\rm c}(n)$ dependences of a number of mercury-containing cuprates [45].

The charge distribution introduced upon doping of multilayer compounds is nonuniform: the inner layers have a lower hole concentration compared to the outer layers, which corresponds to a minimum in the electrostatic energy [46]. The optimum doping of a multilayer compound consists in underdoped inner and overdoped outer planes, as compared to the optimum doping of a compound with a single CuO_2 plane in the unit cell.

Coherent tunneling of pairs between neighboring layers qualitatively (not quantitatively) explains the initial increase in the $T_{\rm c}(n)$ function and its subsequent saturation (at $n > 3$) [47]. The decrease in $T_{\rm c}(n)$ at $n > 3$ is explained by a nonuniform carrier distribution in unit-cell layers and the competition of an SC ordered state and an insulating (in the form of an orbital current density d wave) ordered state. The significant increase in the superconducting transition temperature with an increase in the number of unit-cell layers can be related to the fact that the effective radius of the screened Coulomb pairing interaction exceeds the distance between neighboring layers.

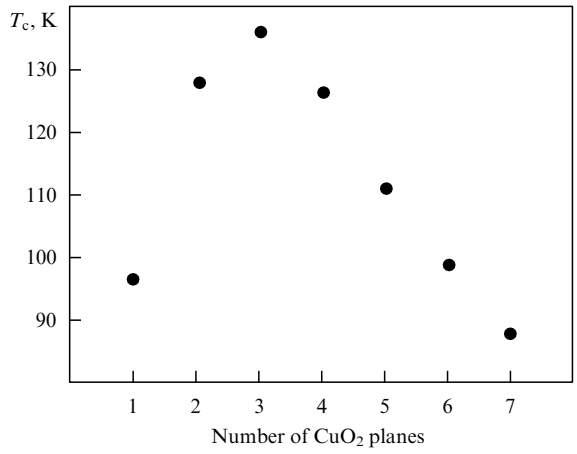

Figure 6. The SC transition temperature vs. the number of CuO_2 planes in a unit cell for the $HgBa_2Ca_{n-1}Cu_nO_{2n+2+\delta}$ homologous series (schematic diagram according to [45]).

The Fermi surface is open along the k_z axis because of the smallness of the hopping integrals between layers. The section of this surface by the k_xk_y planes corresponding to different layers represents a set of n layers, which are different due to different doping levels. SC pairing with momentum **K** can occur not only for the particle momenta $\mathbf{k}_\pm$ and $\mathbf{k}'_\pm$ (before and after scattering) in one plane but also in the case where these momenta correspond to different (nearest) planes. Another possibility is associated with pair tunneling between neighboring cuprate planes: particle momenta belong to one plane before scattering and to another plane after scattering.

With the **K**-pairing channel, we can easily explain the universal $T_{\rm c}(n)$ dependence detected in the homologous series of cuprates.

The limitation related to taking the interaction into account only in the nearest neighbor layers reduces the increase rate of the effective coupling constant as n increases, since the inner layer has two nearest neighbors and the outer layers have only one nearest neighbor. If the FC were the same for all layers, the effective coupling constant would saturate as n increases. Nonuniform doping of cuprate layers within one unit cell violates the mirror nesting condition in the interlayer interaction mechanism, since the FCs of neighboring cuprate layers are different because of different degrees of their filling.

The difference in the carrier concentrations in neighboring layers plays the role of an exchange field in weakly ferromagnetic superconductors. The violation of the interlayer mirror nesting smooths the logarithmic singularity in the self-consistency equation and results in an order parameter of type (6), as in the case of the intralayer mirror nesting. The deviations from mirror nesting and the doping optimal for a monolayer increase with n because of an increase in the role of electrostatic effects, which reduce the condensation energy and are the main causes of the decrease in the $T_{\rm c}(n)$ dependence after reaching its maximum.

Cuprates are strongly anisotropic quasi-two-dimensional systems of weakly coupled CuO_2 planes; therefore, cuprate superconductivity theories are constructed as theories describing one such plane. In crystals with several weakly tunneling-coupled CuO_2 planes, the Coulomb pairing interaction only couples pairs of the nearest-neighbor planes because of the specific features of 2D screening [50]. There-

fore, an increase in the number of layers in a unit cell results in a noticeable increase in the effective coupling constant only at small n; for $n > 3$, this increase slows down and the coupling constant saturates. The presence of charge reservoirs between conducting planes in multilayer cuprates, which favors superconductivity in the CuO_2 plane in the sense that doping does not cause structural defects in it, leads to a nonuniform carrier distribution in unit-cell planes, which is required for the minimization of the electrostatic energy. In the case of **K** pairing (where an antisymmetric solution corresponding to the maximum possible SC order parameter amplitude), the role of this nonuniform distribution, which violates the mirror nesting of the FC upon pairing in neighboring layers, is analogous to the role of magnetization, which changes the pairing conditions and decreases T_c.

6. Increasing the superconducting transition temperature: the 3D path

The search for or creation of structures with SC transition temperatures higher than the reached record value can be related to the variation in the chemical compositions and structures of cuprate superconductors. The estimates made in terms of the $t-J$ model suggest that layered 2D cuprate-like compounds in which Cu atoms in conducting planes are replaced by any other elements that can supply carriers to these planes can hardly exhibit the T_c characteristics of cuprates [28]. This means that the path of a significant increase in T_c due to a change in the chemical composition of conducting planes in such 2D crystals is most likely to be a traveled path. Nevertheless, the substantial increase in T_c in multilayer cuprates (compared to T_c in the corresponding one-layer cuprates) at $1 < n \lesssim 3$ indicates the possibility of enhancing the effective coupling constant in passing from a 2D to a 3D (three-dimensional) system and another, apparently more promising, way of searching for high-T_c compounds.

The realization of the **K**-pairing conditions in a 3D system is mainly restricted by how close the Fermi surface (FS) can approach the mirror nesting condition in a sufficiently wide 3D kinematic limitation region. If we start with the dispersion law characteristic of strongly coupled cuprates, it is obvious that mirror nesting for such a structure can be provided if certain relations between the dispersion-law parameters are satisfied. Therefore, the main problem is to control these parameters such that they fall in relatively narrow ranges corresponding to mirror nesting.

When atoms form a simple cubic lattice, the dispersion law that takes hopping only between the nearest, next-to-nearest, and next-next-to-nearest neighbor atoms into account is

$$\begin{aligned}\varepsilon(k_x, k_y, k_z) = &-2t(\cos k_x + \cos k_y + \cos k_z)\\ &+ 2t'(\cos k_x \cos k_y + \cos k_y \cos k_z + \cos k_z \cos k_x)\\ &+ t''(\cos 2k_x + \cos 2k_y + \cos 2k_z)\,. \qquad (11)\end{aligned}$$

It leads to a large variety of FS shapes, depending on the chemical potential. In particular, the FS can have the shape of a cube with rounded corners and weakly bent faces parallel to the boundaries of the 3D Brillouin zone. At the hopping-integral ratios $t'/t \approx -0.3$ and $t''/t \approx +0.3$ [which differ from the ratios characteristic of 2D cuprates ($t'/t \approx -0.3$, $t''/t \approx +0.2$)], this FS provides nesting at momenta **Q** connecting the faces and mirror nesting at pair momenta **K** parallel and not equal to **Q**. As in the case of large-momentum pairing in a 2D system, the 3D kinematically restricted regions that appear in the case of **K** pairing result in a screened pairing Coulomb potential that oscillates in real space and extends outside the region of strong intracenter repulsion. This potential, one of whose eigenvalues is negative, allows the existence of bound states of both the relative motion of a pair and the QSS.

The conditions for the occurrence of a bound state in an asymmetric 3D potential well differ from those for low-dimensional systems [37]: generally speaking, a 3D potential well couples a pair of particles weakly compared to a 2D well with the same depth and width. However, upon **K** pairing in a 3D system with the mirror nesting of the FS, a logarithmic singularity forms in the self-consistency equation in the neighborhood of the part of the Fermi surface where the mirror nesting condition is satisfied rather than in the neighborhood of a line in the Fermi surface, as in a 2D system (where this line is represented by the PFC). For a pair momentum directed along a Brillouin zone edge, this part (*pair Fermi surface,* PFS) includes two pairs of mutually perpendicular planar FC sections connected by rounded portions of the PFS (Fig. 7) rather than one pair of parallel planar FS sections, as in the case of **K** pairing in a 2D system (where the PFC consists of two parallel FC segments). This corresponds to an increase in the density of states of the relative motion of a **K** pair on the FS, which is tantamount to an increase in the effective coupling constant. Thus, upon **K** pairing, any section of the FS by a plane normal to the pair momentum inside the kinematic limitation region satisfies the mirror nesting condition (e.g., for a section by the (k_x, k_y) plane, pairing with a momentum $\mathbf{K} = (0, 0, K)$ is similar to the Cooper pairing that corresponds to the zero projection of the pair momentum onto this plane), and the role of almost planar FS faces is to ensure as large a PFS area as possible.

The nesting condition that favors insulating pairing at nesting momentum **Q** that is normal to only one pair of the FS face pairs is also satisfied at almost planar FS faces, although both pairs of faces promote SC pairing. In this sense, the efficiency of insulating pairing with respect to SC pairing in a 3D system decreases compared to that in a 2D system; that is, the appearing SC order is suppressed more weakly by a competing insulating order.

The repulsion-induced pairing in a 3D system leads to the SC order parameter $\Delta(\mathbf{K})$ with zeros distributed over the *zero surface* that has lines of intersection with the FS and corresponds to the symmetry or antisymmetry of $\Delta(\mathbf{K})$ with respect to the inversion of the momentum of the relative motion of a pair. The coefficient of the logarithm in the self-consistency equation is specified by the neighborhood of the

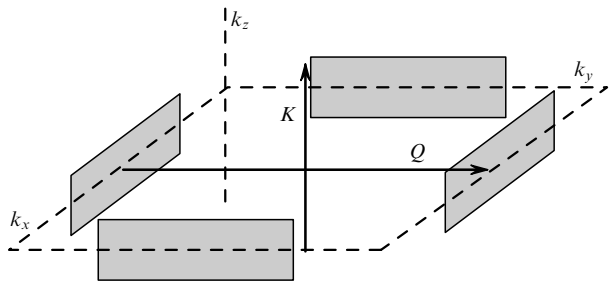

Figure 7. Nesting (at momentum **Q**) and mirror nesting (at total pair momentum **K**) for a Fermi surface with almost planar sections (shaded).

line of intersection of the FS and the order parameter zero line in which both intersecting surfaces are close to each other. For a d-wave order parameter in a 2D system, these neighborhoods of the points of intersection of the FC and the zero line along the diagonals of the Brillouin zone are definitely small, which strongly restricts the SC gap amplitude, e.g., in the scheme of spin-fluctuation pairing [34]. Therefore, the more complex topology of the SC order parameter, which results from **K** pairing upon Coulomb repulsion and is determined by the distribution of zero lines or surfaces in a 2D or 3D system, can lead to a substantially larger gap.

The complex topology of the momentum-dependent SC order parameter that is inherent in repulsion-induced pairing significantly complicates the numerical solution of a 2D self-consistency equation [36], e.g., compared to the corresponding procedure in the Eliashberg theory [21], where the order parameter depends on a single energy variable.

Of course, the ideology of the physics of cuprates cannot be used to search for or to create high-T_c 3D systems. If superconductivity in such a system is assumed to be realized upon doping of a certain parent insulator (as in the case of cuprates), the problem of a charge reservoir for a 3D atomic lattice supplying carriers to the conduction band appears. If superconductivity in a 3D crystal occurs in the absence of doping for a not-half-filled conduction band, the problem of controlling the dispersion-law parameters in a given crystal structure in order to ensure the mirror nesting of the FS is still an open question.

Because the superfluid density in underdoped cuprates is low, the phase transition into an SC state, i.e., the appearance of phase coherence, is specified not by the SC pair binding energy but by phase fluctuations [51]. Therefore, an SC transition in a 2D system inevitably acquires the features of the Berezinskii – Kosterlitz – Thouless transition [52, 53], which describes the thermal birth and disappearance of vortex – antivortex pairs. In a 3D system, the SC transition temperature is much less sensitive to phase fluctuations, which should broaden the SC state region due to the narrowing of the strong-pseudogap region, whose size increases with decreasing the vortex core energy [4].

Acknowledgments. This work was supported by the Russian Foundation for Basic Research, project nos. 05-02-17077a, 06-02-17186a.

References

1. Bednorz J G, Müller K A *Z. Phys. B* **64** 189 (1986)
2. Bardeen J, Cooper L N, Schrieffer J R *Phys. Rev.* **108** 1175 (1957)
3. Norman M R, Pines D, Kallin C *Adv. Phys.* **54** 715 (2005)
4. Lee P A, Nagaosa N, Wen X-G *Rev. Mod. Phys.* **78** 17 (2006)
5. Wang Y et al. *Phys. Rev. Lett.* **95** 247002 (2005)
6. Li L et al. *Europhys. Lett.* **72** 451 (2005)
7. Wang Y, Li L, Ong N P *Phys. Rev. B* **73** 024510 (2006)
8. Belyavsky V I, Kopaev Yu V *Usp. Fiz. Nauk* **176** 457 (2006) [*Phys. Usp.* **49** 441 (2006)]
9. Izyumov Yu A *Usp. Fiz. Nauk* **161** (11) 1 (1991); **165** 403 (1995); **169** 225 (1999) [*Sov. Phys. Usp.* **34** 935 (1991); *Phys. Usp.* **38** 385 (1995); **42** 215 (1999)]
10. Laughlin R B, cond-mat/0209269 (unpublished)
11. Franck J P, Lawrie D D *J. Supercond.* **8** 591 (1995)
12. Zhao G et al. *Nature* **385** 236 (1997)
13. Williams G V M et al. *Phys. Rev. Lett.* **80** 377 (1998)
14. Zhao G *Phys. Rev. B* **64** 024503 (2001)
15. Brandow B H *Phys. Rev. B* **65** 054503 (2002)
16. Basov D N, Timusk T *Rev. Mod. Phys.* **77** 721 (2005)
17. Leggett A J *Nature Phys.* **2** 134 (2006)
18. Loram J W et al. *Physica C* **341 – 348** 831 (2000)
19. Orenstein J, Millis A J *Science* **288** 468 (2000)
20. Demler E, Hanke W, Zhang S-C *Rev. Mod. Phys.* **76** 909 (2004)
21. Maksimov E G *Usp. Fiz. Nauk* **170** 1033 (2000) [*Phys. Usp.* **43** 965 (2000)]
22. Anderson P W *Science* **235** 1196 (1987)
23. Anderson P W et al. *J. Phys.: Condens. Matter* **16** R755 (2004)
24. Franz M, Tešanović Z, Vafek O *Phys. Rev. B* **66** 054535 (2002)
25. Sachdev S *Science* **288** 475 (2000)
26. Zhang S-C *Science* **275** 1089 (1997)
27. Guidry M et al. *Phys. Rev. B* **63** 134516 (2001)
28. Lee P A *Rep. Prog. Phys.* **71** 012501 (2008)
29. Campuzano J C, Norman M R, Randeria M, in *The Physics of Superconductors* Vol. 2 *Superconductivity in Nanostructures, High-T_c and Novel Superconductors, Organic Superconductors* (Eds K H Bennemann, J B Ketterson) (Berlin: Springer-Verlag, 2004) p. 167
30. Damascelli A, Hussain Z, Shen Z-X *Rev. Mod. Phys.* **75** 473 (2003)
31. Hirsch J E *Phys. Rev. B* **59** 11962 (1999)
32. Lanzara A et al. *Nature* **412** 510 (2001)
33. Rusinov A I, Kat D C, Kopaev Yu V *Zh. Eksp. Teor. Fiz.* **65** 1984 (1973) [*Sov. Phys. JETP* **38** 991 (1974)]
34. Millis A J, Monien H, Pines D *Phys. Rev. B* **42** 167 (1990)
35. Bulaevskiĭ L N *Usp. Fiz. Nauk* **115** 263 (1975) [*Sov. Phys. Usp.* **18** 131 (1975)]
36. Belyavsky V I, Kapaev V V, Kopaev Yu V *Pis'ma Zh. Eksp. Teor. Fiz.* **86** 462 (2007) [*JETP Lett.* **86** 404 (2007)]
37. Landau L D, Lifshitz E M *Kvantovaya Mekhanika: Nerelyativistskaya Teoriya* (Quantum Mechanics: Non-Relativistic Theory) (Moscow: Fizmatlit, 2001) [Translated into English (Oxford: Pergamon Press, 1977)]
38. Pan S H et al. *Nature* **413** 282 (2001)
39. Randeria M et al. *Phys. Rev. Lett.* **95** 137001 (2005)
40. Cooper L N *Phys. Rev.* **104** 1189 (1956)
41. Corson J et al. *Nature* **398** 221 (1999)
42. Belyavsky V I, Kopaev Yu V *Phys. Rev. B* **76** 214506 (2007)
43. Belyavskiĭ V I, Kopaev Yu V, Nguen Ngoc Tuan *Zh. Eksp. Teor. Fiz.* **132** 831 (2007) [*JETP* **105** 726 (2007)]
44. Vedeneev S I, Maude D K *Phys. Rev. B* **72** 144519 (2005)
45. Kuzemskaya I G, Kuzemsky A L, Cheglokov A A *J. Low Temp. Phys.* **118** 147 (2000)
46. Trokiner A et al. *Phys. Rev. B* **44** 2426 (1991)
47. Chakravarty S, Kee H-Y, Völker K *Nature* **428** 53 (2004)
48. Chakravarty S et al. *Phys. Rev. B* **63** 094503 (2001)
49. Belyavsky V I, Kopaev Yu V *Pis'ma Zh. Eksp. Teor. Fiz.* **83** 606 (2006) [*JETP Lett.* **83** 515 (2006)]
50. Ando T, Fowler A B, Stern F *Rev. Mod. Phys.* **54** 437 (1982)
51. Emery V J, Kivelson S A *Nature* **374** 434 (1995)
52. Berezinskii V L *Zh. Eksp. Teor. Fiz.* **61** 1144 (1971) [*Sov. Phys. JETP* **34** 610 (1972)]
53. Kosterlitz J M, Thouless D J *J. Phys. C: Solid State Phys.* **6** 1181 (1973)